

ELECTRIC FIELDS ON GIBBSITE NANOPATELET ASSEMBLIES,
NANOPYRAMID SERS SUBSTRATES AND GRAPHENE ACTUATORS

By

TZUNG-HUA LIN

A DISSERTATION PRESENTED TO THE GRADUATE SCHOOL
OF THE UNIVERSITY OF FLORIDA IN PARTIAL FULFILLMENT
OF THE REQUIREMENTS FOR THE DEGREE OF
DOCTOR OF PHILOSOPHY

UNIVERSITY OF FLORIDA

2010

© 2010 Tzung-Hua Lin

To my Mom, Yue-Shia Wu

ACKNOWLEDGMENTS

I would like to thank Dr. Jiang for his advice over the past few years and people in Jiang's group for their help, especially Wei-Han Huang for providing gibbsite nanoplatelets and In-Kook Jun for mechanical tests.

TABLE OF CONTENTS

	<u>page</u>
ACKNOWLEDGMENTS.....	4
LIST OF TABLES.....	8
LIST OF FIGURES.....	9
LIST OF ABBREVIATIONS.....	14
ABSTRACT.....	16
CHAPTER	
1 INTRODUCTION.....	17
2 BIOINSPIRED ASSEMBLY OF GIBBSITE NANOPLATELETS BY ELECTRIC FIELD.....	19
Background.....	19
Learning from Nature.....	19
Bottom-up Self-assembly.....	19
Electrodeposition.....	20
Gibbsite Nanoplatelets.....	21
Experimental.....	22
Materials and Substrates.....	22
Instrumentation.....	22
Synthesis of Gibbsite Nanoplatelets.....	23
Surface Modification of Gibbsite Nanoplatelets.....	24
EPD of Gibbsite Nanoplatelets.....	25
ETPTA-Gibbsite Nanocomposites.....	25
Mechanical Test.....	26
Results and Discussion.....	26
Gibbsite Characterization.....	26
EPD of Gibbsite Nanoplatelets.....	27
Polymer-Gibbsite Nanocomposites.....	29
TGA and Tensile Strength of Gibbsite-based Nanocomposites.....	30
Summary.....	32
3 ELECTROPHORETIC CO-DEPOSITION OF POLYMER-GIBBSITE COMPOSITES.....	46
Background.....	46
Experimental.....	46
EPD of Nanoplatelets.....	46
EPD of PVA-Gibbsite nanoplatelets.....	47

	EPD of PEI-Gibbsite nanoplatelets	47
	Results and Discussion.....	47
	Electrophoretic Co-deposition of PVA-Gibbsite	47
	Electrophoretic Co-deposition of PVA-Gibbsite	49
	Summary	53
4	ELECTROPHORETIC ASSEMBLY OF SURFACE-ROUGHENED GIBBSITES....	62
	Background.....	62
	Experimental.....	63
	Coating of Gibbsite Nanoplatelets with Silica	63
	EPD of Nanoplatelets	64
	EPD of SCG nanoplatelets.....	64
	EPD of PEI-SCG nanoplatelets.....	64
	Results and Discussion.....	65
	SCG Nanoplatelets.....	65
	EPD of SCG Nanoplatelets	66
	PEI-SCG Colloidal Stability	67
	EPD of PEI-SCG Nanoplatelets	68
	ETPTA-PEI-SCG Nanocomposites	70
	Summary	72
5	ELECTROCHEMICAL SERS AT PERIODIC METALLIC NANOPYRAMID ARRAYS.....	80
	Background.....	80
	Surface Plasmon	80
	Extraordinary Optical Transmission.....	81
	Surface-enhanced Raman Scattering	82
	Substrates for Surface-enhanced Raman Scattering	83
	Experimental.....	85
	Preparation of Electrochemical SERS-active Gold Nanopyramid Arrays	85
	Electrochemical Surface-enhanced Raman Scattering	86
	Cyclic Voltammetry Measurements	87
	Electromagnetic Modeling of Raman Enhancement.....	87
	Results and Discussion.....	88
	Colloidal Templating Process for Nanopyramid Array Fabrication	88
	Electrochemical SERS Spectra of Pyridine on Gold Nanopyramid Arrays	89
	Electrode Effects	91
	Electromagnetic Modeling	93
	Summary	94
6	GRAPHENE PAPER ACTUATORS	105
	Background.....	105
	Experimental.....	106
	Materials and Methods	106

Graphene papers	106
Prior to Hummers' method	107
Hummers' method.....	107
Exfoliation and reduction of GO	108
Graphene actuators	108
Results and Discussion.....	109
GO and Graphene Dispersions	109
Graphene Papers	110
Graphene Actuators	111
Summary	114
7 CONCLUSIONS	131
LIST OF REFERENCES	134
BIOGRAPHICAL SKETCH.....	142

LIST OF TABLES

<u>Table</u>		<u>page</u>
5-1	Assignment of SERS peaks for pyridine adsorbed on gold nanopyramid electrode.....	96

LIST OF FIGURES

<u>Figure</u>	<u>page</u>
2-1 (A) Image of an abalone shell. (B) SEM image of fracture surface of aragonitic portion of abalone nacre. (C) TEM image of the nacre cross section.	34
2-2 A model of biocomposites. (A) A schematic diagram of staggered mineral crystals embedded in protein matrix. (B) A simplified model showing the load-carrying structure of the mineral-protein composites. Most of the load is carried by the mineral platelets whereas the protein transfers load via the high shear zones between mineral platelets.....	35
2-3 (A) Schematic of cathodic electrophoretic deposition (EPD) and electrolytic deposition (ELD). (B) Thickness of coatings deposited using ELD and EPD.	36
2-4 (A) Lattice structure of Gibbsite. (B) Hexagon-shape of Gibbsite and corresponding isoelectric points.	37
2-5 Schematic illustrations of (A) an electrophoretic cell and (B) deposit after EPD.	38
2-6 TEM image of gibbsite nanoplatelets. The inset shows the electron diffraction patterns obtained from a single nanoplatelet.....	39
2-7 Electrophoretic assembly of gibbsite nanoplatelets. (A) Photograph of a free-standing gibbsite film. (B) Top-view SEM image of the sample in (A). (C) Cross-sectional view of the same sample.	40
2-8 XRD patterns of the gibbsite film in Figure 2-7A.....	41
2-9 Thickness dependence of the electroplated films on the concentration of colloidal gibbsite suspensions. The thickness standard deviation for all samples is ca. 10%.....	41
2-10 Free-standing gibbsite-ETPTA nanocomposite. (A) Photograph of a transparent film. (B) Cross-sectional SEM image of the same nanocomposite film.....	42
2-11 Normal-incidence transmission spectrum of the sample in Figure 2-10A.	43
2-12 XRD patterns of the nanocomposite sample in Figure 2-10A.....	43
2-13 TGA of the ETPTA-Gibbsite nanocomposite as shown in Figure 2-10A.....	44
2-14 Tensile stress versus strain curves for plain ETPTA film, ETPTA-Gibbsite nanocomposite, and ETPTA-TPM-Gibbsite nanocomposite.	44

2-15	Tensile strength of composites as functions of volume fraction and aspect ratio of gibbsite nanoplatelets.	45
3-1	Electrodeposited PVA-Gibbsite nanocomposite. (A) Photograph of a composite film on an ITO electrode. (B) Top-view SEM image of the sample in (A). (C) Cross-sectional SEM image of the sample in (A). (D) Magnified cross-sectional image.	54
3-2	XRD patterns of an electrodeposited PVA-gibbsite composite on ITO electrode.	55
3-3	Deposit weight on ITO electrode versus electrophoretic duration.	55
3-4	TGA of the nanocomposite sample as shown in Figure 3-1A.	56
3-5	Particle size distribution of nanoplatelet suspensions at different PEI/gibbsite weight ratio. (A) R = 0, (B) R = 0.03, (C) R = 0.075, and (D) R = 0.75.	57
3-6	Electrophoretic mobility and corresponding zeta-potential of nanoplatelets at different PEI/gibbsite weight ratio.	58
3-7	SEM images of PEI-Gibbsite nanocomposite. (A) Top-view image, (B) magnified top-view image, (C) cross-sectional image, and (D) magnified cross-sectional image.	59
3-8	XRD patterns of an electrodeposited PEI-Gibbsite nanocomposite on Au electrode.	60
3-9	TGA of an electrodeposited PEI-Gibbsite nanocomposite.	60
3-10	Reduced modulus of pure gibbsite and PEI-Gibbsite nanocomposite measured by nanoindentation.	61
4-1	Cross section of abalone nacre showing the detailed structure at the lamellae boundaries. Arrows highlight locations where the nano-asperities interpose.	74
4-2	(A) TEM image of acid-leached SCG nanoplatelets. The arrows point to a silica shell with a thickness of ca. 10nm. (B) Photograph of an electrodeposited SCG film on a gold electrode.	74
4-3	Zeta-potential of PEI-SCG nanoplatelets with different amount of PEI addition. The inset shows the molecular structure of PEI.	75
4-4	SEM images of electrodeposited PEI-SCG nanocomposite. (A) Top-view image. (B) Magnified top-view image. (C) Cross-sectional image. (D) Magnified cross-sectional image.	76

4-5	XRD patterns of a PEI-SCG nanocomposite on an ITO electrode. Blue arrows point to the characteristic peaks of ITO. The inset shows a table with major lattice planes of gibbsite.	77
4-6	Photographs of (A) ETPTA-PEI-SCG and PEI-SCG deposits on ITO electrodes.....	78
4-7	Normal-incidence transmission spectra of ETPTA-PEI-SCG nanocomposite, ETPTA-PEI-SCG nanocomposite on an ITO electrode, and PEI-SCG deposit on an ITO electrode.....	78
4-8	SEM images of an ETPTA-PEI-SCG nanocomposite on an ITO electrode. (A) Cross-sectional image. (B) Magnified cross-sectional image. Red and black arrows in (A) point to a thin wetting layer of ETPTA and the ITO electrode, respectively.....	79
4-9	Tensile stress vs. strain curves for plain ETPTA film, ETPTA-Gibbsite nanocomposite, and ETPTA-PEI-SCG nanocomposite.....	79
5-1	Surface plasmons propagate along a metal/dielectric interface.	97
5-2	Extraordinary transmittance at normal incidence for a square array of holes. The area covered by holes is only 11% while the normalized-to-area transmittance of lights is 130%.	97
5-3	Schematic SERS process in which light is Raman scattered by a molecule on the surface.....	98
5-4	Schematic illustration of electrochemical SERS set up.	98
5-5	Schematic illustration of the templating procedures for fabricating gold nanopyramid array by using spin-coated monolayer colloidal crystal as template.....	99
5-6	Tilted (35°) SEM images of a gold nanopyramid array electrode prior to (A) and after (B) electrochemical SERS experiments. As templates, 320 nm silica spheres were uses.	100
5-7	Electrochemical SER spectra recorded on a gold nanopyramid array supported by a conductive carbon disk and a copper tape (red) and a flat gold control sample on silicon (black) in 0.1 M NaCl solution containing 0.05 M pyridine.	101
5-8	Electrochemical SER spectra recorded on a gold nanopyramid array supported by a conductive carbon disk and a copper tape in 0.1 M NaCl solution containing 0.05 M pyridine.	101

5-9	The gold electrode potential was swept from -1.0 V (top) to $+1.0$ V (middle) and then back to -1.0 V (bottom).	102
5-10	Cyclic voltammograms of a conductive carbon tape, a conductive copper tape, a gold nanopyramid array supported by a carbon tape, and a gold nanopyramid array supported by a carbon disk and a copper tape in 0.1 M NaCl.	102
5-11	Electrochemical SER spectra obtained on a gold nanopyramid array supported by a conductive carbon tape in 0.1 M NaCl solution containing 0.05 M pyridine. The gold electrode potential was swept from -1.0 to 0.2 V. The spectra were taken using a 785 nm diode laser at 48 μ W with an integration time of 10 s.	103
5-12	(A) Modeled Raman enhancement factor around two gold nanopyramids with base length of 320 nm and nanotips radius of curvature of 5 nm at $\lambda = 785$ nm. (B) Simulated maximum SERS enhancement factor (G_{\max}) vs. number of tips of the templated nanopyramid array with the same structural parameters as (A).	104
6-1	Mother of all graphitic forms.	116
6-2	Schematic illustration of an additional oxidation prior to Hummer's method.	117
6-3	Schematic illustration of Hummers' method for GO preparation.	118
6-4	Schematic illustration of preparation of graphene papers.	119
6-5	Images of colloidal dispersions of (A) GO and (B) graphene.	120
6-6	TEM image of graphene sheets.	120
6-7	(A) Tapping-mode AFM image of graphene sheets with (B) height profiles B1 and B2 taken along the lines in (A). The sample was prepared by drop-casting diluted graphene dispersion onto a mica substrate.	121
6-8	(A) Top and (B) bottom side images of a free-standing graphene paper made by vacuum filtration of graphene dispersion through an Anodisc membrane. ...	122
6-9	SEM images of a graphene paper. (A) Top-view SEM image, (B) bottom-view SEM image and (C) cross-sectional SEM image.	123
6-10	(A) Top and (B) bottom side images of a free-standing graphene paper made by vacuum filtration of GO dispersion through an Anodisc membrane.	124
6-11	SEM images of a GO paper. (A) Top-view SEM image, (B) bottom-view SEM image and (C) cross-sectional SEM image.	125

6-12	Tensile stress versus strain curve for a free-standing graphene and GO paper.	126
6-13	Schematic illustrations of a graphene actuator. (A) Front-view of the actuator, (B) side-view of the actuator and (C) apparatus used for displacement measurement.....	127
6-14	(A) Cyclic voltammograms of a graphene strip at various scan rates in 1 M NaCl solution. A saturated calomel electrode was used as the reference electrode and a platinum wire was used as the counter electrode. The superficial active area was 0.2 cm^2 and the weight of graphene paper immersed was 0.12 mg. (B) A plot of steady state currents in (A) versus corresponding scan rates. The slop in (B) is 0.006 F.	128
6-15	(A) Cross-sectional images of a graphene actuator under eight successive potential steps with a total of four cycles ($-2/2 \text{ V}$ repeatedly). (B) Displacements of the actuator tip in (A) under repeated potential steps.....	129
6-16	(A) Two-electrode cyclic voltammograms of a graphene actuator operated between -2 and 2 volts in 1 M NaCl solution with a scan rate of 50 mV/s . (B) Corresponding displacements of the actuator in (A) as a function of cycle number.	130

LIST OF ABBREVIATIONS

AFM	Atomic force microscopy
AgFON	Silver film over nanosphere
ALD	Atomic layer deposition
DIW	Deionized water
ELD	Electrolytic deposition
EPD	Electrophoretic deposition
ETPTA	Ethoxylated trimethylolpropane triacrylate
FEM	Finite-element-method
FIB	Focused ion beam
GO	Graphite oxide
IEP	Isoelectric point
ITO	Indium tin oxide
LBL	Layer-by-layer
MFON	Metal film over nanosphere
PAH	Poly(allylamine hydrochloride)
PDMS	Polydimethylsiloxane
PDDA	Poly(diallyldimethylammonium chloride)
PEI	Polyethylenimine
PML	Perfect matched layers
PVA	Polyvinyl alcohol
PVP	Polyvinylpyrrolidone
SAED	Selected area electron diffraction
SCG	Silica-coated-gibbsite
SEM	Scanning electron microscopy

SERS	Surface-enhanced Raman scattering
SP	Surface plasmon
SPR	Surface plasmon resonance
TEM	Transmission electron microscopy
TEOS	Tetraethyl orthosilicate
TERS	Tip-enhanced Raman scattering
TGA	Thermogravimetric analysis
TPM	3-(trimethoxysilyl)propyl methacrylate
vol.	Volume
wt.	Weight
XRD	X-ray diffraction

Abstract of Dissertation Presented to the Graduate School
of the University of Florida in Partial Fulfillment of the
Requirements for the Degree of Doctor of Philosophy

ELECTRIC FIELDS ON GIBBSITE NANOPATELET ASSEMBLIES,
NANOPYRAMID SERS SUBSTRATES AND GRAPHENE ACTUATORS

By

Tzung-Hua Lin

August 2010

Chair: Peng Jiang
Major: Chemical Engineering

This dissertation focuses on the exertion of electric fields to assemble gibbsite nanoplatelets along with various polymers to mimic the intricate brick-and-mortar nanostructure found in abalone shells. A simple electrophoretic (co-)deposition technology that enables rapid production of large-area polymer nanocomposites with layered structures was studied. Addition of binders and assembling of surface-roughened gibbsite nanoplatelets were also studied. The tensile strength and the stiffness of these biomimetic nanocomposites were significantly improved when compared to pure polymer films.

The exertion of electric fields to conduct electrochemical SERS on nanostructured substrates that were templated from self-assembled colloidal silica arrays as well as to drive graphene-based actuators that were made by flow-directed assembly of one-atom-thick graphene sheets were also studied. Periodic arrays of nanoplatelets with nanoscale sharp tips and high tip density demonstrated an enhancement on the order of 10^6 . Actuations of a graphene actuator operated by cyclic voltammetry at a scan rate of 50 mV/s were able to last up to 140 cycles without significant degradation.

CHAPTER 1 INTRODUCTION

Electrodeposition technologies that enable the creation of inorganic-organic nanocomposites with oriented layered nanostructures were studied to mimic the intricate brick-and-mortar nanostructure found in the nacreous layer of abalone shells. To resolve the colloidal aggregation issue faced by using nanoclays as building blocks, electrostatically stabilized gibbsite nanoplatelets with high-aspect ratio were employed as a model system. Electrophoretic deposition (EPD) of gibbsite nanoplatelets will be discussed in Chapter 2. The interstitials between the assembled nanoplatelets were infiltrated with polymer to form optically transparent nanocomposites. The tensile strength and the stiffness of these biomimetic composites were significantly improved when compared to pure polymer films.

To avoid the infiltration process, a novel electrophoretic co-deposition technology for rapid production of polymer-gibbsite nanocomposites in a single step was also studied and will be discussed in Chapter 3. Furthermore, it is found that the arrangement of nano-asperities interposing between neighboring lamellae plays a crucial role in determining the inter-lamellae slip and the resulting mechanical properties of the natural composites. In order to help understand the surface roughness effect, gibbsite nanoplatelets were surface-coated with rough silica and results will be shown in Chapter 4. The current bottom-up technology enables scalable production of large-area nanocomposites with ordered layered structure that have potential applications ranging from gas-barrier films for optoelectronic devices to light-weight reinforced materials.

Other than assembly of gibbsite nanoplatelets by EPD, applying electric fields on surface-enhanced Raman scattering (SERS) substrates and graphene-based actuators

were also studied. In Chapter 5, a better way to generate periodically tailored structures of SERS electrodes for chemical and biochemical analysis is provided. A spin-coating technique that combines the simplicity and cost benefits of bottom-up self-assembly with the scalability and compatibility of standard top-down microfabrication in creating a large variety of nanostructured materials has been demonstrated. The methodology is based on shear-aligning concentrated colloidal suspensions using standard spin-coating equipment. The shear flow generated during the spin-coating process coupled with interparticle interaction induces the formation of wafer-scale, non-close-packed colloidal crystals with adjustable thickness ranging from monolayer to hundreds of layers. These self-assembled colloidal arrays can be used as structural templates to make metallic nanostructures. Periodic arrays of nanopylramids with nanoscale sharp tips and high tip density can enhance the local electromagnetic field in the vicinity of the nanotips, resulting in high SERS enhancement (on the order of 10^6). The effects of the applied electrode potential and the electrode redox reactions on the SERS enhancement were investigated.

In Chapter 6, electromechanical actuators based on sheets of graphene papers will be discussed. Graphite oxide (GO) sheets were generated by exfoliation of highly oxygenated graphite in water and then chemically reduced to one-atom-thick graphene sheets. The graphene sheet dispersions were further filtrated to produce graphene papers. The actuators were operated under repeated potential steps and cyclic voltammetry. Cycling stability of the graphene-based actuators was also discussed.

CHAPTER 2 BIOINSPIRED ASSEMBLY OF GIBBSITE NANOPATELETS BY ELECTRIC FIELD

Background

Learning from Nature

The spontaneous organization of nonspherical colloids has attracted great recent interest due to the wide range of potential applications of the resulting assemblies in photonic crystals (1-4), metamaterials (5), surface-enhanced Raman scattering sensors (6), and reinforced nanocomposites (7-9), as well as fundamental studies of liquid crystal phase transitions (10-13) and particle packing (14-16). Among a large variety of nonspherical colloids, platelet particles are particularly interesting as they enable the bottom-up assembly of layered nanocomposites that mimic the nacreous layer of mollusk shells (17-19). The intricate brick-and-mortar nanostructure (as in Figure 2-1) found in nacre, which consists of ~95 vol.% of brittle aragonite platelets and ~5 vol.% of soft biological macromolecules (20-23), makes the shells exceptionally tough and stiff with a tensile stress of around 100 MPa (19, 23) because most of the load can be carried by the mineral platelets whereas the protein transfers load via the high shear zones between mineral platelets, as shown in Figure 2-2 (18). The unusual combination of the mechanical strength, toughness, and stiffness in these natural inorganic-organic composites has inspired scientists to create artificial nanocomposites that mimic the mechanical design principles found in nature (7-9).

Bottom-up Self-assembly

Bottom-up self-assembly of nonspherical colloidal building blocks is of great interest for the development of new materials with potential applications in optoelectronics, photonics, magnetism, catalysis, and mechanics (1, 2, 15, 19, 24-28).

Layer-by-layer (LBL) assembly of inorganic nanoplatelets (e.g., nanoclays) and polyelectrolytes has recently been demonstrated as an efficient methodology in making reinforced polymer nanocomposites (7, 8). Ice-templated crystallization, gravitational sedimentation, centrifugation, spin-coating, and dip-coating have also been employed to align inorganic nanosheets to form nacre-like assemblies (28-31). However, these techniques are either time-consuming or require multiple steps to infiltrate the inorganic assemblies with polymer to make nanocomposites. For example, LBL assembly is a relative slow process and hundreds of bilayers need to be deposited to form composites with micrometer-scale thickness. Additionally, the significant agglomeration of commonly used clay nanoplatelets hampers the formation of highly aligned structures and thus impairs the mechanical properties of the resulting nanocomposites.

Electrodeposition

Electrodeposition is widely used for the deposition of thin films and coatings. Electrophoretic deposition (EPD) and electrolytic deposition (ELD) are the two commonly used processes, as shown in Figure 2-3. EPD is carried out based on the use of ceramic particles in suspensions and enables the preparation of thick ceramic films while ELD uses solutions of metal salts and is an important tool for the formation of nanostructured thin films (32). Electrophoresis is a well-established technology in assembling spherical colloids into highly ordered colloidal crystals (33-35). In this methodology, charged colloids are attracted by electrical force toward the counter electrode and then deposited on the electrode surface by particle coagulation (32). Electrodeposition is a simple, inexpensive, and scalable technology that enables rapid production of thick films over large areas. Electrophoretic co-deposition of colloids and polymer is also possible for the formation of nanocomposites in a single step. In

addition, deposition of metals and conducting polymers in the interstitials of colloids is easily achieved by electrophoresis. This will significantly expand the available materials for the fabrication of layered nanocomposites. Electrophoretic assembly of nanoclays has previously been tested, but the entrapment of non-platy particles caused by the agglomeration of nanoclays deteriorates the layered structure (36).

Gibbsite Nanoplatelets

Various synthetic methods have been developed to make fairly monodispersed colloidal platelets with high stability in suspensions (37-40). For instance, uniform gibbsite ($\text{Al}(\text{OH})_3$) nanoplatelets with well defined hexagon-shape can be synthesized by hydrolysis of $\text{Al}(\text{OH}_2)_6^{3+}$ at 85°C (37, 41). The aspect ratio of the synthesized gibbsite nanoplatelets (~ 10) is close to that of natural aragonite platelets in nacre (20). The diameter and thickness of the gibbsite nanoplatelets can be controlled by seeded growth (42). The gibbsite structure is a stacking of Al-OH layers and each Al^{3+} is surrounded by six hydroxyl groups, as shown in Figure 2-4. The reaction of surface hydroxyl groups with water makes the nanoplatelets highly charged in water and alcoholic suspensions. The surface hydroxyl groups also facilitate the chemical modification of the particle surface to render different functionality (41). By using gibbsite nanoplatelet as a model system, Lekkerkerker et al. have extensively exploited the liquid crystal phase transition in suspensions of plate-like particles (10-12, 43). Opal-like columnar gibbsite colloidal crystals have also been demonstrated by forced sedimentation (13, 44).

We used electrostatically stabilized gibbsite nanoplatelets with well-defined shape and size as a model system to explore the oriented assembly of plate-like colloids by electrophoresis. A simple spin-coating process were developed to infiltrate the

interstitials between the assembled nanosheets to form artificial nacreous nanocomposites. The resulting self-standing films were transparent and exhibited significantly improved mechanical properties over those of pure polymer. We also chemically functionalized the surface of the gibbsite nanoplatelets to facilitate the formation of covalent linkage between the ceramic platelets and the polymer matrix. This further reinforced these biomimetic nanocomposites.

Experimental

Materials and Substrates

All solvents and chemicals were of reagent quality and were used without further purification. Ultrapure water ($18.2 \text{ M}\Omega \text{ cm}^{-1}$) was used directly from a Barnstead water system. Ethanol (200 proof) was purchased from Pharmaco Products. Hydrochloric acid (37%), aluminum sec-butoxide (95%), and aluminum isopropoxide (98%) were obtained from Aldrich. Ethoxylated trimethylolpropane triacrylate (ETPTA) monomer was provided by Sartomer (Exton, PA). The photoinitiator, Darocur 1173 (2-hydroxy-2-methyl-1-phenyl-1-propanone), was obtained from Ciba Specialty Chemicals. Two-part polydimethylsiloxane (PDMS, Sylgard 184) was provided by Dow Corning. Indium tin oxide (ITO) coated glass substrates with sheet resistance of 8Ω were purchased from Delta Technologies. Silicon wafers (test grade, n type, (100)) were purchased from University Wafer.

Instrumentation

An EG&G Model 273A potentiostat/galvanostat was used for EPD. Scanning electron microscopy (SEM) was carried out on a JEOL 6335F FEG-SEM. A thin layer of gold was sputtered onto the samples prior to imaging. Transmission electron microscopy (TEM) and selected area electron diffraction (SAED) were performed on a

JEOL TEM 2010F. Atomic force microscopy (AFM) was conducted on a Digital Instruments Dimension 3100 unit. X-ray diffraction (XRD) spectra of the electroplated gibbsite films were obtained with Philips APD-3720 equipment. A Cu $K\alpha_1$ ($\lambda = 1.54049 \text{ \AA}$) radiation was scanned from 10° to 70° with a scan rate of $2.4^\circ/\text{min}$. Thermogravimetric analysis (TGA) was carried out in air with a Perkin-Elmer thermogravimetric analyzer and a platinum crucible between 20 and 800°C at a heating rate of $5^\circ\text{C}/\text{min}$. The zeta-potential of gibbsite nanoplatelets was measured by a Brookhaven ZetaPlus Analyzer (Brookhaven Instrument Corporation). An Ocean Optics HR4000 high resolution fiber optic UV-vis-near-IR spectrometer was used for optical transmission measurement. A standard spin-coater (WS-400B-6NPP-Lite spin processor, Laurell) was used to spin-coat ETPTA monomer. The polymerization of ETPTA was carried out on a pulsed UV curing system (RC 742, Xenon).

Synthesis of Gibbsite Nanoplatelets

The gibbsite nanoplatelets were synthesized by following a preparation method as described in the reference (37). To 1 L of ultrapure water were added hydrochloric acid (0.09 M), aluminum sec-butoxide (0.08 M), and aluminum isopropoxide (0.08 M). The mixture was stirred for 10 days and then heated in a polyethylene bottle in a water bath at 85°C for 72 h. After cooling to room temperature, dispersions of gibbsite nanoplatelets were centrifuged at $3500g$ for 6 h, and the sediments were redispersed in deionized water. For completely removing the unreacted reactants and concentrating the nanoplatelets, this process was repeated for five times. Detailed processes are listed as below:

1. Clean a 1000 ml glass flask by soaking in saturated KOH in isopropanol for 24 h.
2. Rinse the flask with DIW, then fill with 2% HF, and storage overnight.

3. Rinse the flask with DIW several times and then dry in an oven.
4. Draw 20 ml of aluminum tri-sec-butoxide (97%) with a syringe. This process might take 10 to 20 mins.
5. Meanwhile, put a stirring bar in the flask and add about 800 ml of DIW.
6. Stir at medium speed and then add 7.4 ml of HCl (37%) into the flask.
7. Add 16.3 g of aluminum isopropoxide (98%).
8. Inject the above 20 ml of aluminum tri-sec-butoxide with a syringe.
9. Fill the flask to 1000 ml with DIW.
10. Increase stirring speed.
11. Age for 10 days till all the particles dissolves.
12. Distribute the solution into several plastic bottles and then put the bottles in isotemp water bath and heat at 85°C for 72 h.
13. Wash particles by centrifuging at 3500g for 6 h.
14. Dump supernatant and add DIW.
15. Re-disperse particles.
16. Repeat processes 16 to 18 for 5 times.

Surface Modification of Gibbsite Nanoplatelets

Gibbsite nanoplatelets were surface-modified with 3-(trimethoxysilyl)propyl methacrylate (TPM) (45). Prior to adding gibbsite nanoplatelets, 10 ml of TPM was mixed with 100 ml of a water-methanol solution (water/methanol volume ratio of 3:1) for 1 h to fully hydrolyze TPM. Surface modification was then accomplished by adding 100 ml of gibbsite dispersion (ca. 1 vol.% aqueous solution) into the hydrolyzed TPM solution. The suspension was stirred at 40°C for 30 min. The modified nanoplatelets were washed by repeated centrifugation-redispersion cycles with pure ethanol and finally concentrated to a stock suspension of 0.045 and 0.035 (g/g) in ethanol.

EPD of Gibbsite Nanoplatelets

EPD of gibbsite nanoplatelets was performed in a sandwich cell placed horizontally, as shown in Figure 2-5A. The bottom and the top of the cell were an ITO working electrode and a gold counter electrode, respectively. The gold electrode was prepared by sputtering deposition of 20 nm of chromium and 200 nm of gold on a (100) silicon wafer. PDMS was used as a spacer to get an active area of $1.5 \times 1.5 \text{ cm}^2$ and a cell gap of 2.2 mm. Aqueous suspensions of gibbsite nanoplatelets with different weight percentage were used. Ethanol (200 proof) was added into the suspensions to make the volumetric ratio of ethanol to the aqueous suspension to be 2. A constant voltage of -2.5 V (ITO vs. Au) was applied for 30 min to deposit the positively charged gibbsite nanoplatelets onto the ITO cathode. After deposition, the electroplated gibbsite films (as in Figure 2-5B) were rinsed with 200-proof ethanol and then dried with compressed air.

ETPTA-Gibbsite Nanocomposites

After the oriented assembly, ETPTA-Gibbsite nanocomposites can then be made by filling the interstitials between the aligned nanoplatelets with photocurable monomers, followed by photopolymerization. We chose a nonvolatile monomer ETPTA to form the nanocomposites. A free standing gibbsite was first put on a PDMS substrate. The ETPTA monomer with 1% photoinitiator was then dropped on the gibbsite film. The sample was then put under vacuum for 10 min in order to remove as many trapped air bubbles as possible. After 10 min, the gibbsite film became transparent and then was spin-coated at 4000 rpm for 1 min to remove excess monomer solution and then polymerized by exposure to ultraviolet radiation.

Mechanical Test

For tensile strength measurement, three types of thin films (ETPTA, ETPTA-Gibbsite, and ETPTA-TPM-modified gibbsite) were tested using an Instron model 1122 load frame upgraded with an MTS ReNew system and equipped with a 500 g load cell at a crosshead speed of 0.5 mm/min. Testing samples with widths of 1.5 mm and thickness ranging from 30 to 80 μm were adhered on homemade sample holders with a 20 mm gap using polyurethane monomer as an adhesive and then UV-cured. The thickness of the tested samples was measured by cross-sectional SEM to calculate the final tensile strength.

Results and Discussion

Gibbsite Characterization

Figure 2-6 shows a typical TEM image of purified gibbsite nanoplatelets. The particles are hexagonally shaped and are relatively uniform in size. The diameter of the nanoplatelets is measured to be 188 ± 40 nm by averaging over 100 particles from the TEM micrographs. TEM images also reveal that the nanoplatelets tend to align parallel to the surface of TEM grids. AFM experiments show the platelet thickness ranges from 10 to 15 nm. The purified gibbsite nanoplatelets are electrostatically stabilized, and the zeta-potential of the colloids in deionized water is measured to be $+40.5 \pm 2.3$ mV by fitting experimental data using Smoluchowski's model. The high surface charge makes the nanoplatelets stable in aqueous and alcoholic dispersions, and aggregated particles are rarely seen in TEM images. The SAED patterns from a single platelet as shown in the inset of Figure 2-6 indicate that the as-made gibbsite nanoplatelets are single-crystal.

EPD of Gibbsite Nanoplatelets

The EPD of positively charged gibbsite nanoplatelets is carried out using a parallel-plate sandwich cell, which consists of an ITO working electrode, a gold counter electrode, and a PDMS spacer (~2.2 mm thick). The bath solution is gibbsite nanoplatelets dispersed in a water-ethanol mixture with volumetric ratio of 1:2. The volume fraction of gibbsite particles is adjusted to ~1%. Ethanol is added to the aqueous dispersions to reduce the dielectric constant of the solvent and thus reduce the electrical double-layer thickness of the particles to promote colloidal coagulation on the ITO electrode. Without ethanol, no particle deposits are adhered on the working electrode after disassembling the electrical cell. The addition of ethanol also facilitates reduction of cracking and porosity in the electrophoretically deposited films. The applied electric field strength is ~1100 V/m. The electrophoretic velocity of the gibbsite nanoplatelets is estimated to be ~7.5 $\mu\text{m/s}$ by using the Smoluchowski's equation:

$$u_E = \frac{\varepsilon \varepsilon_0 \zeta}{\mu} E$$

where ε is the dielectric constant of the solution, ε_0 is the permittivity of the vacuum, μ is the solution viscosity, and E is the applied electric field strength. For a 2.2 mm thick sandwich cell, the estimated time to deposit most particles on the ITO electrode is about 5 min, agreeing with our experimental observation. Besides parallel-plate geometry, electrodes can also be vertically inserted into the colloidal baths to conduct the EPD. As the gravitational sedimentation of the gibbsite nanoplatelets during the electrophoretic process is negligible, uniform deposits on the electrodes are obtained. After EPD, the gibbsite deposits on the ITO cathode are washed with ethanol and then dried with compressed air. The deposits can be easily peeled off from the ITO surface by using a

sharp razor blade, resulting in the formation of self-standing films as shown in Figure 2-7A. The film is opaque and brittle, and the side facing the ITO cathode is smoother than the side facing the suspension. The size of the resulting films is solely determined by the dimensions of the ITO electrode. Figure 2-7A depicts a sample with $1.6 \times 0.6 \text{ inch}^2$ size deposited on a $2 \times 1 \text{ inch}^2$ ITO electrode. Figure 2-7B shows a top-view SEM image of the suspension side of the sample in Figure 2-7A. The hexagonal gibbsite nanoplatelets are densely packed and aligned parallel to the electrode surface. The alignment of gibbsite nanoplatelets is further confirmed by the layered structure as shown in the cross-sectional SEM image of Figure 2-7C. Another convincing evidence of the orientated deposition comes from the XRD patterns shown in Figure 2-8. Only (002) and (004) peaks are observed in the XRD spectrum. As the crystallographic c-axis of single-crystal gibbsite is normal to the platelet surfaces, the (002) and (004) reflections are from gibbsite platelets oriented parallel to the electrode surface (46). Analysis of the half-height width of the (002) peak with the Scherrer equation yields an average platelet thickness of 15.1 nm, agreeing with AFM measurement.

The oriented deposition of gibbsite nanoplatelets in a direct-current (dc) electric field can be understood by considering the charge distribution on the gibbsite surfaces. Early study shows the isoelectric point (IEP) of the edges ($\text{pH} \approx 7$) differs from that on the faces ($\text{pH} \approx 10$) (37). The pH of the suspension in the electrophoretic experiments is close to 7, resulting in positively charged surfaces and almost neutral edges. Therefore, the applied electric field exerts a force only on the surfaces of the gibbsite platelets, and Brownian motion could provide sufficient torque to reorient perpendicular particles to face the ITO electrode. Once close to the electrode, the gibbsite nanoplatelets will be

forced to align parallel to the electrode surface as this orientation is more energetically favorable than the perpendicular one. Similar to the evaporation-induced alignment of gibbsite nanoplatelets on TEM grids (Figure 2-6), further evidence shows that capillary force during solvent evaporation is sufficient to orient gibbsite particles into layered assemblies. However, the rapid and uniform deposition of nanoplatelets over large areas is the major advantage of the electrodeposition technology over evaporation and gravitational sedimentation-induced assembly. If the duration of the electrophoretic process is long enough, almost all gibbsite platelets can be deposited on the ITO electrode. The thickness of the deposits is then linearly proportional to the particle volume fraction of the suspension as shown in Figure 2-9.

Polymer-Gibbsite Nanocomposites

After the oriented assembly, polymer-Gibbsite nanocomposites can then be made by filling the interstitials between the aligned nanoplatelets with photocurable monomers, followed by photopolymerization. We chose a nonvolatile monomer ETPTA to form the nanocomposites. The monomer with 1% photoinitiator is spin-coated at 4000 rpm for 1 min to infiltrate the electroplated gibbsite film and then polymerized by exposure to ultraviolet radiation. The resulting nanocomposite film becomes highly transparent (Figure 2-10A) as a result of the matching of the refractive index between the gibbsite platelets and the polymer matrix. The cross-sectional SEM image in Figure 2-10B shows that the nanocomposite retains the layered structure of the original electroplated gibbsite film, and thin wetting layers of ETPTA ($\sim 1 \mu\text{m}$ thick) are observed on the surfaces of the film. The normal-incidence transmission measurement as shown in Figure 2-11 shows that the free-standing nanocomposite film exhibits high transmittance ($>80\%$) for most of the visible wavelengths. As the reflection (R) from an

interface between two materials with refractive indices of n_1 and n_2 is governed by Fresnel's equation $R = [(n_1 - n_2)/(n_1 + n_2)]^2$, we can estimate the normal-incidence reflection from each air-nanocomposite interface to be about 4%. Thus, the optical scattering and absorption caused by the nanocomposite itself is approximately 10%. This suggests that the polymer matrix has infiltrated most interstitial spaces between the aligned gibbsite nanoplatelets. The oriented arrangement of the nanoplatelets is also maintained throughout the polymer infiltration process as confirmed by the distinctive (002) and (004) peaks of the XRD spectrum shown in Figure 2-12.

TGA and Tensile Strength of Gibbsite-based Nanocomposites

The ceramic weight fraction in the ETPTA-Gibbsite nanocomposite film is determined by TGA as shown in Figure 2-13. From the TGA curve and the corresponding weight loss rate, it is apparent that two thermal degradation processes occur. One happens at $\sim 250^\circ\text{C}$ and corresponds to the degradation of the polymer matrix, while another occurs at $\sim 350^\circ\text{C}$ and is due to the decomposition reaction of gibbsite: $2\text{Al}(\text{OH})_3 \rightarrow \text{Al}_2\text{O}_3 + 3\text{H}_2\text{O}$. On the basis of the residue mass percentage (45.65%) and assuming the ash is solely Al_2O_3 , we can estimate the weight fraction of gibbsite nanoplatelets in the original nanocomposite film to be ~ 0.70 . Considering the density of gibbsite ($\sim 2.4 \text{ g/cm}^3$) and ETPTA ($\sim 1.0 \text{ g/cm}^3$), the volume fraction of gibbsite nanoplatelets in the nanocomposites is approximately 0.50. The complete infiltration of ETPTA between the electroplated gibbsite platelets is further confirmed by the selective dissolution of gibbsite in a 2% hydrochloric acid aqueous solution. This results in the formation of a self-standing porous membrane with stacked hexagonal-shaped pores, which are a negative replica of the assembled gibbsite platelets.

The mechanical properties of the biomimetic polymer nanocomposites are evaluated by tensile tests. We compare the tensile strength for three types of thin films, including pure ETPTA, ETPTA-Gibbsite, and ETPTA-TPM-modified Gibbsite. The surface hydroxyl groups of gibbsite nanoplatelets can be easily modified by reacting with TPM through the well-established silane coupling reaction (45). This results in the formation of surface-modified particles with dangling acrylate bonds that can be cross-linked with the acrylate-based ETPTA matrix. The colloidal stability and the surface charge of the resulting nanoplatelets are not affected by this surface modification process as confirmed by TEM and zeta-potential measurement. Figure 2-14 shows the tensile stress versus strain curves for the above three types of films. The ETPTA-Gibbsite nanocomposite displays ~2-time higher strength and ~3-time higher modulus when compared with pure ETPTA polymer. Even more remarkable improvement occurs when TPM-Gibbsite platelets are cross-linked with the ETPTA matrix. We observe ~4-time higher strength and nearly 1 order of magnitude higher modulus than pure polymer. This agrees with early studies that reveal the crucial role played by the covalent linkage between the ceramic fillers and the organic matrix in determining the mechanical properties of the artificial nacreous composites (8). We also conduct a simple calculation to evaluate if the measured mechanical properties of the ETPTA-Gibbsite nanocomposites are reasonable. For a polymer matrix having a yield shear strength τ_y and strong bonding to the gibbsite nanoplatelet surface (e.g., TPM-modified gibbsites), the tensile strength of the composite (σ_c) can be calculated using the volume fraction of nanoplatelet (V_p), the nanoplatelet aspect ratio (s), and the tensile strength of the nanoplatelet (σ_p) and of the polymer matrix (σ_m), as (9)

$$\sigma_c = \alpha V_p \sigma_p + (1 - V_p) \sigma_m$$

For the gibbsite nanoplatelet which has a relatively small aspect ratio ($s \sim 12-18$), the factor R in the above equation can be estimated as

$$\alpha = \frac{\tau_y s}{2\sigma_p}$$

From the above TGA analysis, the volume fraction of gibbsite nanoplatelets in the polymer nanocomposite is ~ 0.50 . If we take $s = 15$, the first equation can then be simplified as

$$\sigma_c = 3.75\tau_y + 0.5\sigma_m$$

For acrylate-based polymer (like ETPTA), the yield shear strength should be close to its tensile strength. The final equation can further be simplified as $\sigma_c \sim 4.25\sigma_m$. This indicates that the strength of the nanocomposite is about fourfold of the strength of the polymer matrix, agreeing with our experimental results. Tensile strength of composites estimated by the above method can be further plotted as functions of volume fraction and aspect ratio of gibbsite nanoplatelets, as shown in Figure 2-15. The dot in Figure 2-15 is our experimental result while the net surface is from the proposed model.

Summary

In summary, we have developed a simple and rapid electrodeposition technology for assembling gibbsite nanoplatelets into large-area, self-standing films. These nanosheets with high aspect ratio are preferentially aligned parallel to the electrode surface. The interstitials between the assembled nanoplatelets can be infiltrated with polymer to form optically transparent nanocomposites. The tensile strength and the stiffness of these biomimetic composites are significantly improved when compared to

pure polymer films. The current electrodeposition technology is a quite general approach to achieve oriented deposition of platelet-like particles with various aspect ratios. Preliminary results show that silica-coated gibbsite nanoplatelets, hollow silica nanoplatelets, and zeolite platelets can also be aligned by EPD. The technology is also promising for developing layered metal-ceramic and conducting polymer-ceramic nanocomposites that may exhibit improved mechanical and electrical properties but are not easily available by other bottom-up technologies.

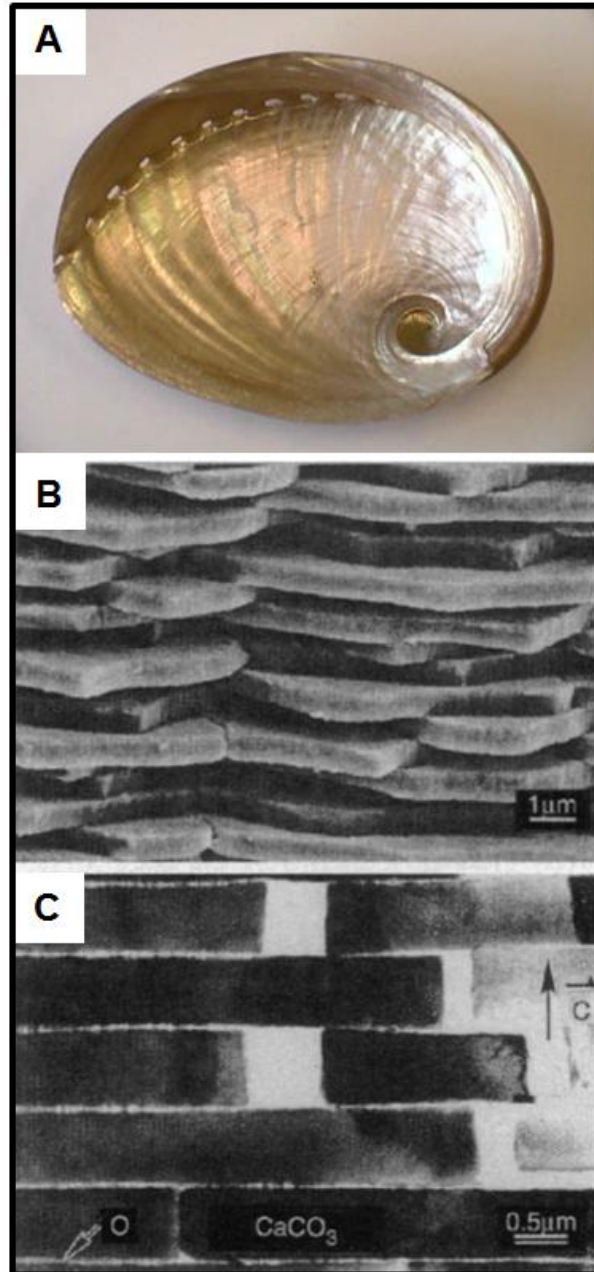


Figure 2-1. (A) Image of an abalone shell. (B) SEM image of fracture surface of aragonitic portion of abalone nacre. (C) TEM image of the nacre cross section (21).

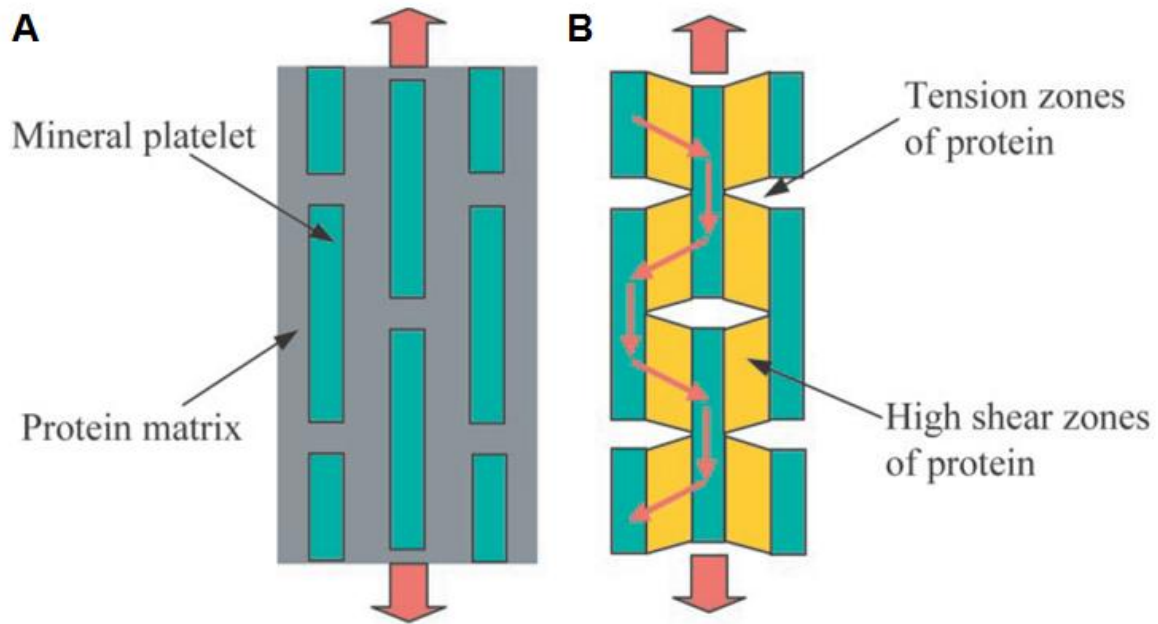


Figure 2-2. A model of biocomposites. (a) A schematic diagram of staggered mineral crystals embedded in protein matrix. (b) A simplified model showing the load-carrying structure of the mineral-protein composites. Most of the load is carried by the mineral platelets whereas the protein transfers load via the high shear zones between mineral platelets (18).

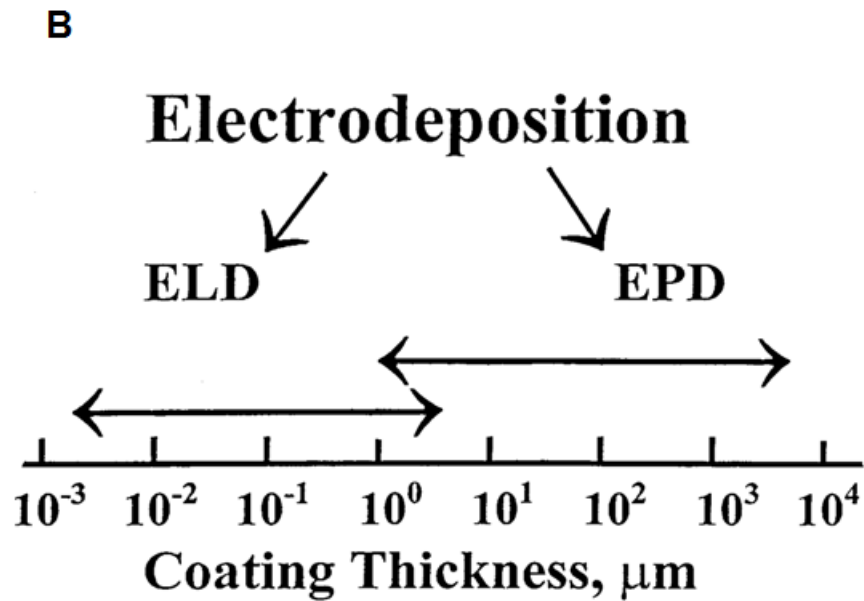
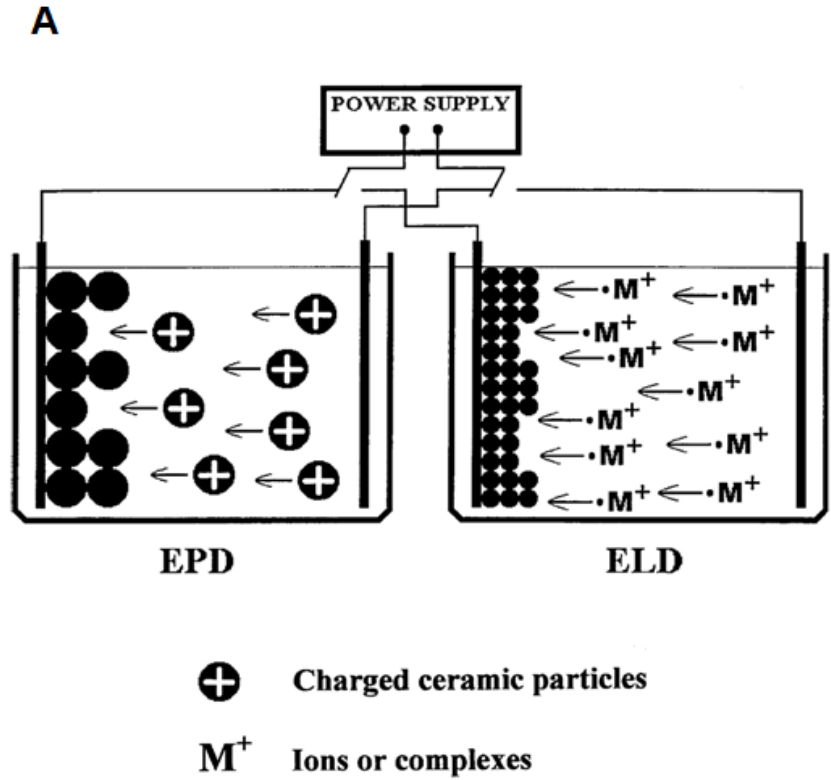


Figure 2-3. (A) Schematic of cathodic electrophoretic deposition (EPD) and electrolytic deposition (ELD). (B) Thickness of coatings deposited using ELD and EPD (32).

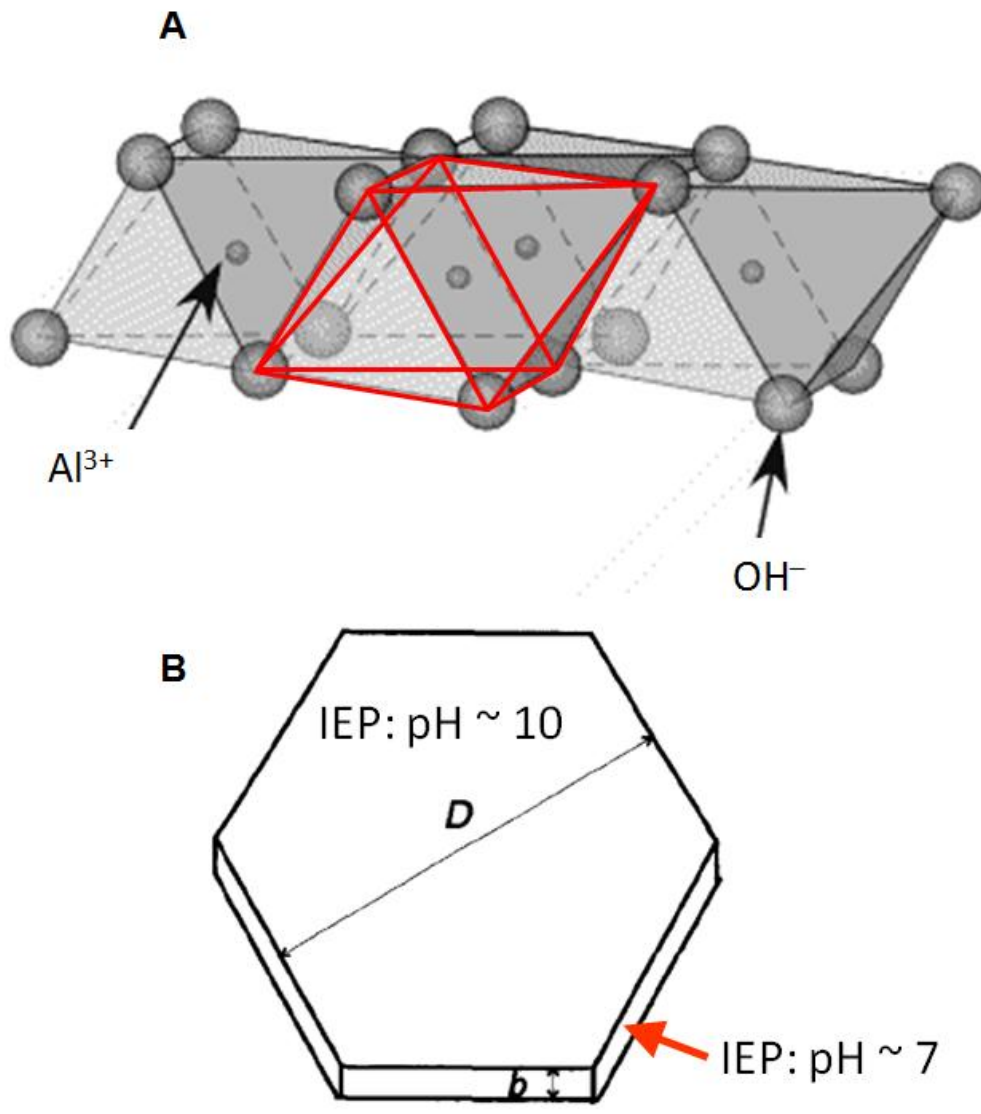


Figure 2-4. (A) Lattice structure of Gibbsite. (B) Hexagon-shape of Gibbsite and corresponding isoelectric points (41).

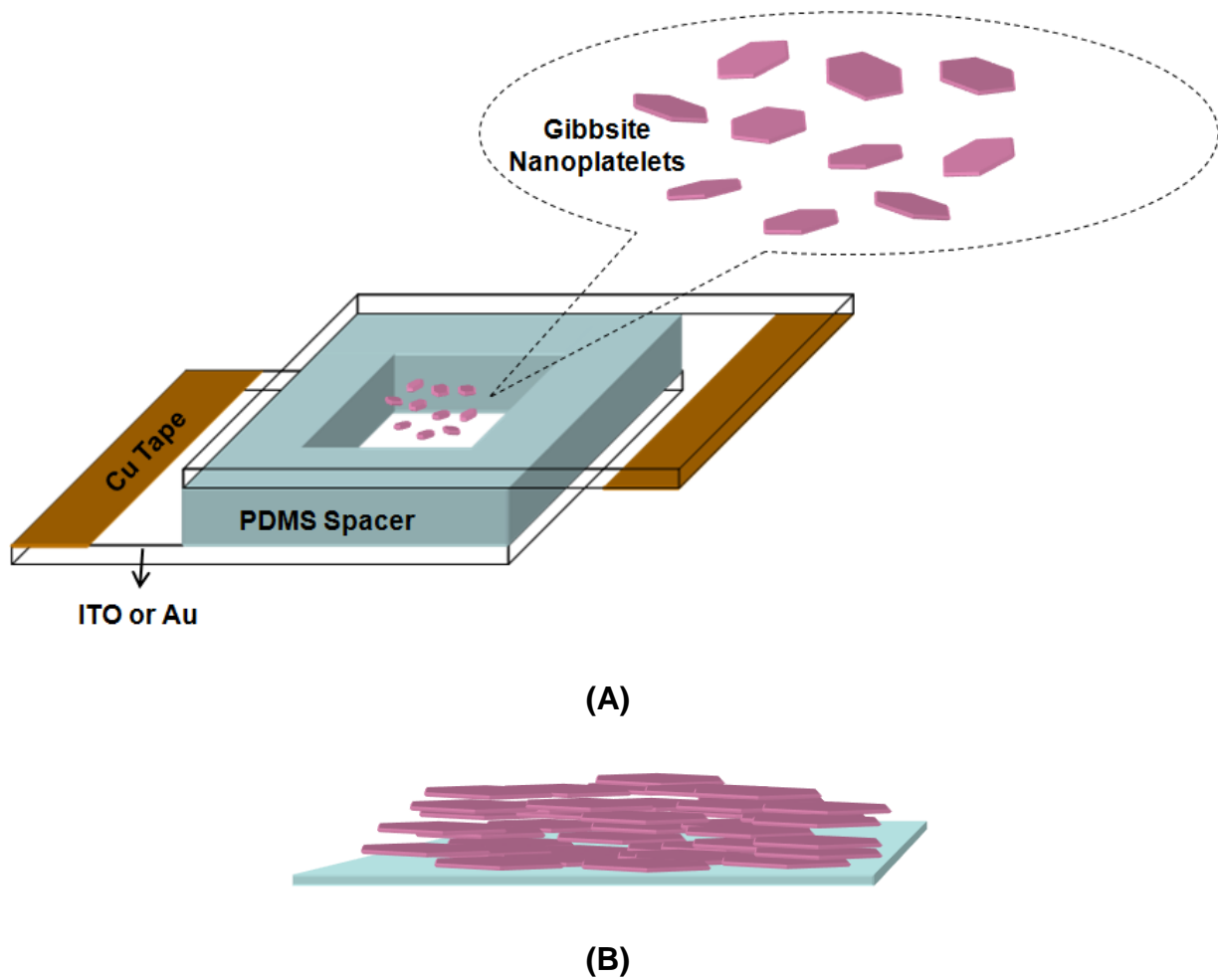


Figure 2-5. Schematic illustrations of (A) an electrophoretic cell and (B) deposit after EPD.

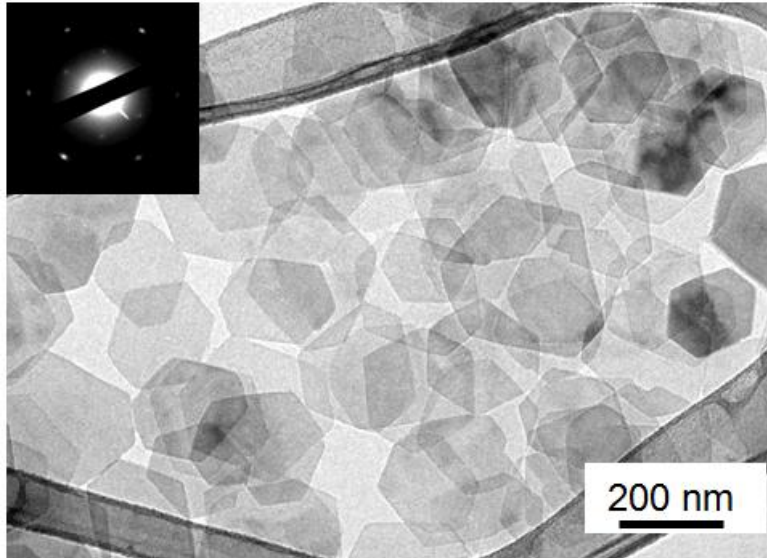


Figure 2-6. TEM image of gibbsite nanoplatelets. The inset shows the electron diffraction patterns obtained from a single nanoplatelet.

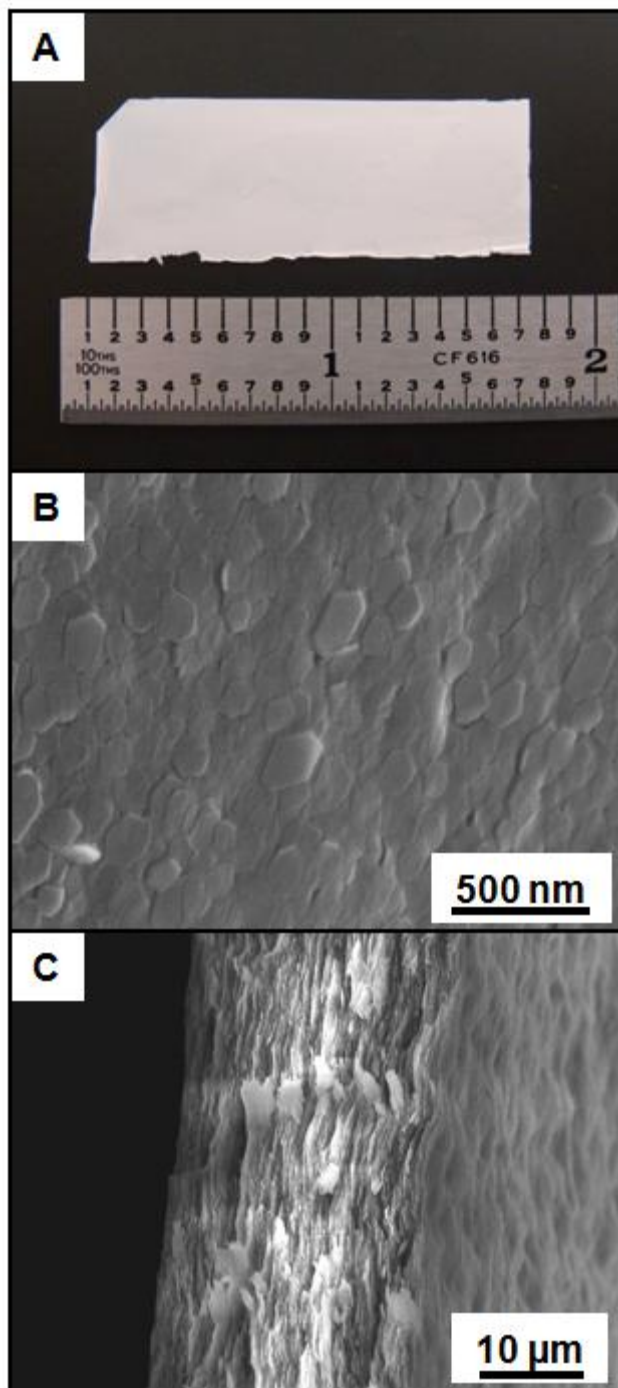


Figure 2-7. Electrophoretic assembly of gibbsite nanoplatelets. (A) Photograph of a free-standing gibbsite film. (B) Top-view SEM image of the sample in (A). (C) Cross-sectional view of the same sample.

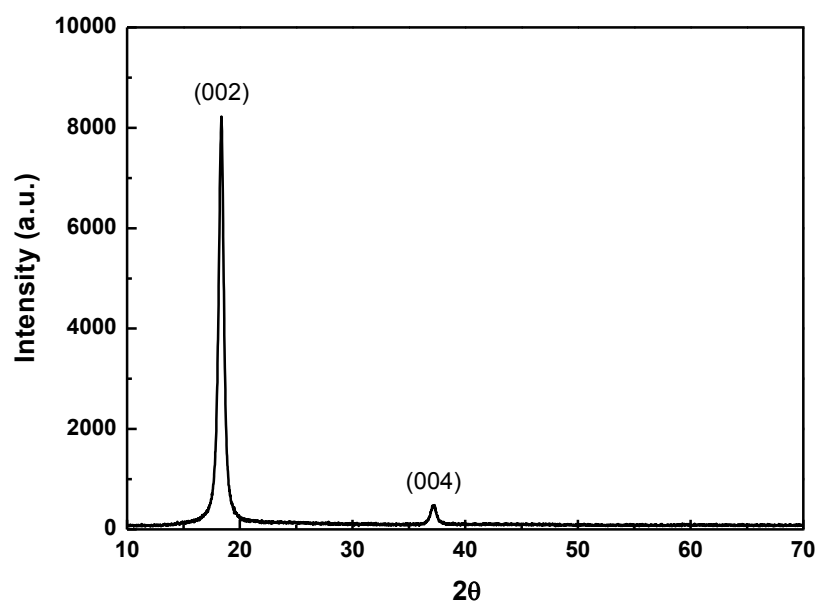


Figure 2-8. XRD patterns of the gibbsite film in Figure 2-7A.

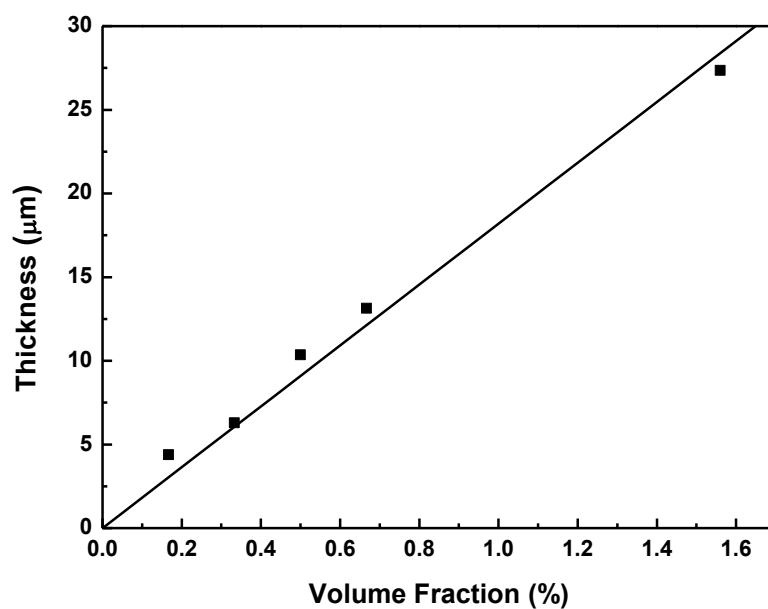


Figure 2-9. Thickness dependence of the electroplated films on the concentration of colloidal gibbsite suspensions. The thickness standard deviation for all samples is ca. 10%.

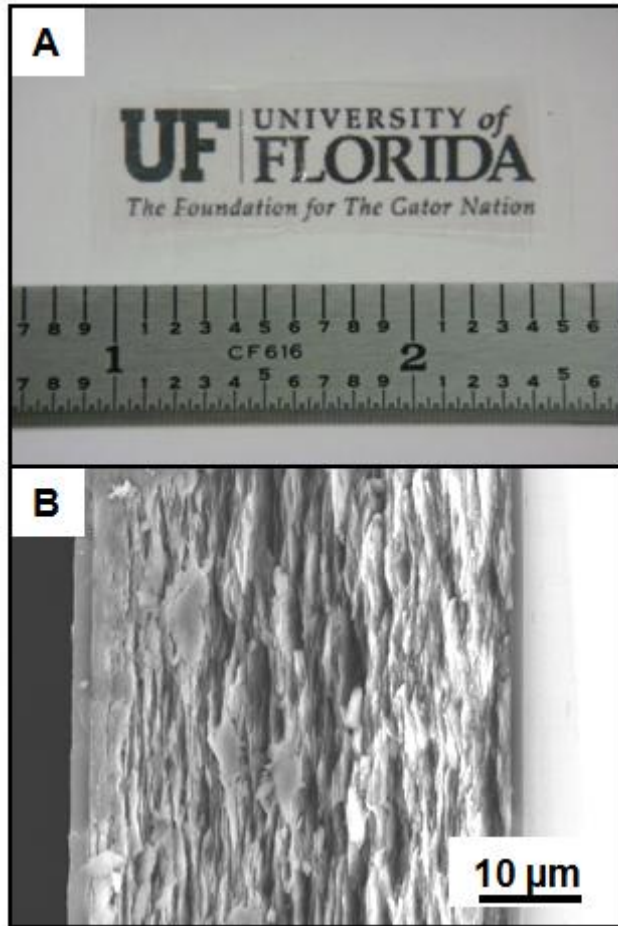


Figure 2-10. Free-standing gibbsite-ETPTA nanocomposite. (A) Photograph of a transparent film. (B) Cross-sectional SEM image of the same nanocomposite film.

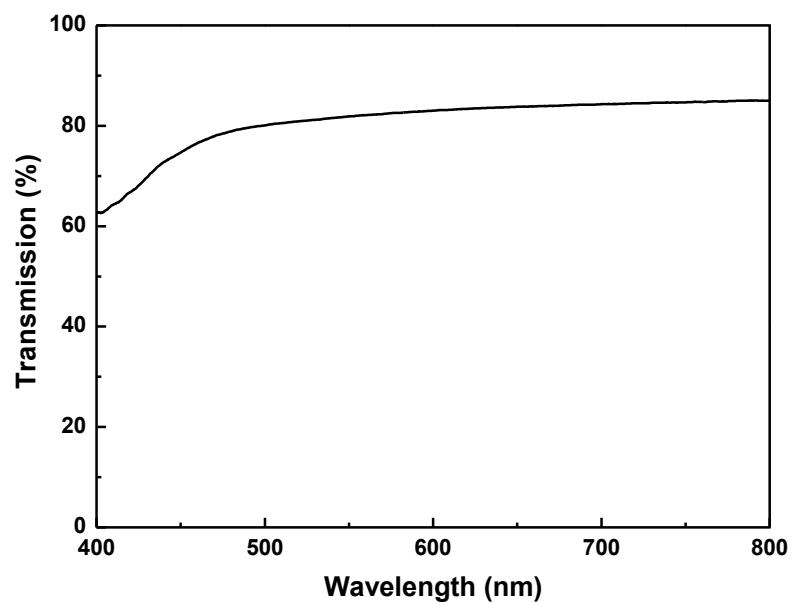


Figure 2-11. Normal-incidence transmission spectrum of the sample in Figure 2-10A.

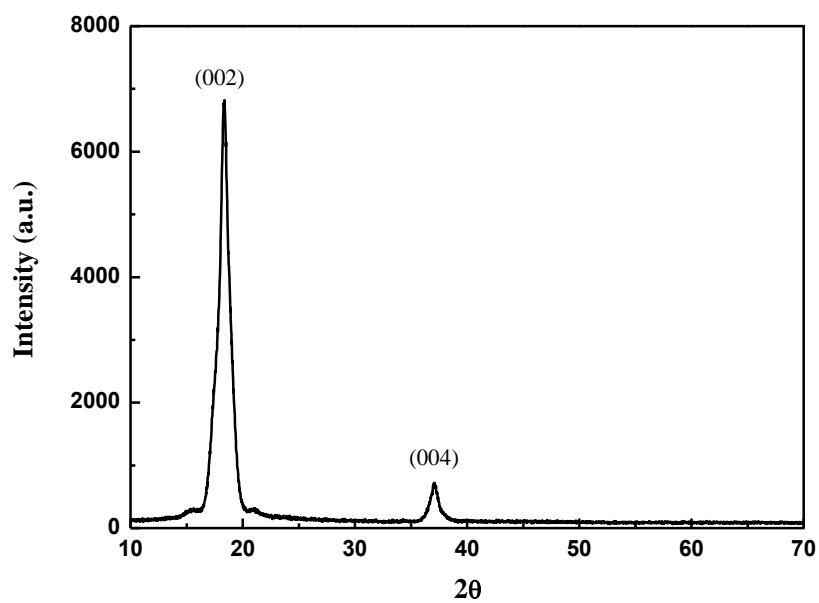


Figure 2-12. XRD patterns of the nanocomposite sample in Figure 2-10A.

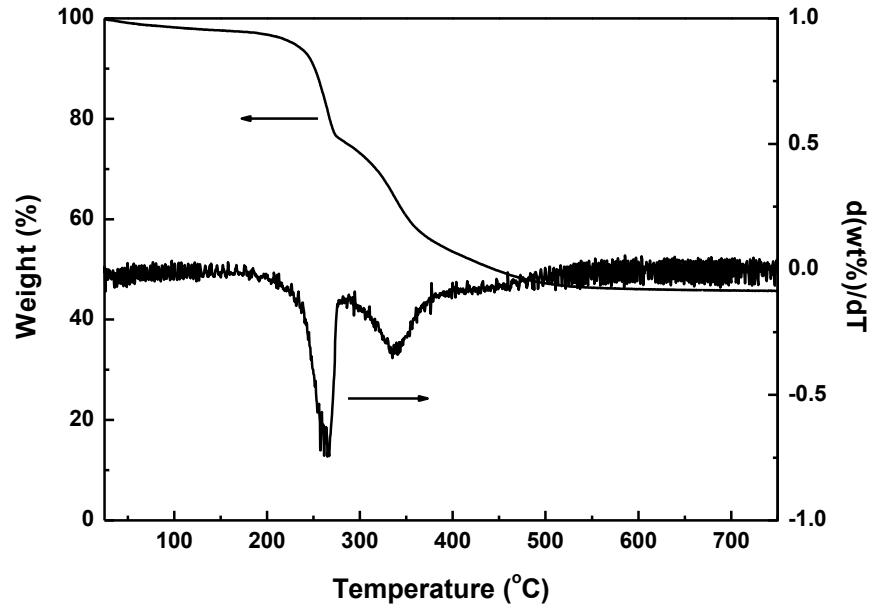


Figure 2-13. TGA of the ETPTA-Gibbsite nanocomposite as shown in Figure 2-10A.

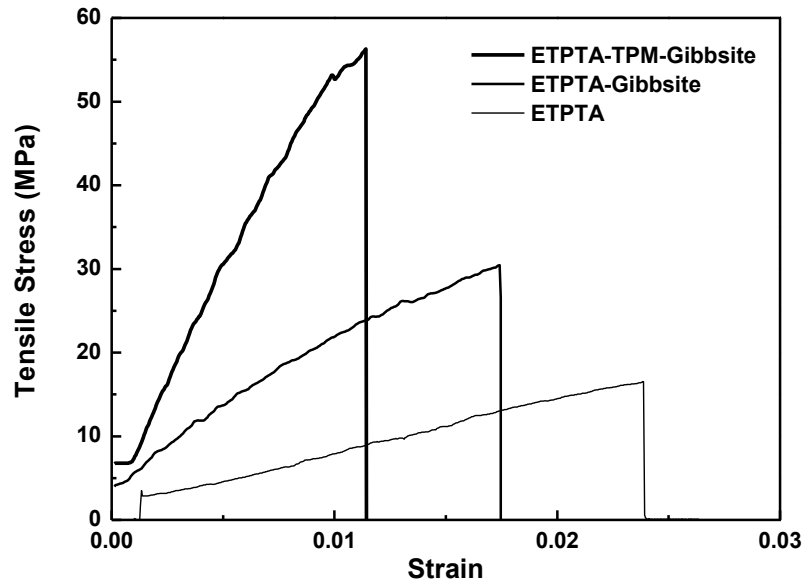


Figure 2-14. Tensile stress versus strain curves for plain ETPTA film, ETPTA-Gibbsite nanocomposite, and ETPTA-TPM-Gibbsite nanocomposite.

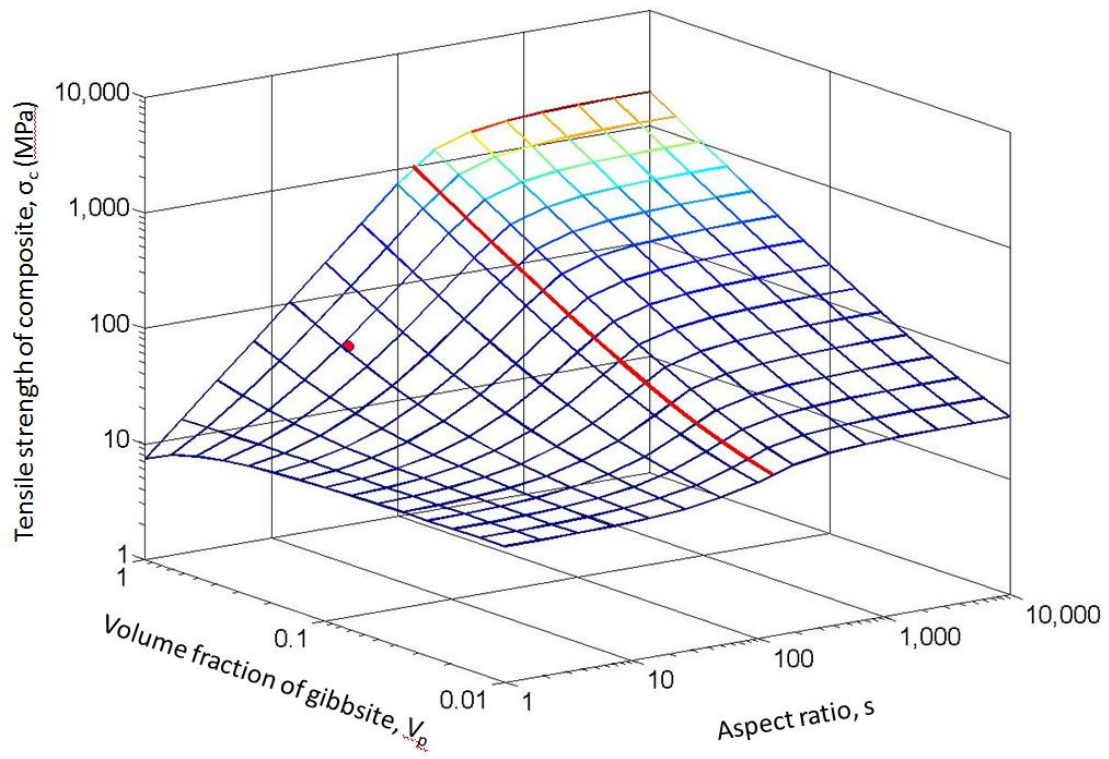


Figure 2-15. Tensile strength of composites as functions of volume fraction and aspect ratio of gibbsite nanoplatelets.

CHAPTER 3 ELECTROPHORETIC CO-DEPOSITION OF POLYMER-GIBBSITE COMPOSITES

Background

In Chapter 2, we have demonstrated a simple and rapid electrodeposition technology for assembling gibbsite nanoplatelets into large-area, self-standing films. The interstitials between the assembled nanoplatelets can then be infiltrated with polymer to form optically transparent nanocomposites. In Chapter 3, we will show a simple electro-co-deposition technology that enables the creation of inorganic-organic nanocomposites with oriented layered nanostructures in a single step. The electrodeposited inorganic-organic nanocomposite films are optically transparent and flexible, even though the weight fraction of the brittle inorganic phase is higher than 80%.

We will also show the assembly of nanocomposites with similar organic/inorganic weight ratio and ordered multilayered structure as naces by using the proposed co-deposition method. The novelty of the technology is that the positively charged nanoplatelets and polyelectrolytes are both electrophoretically attracted by the applied direct-current electric field and then simultaneously deposited on the cathode to form ordered nanocomposites. The mechanical properties of these biomimetic nanocomposites and the colloidal stability of the nanoplatelet-polyelectrolyte dispersions have also been investigated.

Experimental

EPD of Nanoplatelets

EPD of nanoplatelets is performed in a water-ethanol mixture in a sandwich cell placed horizontally. The bottom and the top of the cell are either an ITO or a gold

electrode. The gold electrode is prepared by sputtering deposition of 20 nm of titanium and 200 nm of gold on a glass slide. PDMS is used as a spacer to get an active area of $1.5 \times 1.5 \text{ cm}^2$ and a cell gap of 2.2 mm.

EPD of PVA-Gibbsite nanoplatelets

To prepare the electrophoretic bath solution, 1 ml of 5 wt.% polyvinyl alcohol (PVA, Mw 89,000 ~ 98,000, Sigma-Aldrich) aqueous solution was firstly mixed with 9 ml of 2 wt.% gibbsite nanoplatelet solution. Twenty milliliters of 200-proof ethanol was then added into the above suspension. The bottom and the top of the cell were an ITO working electrode and a gold counter electrode, respectively. A constant voltage of -2.5 V (ITO vs. Au electrode) was applied to deposit gibbsite nanoplatelets on the ITO cathode. After the EPD, the as-deposited PVA-gibbsite film was dried in an oven at 80°C .

EPD of PEI-Gibbsite nanoplatelets

Electrophoretic bath solution was prepared by mixing 2 ml of 0.3 wt.% polyethylenimine (PEI, Mw ~750,000, Sigma-Aldrich) aqueous solution, 3 ml of 2.0 wt.% gibbsite nanoplatelet aqueous solution, and 10 ml of 200-proof ethanol. Gold electrodes were served as both working and counter electrodes. Constant current of 0.3 mA was applied for 15 min to deposit gibbsite nanoplatelets and PEI on the bottom gold cathode. After EPD, the as-deposited PEI-gibbsite nanocomposite was dried in air.

Results and Discussion

Electrophoretic Co-deposition of PVA-Gibbsite

As the synthesized gibbsite platelets have positively charged surfaces and almost electrically neutral edges due to their different isoelectric point (pH 10 and 7, respectively), they tend to re-orient in the electric field with their surfaces facing the ITO

electrode. The high-molecular weight PVA (Mw 89,000-98,000) is neutrally charged in the electrophoretic bath. They can be absorbed on the surfaces of gibbsite nanoplatelets and function as water-soluble binders to cement electrodeposited ceramic particles together. Ethanol (~50% of total volume) is also added to the aqueous colloidal suspensions to reduce the dielectric constant of the solvent, and thus reduce the electrical double-layer thickness of the particles to further promote colloidal coagulation on the ITO cathode.

Figure 3-1A shows a photograph of a PVA-Gibbsite nanocomposite formed on an ITO cathode. The film can be easily peeled off from the electrode surface by using a sharp razor blade. The resulting self-standing film is flexible and transparent. Optical transmission measurement at normal-incidence (not shown here) shows the film exhibits 60-80% transmittance for most of the visible wavelengths. Top-view SEM image in Figure 3-1B illustrates the gibbsite nanoplatelets are preferentially oriented with their crystallographic c-axis perpendicular to the electrode surface. It is very rare to find edge-on platelets.

The ordered layered structure is clearly evident from the cross-sectional SEM images as shown in Figure 3-1C and D. The oriented assembly of high-aspect ratio gibbsite nanoplatelets is further confirmed by XRD. Figure 3-2 displays a XRD spectrum of an electrodeposited PVA-Gibbsite nanocomposite on an ITO electrode. The diffraction peaks from (222), (400), (441), and (662) planes of the ITO substrate are clearly appeared. Other than ITO diffraction peaks, we only observe (002) and (004) peaks from gibbsite single crystals. As the crystallographic c-axis of single-crystalline gibbsite is normal to the platelet surfaces, the (002) and (004) reflection are from

gibbsite platelets oriented parallel to the electrode surface. This strongly supports the macroscopic alignment of gibbsite nanoplatelets in the electrophoretically deposited nanocomposites. Analysis of the half-height width of the (002) and (004) peaks with the Scherrer equation (46) yields an average platelet thickness of 10.3 nm, agreeing with cross-sectional SEM measurement.

The current EPD technology enables large-scale assembly of ordered nanocomposite films in a very short time. Figure 3-3 shows the relationship between the measured weight of deposits on ITO cathode and the electrophoretic duration. A weight plateau is reached in ca. 8 min. Experimental observation shows almost all gibbsite nanoplatelets have already been deposited in this time interval and the electrophoretic bath changes from turbid to clear. The electrophoretic velocity of gibbsite nanoplatelets is estimated to be $\sim 8.2 \mu\text{m/s}$ by using the Smoluchowski's equation. For a 2.16 mm thick sandwich cell, the estimated time to deposit all particles on the ITO electrode is ca. 5 min, reasonably agreeing with the experimental observation.

The weight fraction of the inorganic phase in the electrodeposited nanocomposites can be determined by TGA. Figure 3-4 shows the TGA curve and the corresponding weight loss rate for the nanocomposite film as shown in Figure 3-1A. An apparent thermal degradation process occurs at $\sim 250^\circ\text{C}$ that corresponds to the degradation of the PVA matrix and the decomposition reaction of gibbsite. Based on the residue mass percentage (53.96%) and assuming the ash is solely Al_2O_3 , we can estimate the weight fraction of gibbsite nanoplatelets in the original nanocomposite film to be 0.825.

Electrophoretic Co-deposition of PVA-Gibbsite

PEI, which is a weak polyelectrolyte and contains amine groups, is positively charged under the electrophoretic conditions. The gibbsite nanoplatelets with a small

amount of PEI are well dispersed in a water-ethanol mixture solution due to the electrostatic repulsion between particles. However, adding a larger amount of PEI leads to the agglomeration of gibbsite nanoplatelets. To allow the electrophoresis at a controlled deposition rate, as well as the formation of ordered layered structure, gibbsite nanoplatelets must be stabilized in suspensions. We therefore study the influence of the PEI concentration on the stability of gibbsite by measuring particle size distribution and zeta-potential.

To prepare the testing solution, $(6 - n)$ ml of 2.0 wt.% gibbsite solution is mixed with n ml of 0.3 wt.% PEI aqueous solution, where $n = 0-5$. The weight ratio (PEI to gibbsite, R) is calculated as $(n \times 0.3)/[(6 - n) \times 2]$. Fig. 3-5 shows the size distribution of gibbsite nanoplatelets at different R values measured by laser diffraction. The average diameter of the as-synthesized gibbsite nanoplatelets ($R = 0$) is 150 nm (Figure 3-5A), which is smaller than that observed from TEM images in Chapter 2. The random mismatch of the surface of nanoplatelets to the incident laser beam reduces the effective diffraction area, resulting in a smaller average diameter. Figure 3-5B shows that no significant change in the particle size distribution is observed when a small amount of PEI is added ($R = 0.03$). However, further increasing of PEI concentration, as shown in Figure 3-5C and D ($R = 0.075$ and 0.75 , respectively), leads to a larger particle diameter resulting from the flocculation of nanoplatelets. The flocculation at high polyelectrolyte concentration can be explained by the increase in ionic strength, which leads to the decrease in the electrical double-layer thickness and the instability of the colloids (47). Depletion flocculation also plays an important role. At a high polymer concentration, the polymer concentration gradient between the inter-particle gap and

the remainder of the solution generates an osmotic pressure difference, forcing solvent flows out of the gap until particles flocculate (48).

Electrophoretic mobility and zeta-potential of nanoplatelets in PEI-Gibbsite suspensions with different R values are shown in Figure 3-6. Zeta-potential is obtained by fitting experimental data using Smoluchowski's model. The increase of the electrophoretic mobility and zeta-potential when a small amount of PEI is added (R from 0 to 0.03) is due to the contribution of highly charged PEI that possesses a zeta-potential of $\sim +60$ mV in water at neutral pH. Further increasing of PEI concentration results in the decreasing of electrophoretic mobility and zeta-potential due to the particle flocculation as shown in Figure 3-5.

As gibbsite nanoplatelets have positively charged surfaces (IEP ~ 10) and almost neutral edges (IEP ~ 7) under the electrophoretic conditions (pH ~ 7), the electrical force tends to re-orient the nanoplatelets to face the cathode. The positively charged PEI molecules are also electrophoretically migrated toward the cathode together with gibbsite and simultaneously sandwiched between nanoplatelets, forming PEI-Gibbsite nanocomposite. The addition of ethanol reduces the effective dielectric constant of the solvent, promoting particle coagulation by suppressing the electrical double-layer thickness of the nanoplatelets. The high pH near the cathode due to cathodic reactions also helps to coagulate nanoplatelets, as well as neutralize the protonated PEI macromolecules. Top-view SEM images in Figure 3-7A and B show that the electrodeposited nanoplatelets are preferentially oriented with their crystallographic c-axis perpendicular to the electrode surface. The hexagonal shape and the size of the platelets can be clearly seen in Figure 3-7B. Cross-sectional SEM images showed in

Figure 3-7C and D provide further evidence of the ordered layered structure. XRD spectrum of the PEI-Gibbsite nanocomposite on an Au electrode is shown in Figure 3-8. The diffraction peak from the (002) plane of gibbsite single crystals is clearly appeared. Comparing to our previous results, which show diffraction peaks from both (002) and (004) planes of gibbsite crystals, the weaker diffraction peak from (004) plane is overlapped with the strong diffraction peak of Au. The (004) diffraction peak can be clearly seen by simply replacing Au electrode with Pt (not shown here). As the (002) and (004) diffraction are originated from gibbsite platelets oriented parallel to the electrode surface, the oriented assembly of high-aspect-ratio nanoplatelets is further confirmed.

TGA is carried out to determine the weight fraction of the organic phase in the nanocomposites shown in Figure 3-9. An apparent thermal degradation process occurs at $\sim 250^{\circ}\text{C}$ that corresponds to the degradation of the polymer matrix and the decomposition reaction of gibbsite. Based on the residual mass percentage (63.7%) and assuming the ash contains only Al_2O_3 , the weight fraction of PEI in the nanocomposite film is estimated to be ~ 0.03 , which is close to the organic content of natural nacre consisting of less than 5 wt.% of soft biological macromolecules (19).

The mechanical properties of the electrodeposited nanocomposites are evaluated using nanoindentation. In a nanoindentation test, a diamond Berkovich indenter is forced perpendicularly into the coating surface. The load-displacement profile is then used to calculate the reduced modulus, E_r , using the Oliver-Pharr method (49). Figure 3-10 shows the E_r as a function of contact depth obtained from the nanoindentation tests. The observed E_r is in the range of 2.20-5.17 GPa, which is comparable to those of

ordered artificial nacles prepared by centrifugal deposition (31) and LBL assembly (50). The decrease in E_r with increasing contact depth may be related to the indentation size effects. The size effects are explained as a result of deformation, which originates mainly from crack propagation for ceramics, and factors such as surface roughness, interaction between inorganic and organic phases, and other structural details of the coatings (51, 52). The E_r of PEI-Gibbsite nanocomposite is ~ 0.4 GPa lower than that of pure gibbsite coating, showing the effect of the soft PEI layers in between the hard gibbsite nanoplatelets (53).

Summary

We have developed a scalable EPD technology for rapid production of nacre-like inorganic-organic nanocomposites in a single step. The applied direct-current electric field enables the preferential alignment of gibbsite nanoplatelets and the co-deposition of non-ionic-type polymer between the inorganic nanosheets. The resulting self-standing nanocomposite films contain high-weight percentage of inorganic platelets, but are still optically transparent and flexible. The co-deposition technology is readily applicable to many cationic polyelectrolytes, such as poly(diallyldimethylammonium chloride) (PDDA) and poly(allylamine hydrochloride) (PAH), gibbsite nanoplatelets with larger size, and even silica-coated gibbsite particles.

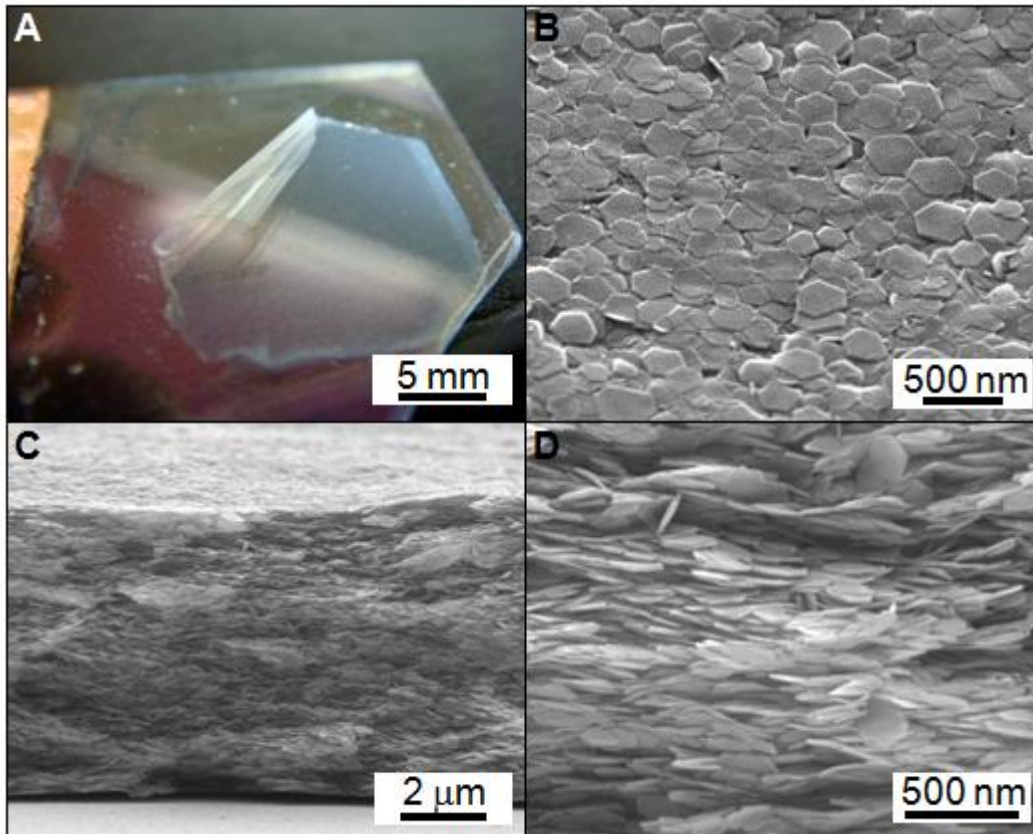


Figure 3-1. Electrodeposited PVA-Gibbsite nanocomposite. (A) Photograph of a composite film on an ITO electrode. (B) Top-view SEM image of the sample in (A). (C) Cross-sectional SEM image of the sample in (A). (D) Magnified cross-sectional image.

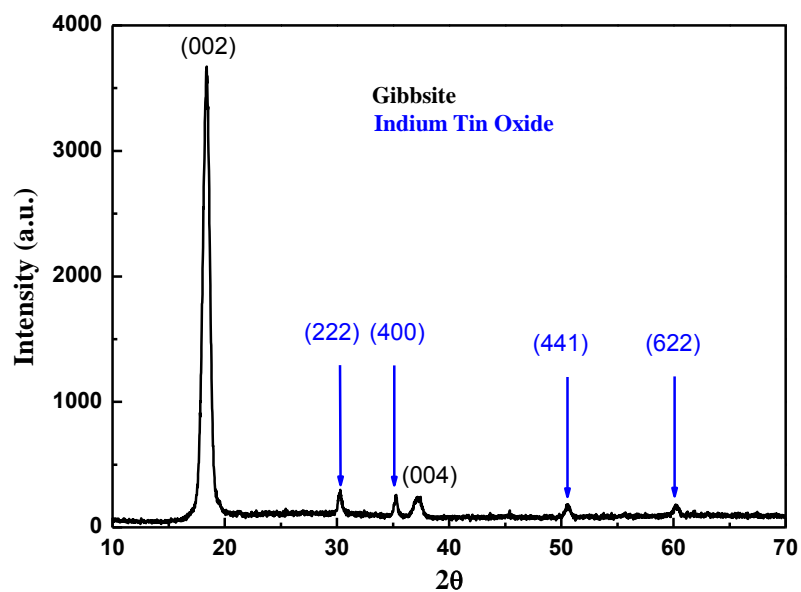


Figure 3-2. XRD patterns of an electrodeposited PVA-gibbsite composite on ITO electrode.

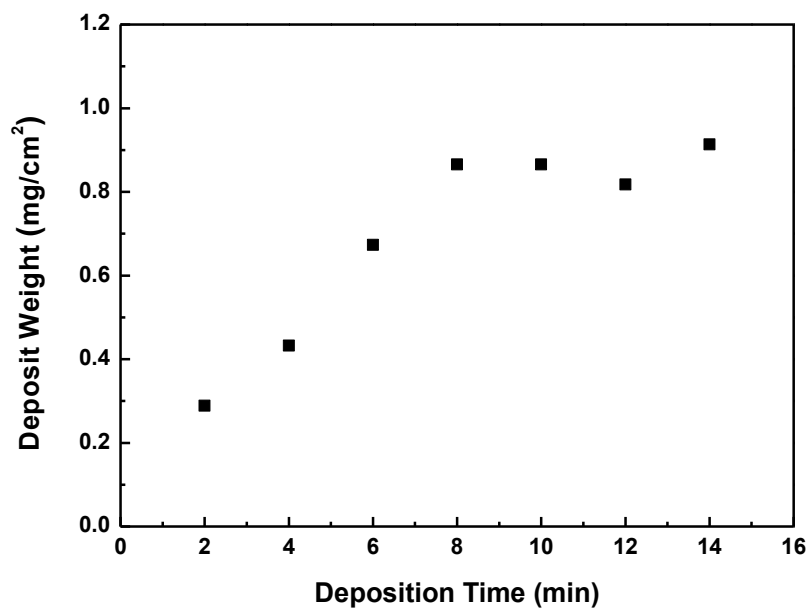


Figure 3-3. Deposit weight on ITO electrode versus electrophoretic duration.

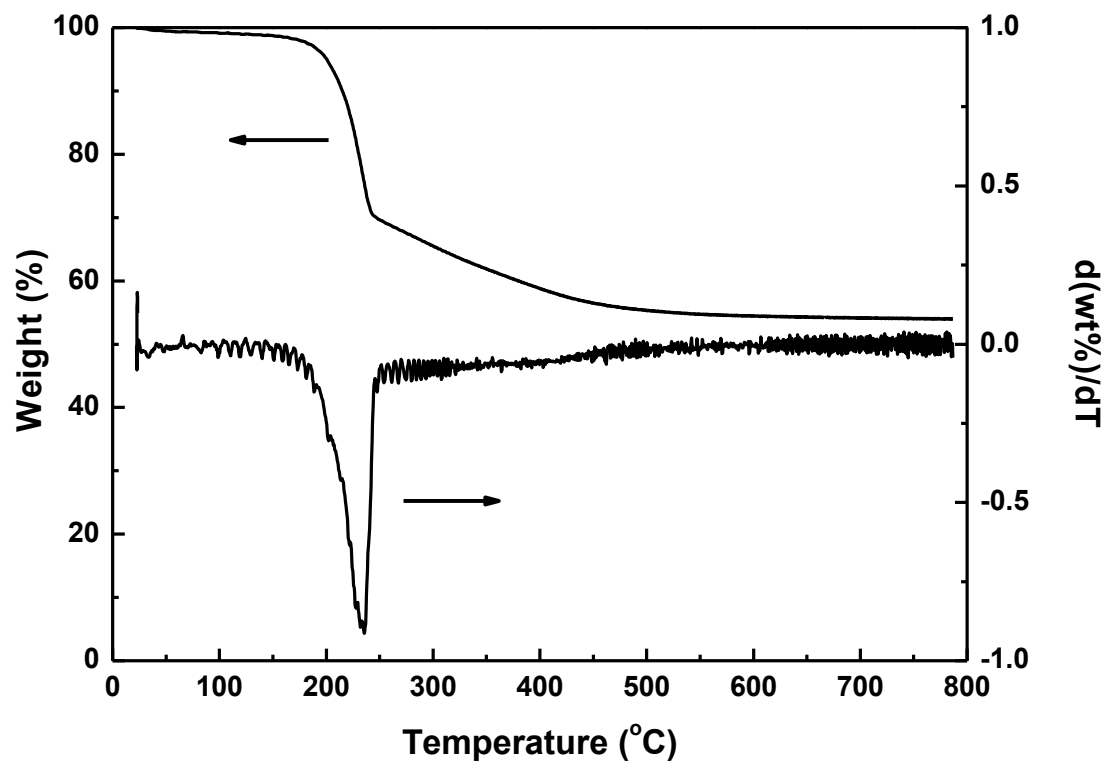


Figure 3-4. TGA of the nanocomposite sample as shown in Figure 3-1A.

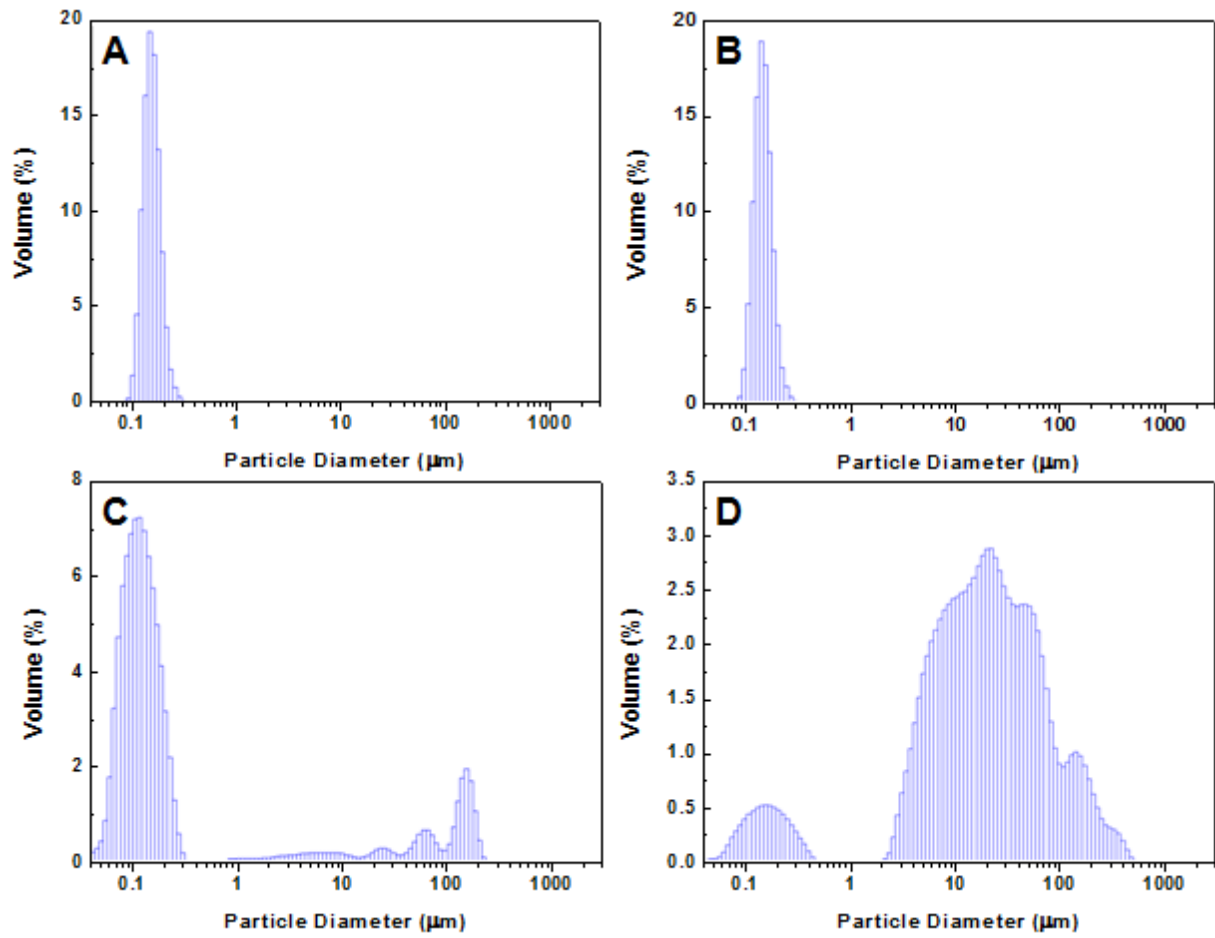


Figure 3-5. Particle size distribution of nanoplatelet suspensions at different PEI/gibbsite weight ratio. (A) $R = 0$, (B) $R = 0.03$, (C) $R = 0.075$, and (D) $R = 0.75$.

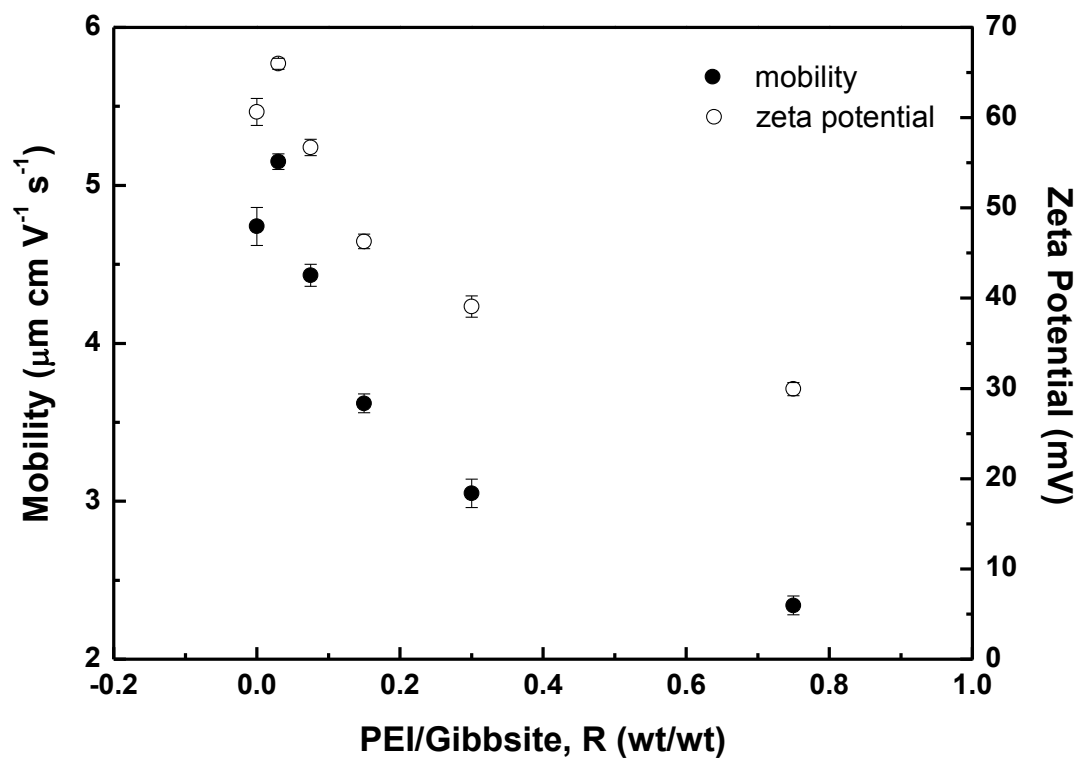


Figure 3-6. Electrophoretic mobility and corresponding zeta-potential of nanoplatelets at different PEI/gibbsite weight ratio.

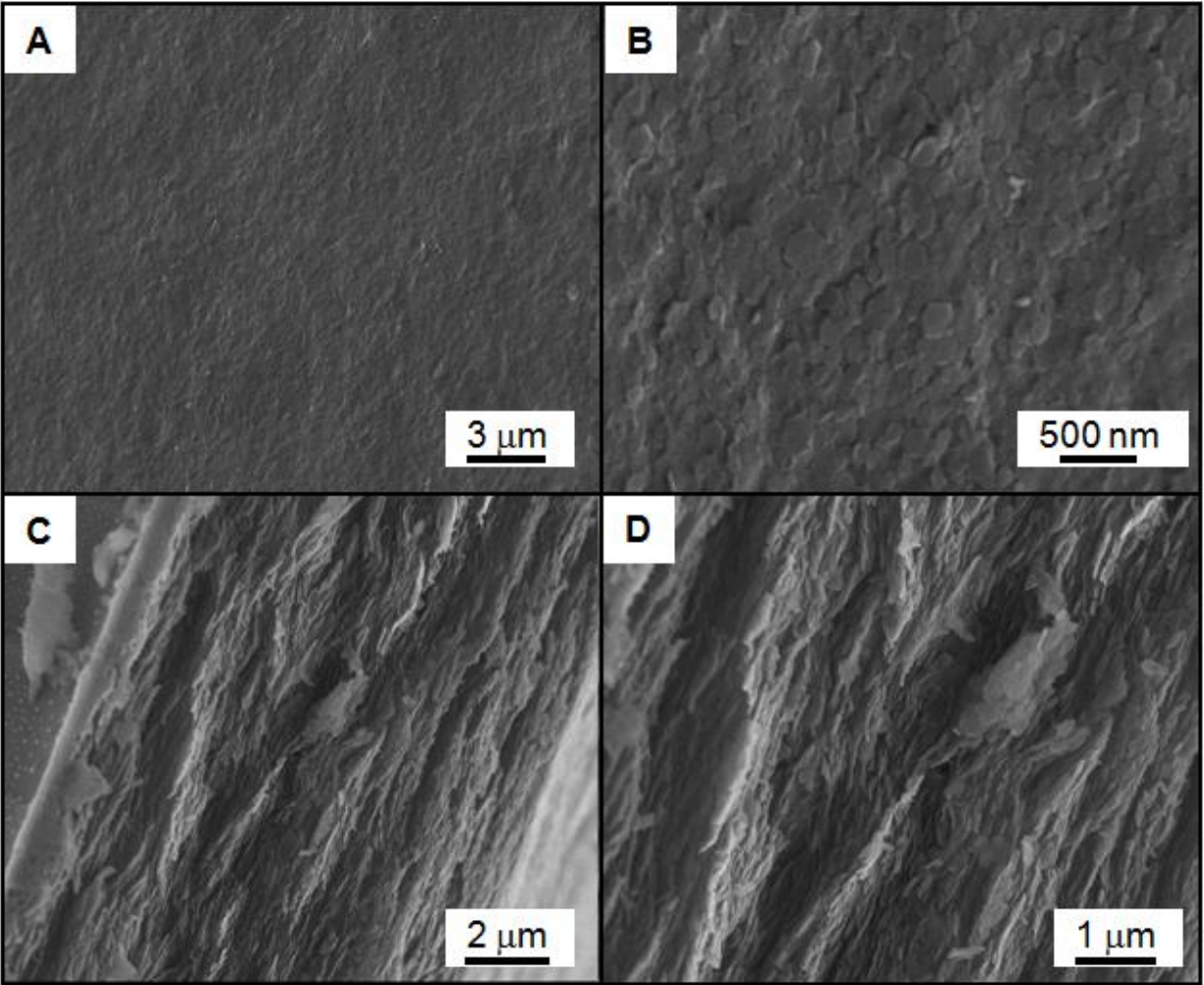


Figure 3-7. SEM images of PEI-Gibbsite nanocomposite. (A) Top-view image, (B) magnified top-view image, (C) cross-sectional image, and (D) magnified cross-sectional image.

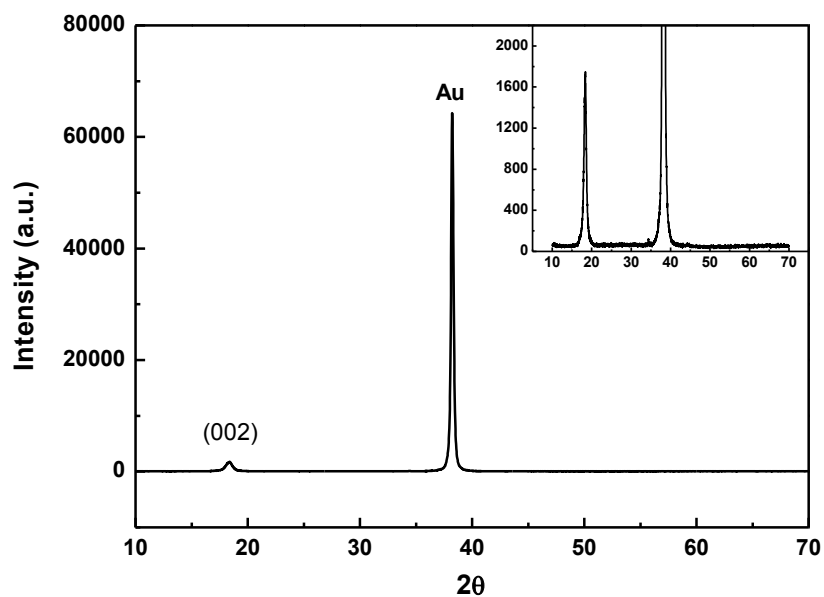


Figure 3-8. XRD patterns of an electrodeposited PEI-Gibbsite nanocomposite on Au electrode.

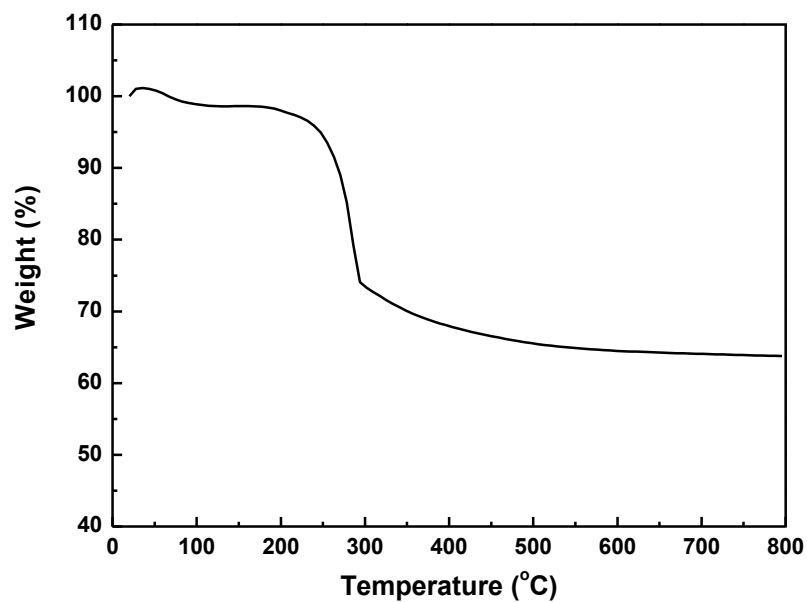


Figure 3-9. TGA of an electrodeposited PEI-Gibbsite nanocomposite.

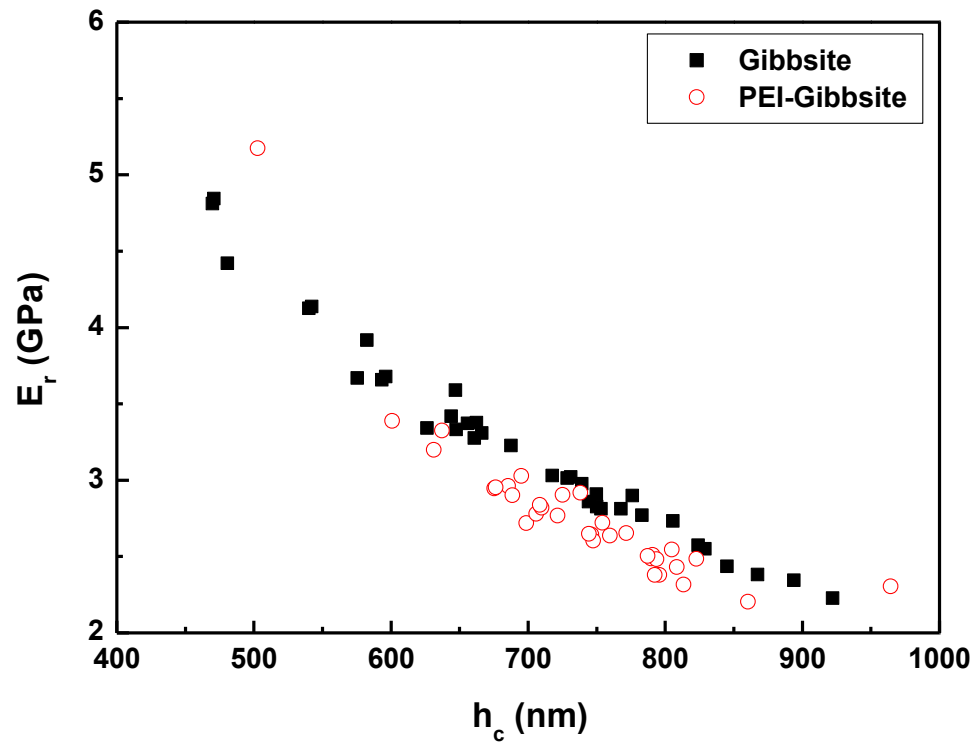


Figure 3-10. Reduced modulus of pure gibbsite and PEI-Gibbsite nanocomposite measured by nanoindentation.

CHAPTER 4 ELECTROPHORETIC ASSEMBLY OF SURFACE-ROUGHENED GIBBSITES

Background

In Chapter 2, we have demonstrated that ordered assemblies of single-crystalline gibbsite nanoplatelets can be achieved by EPD and polymer-gibbsite nanocomposites are obtained by subsequent polymer infiltration. In Chapter 3, we have also shown that the co-deposition of gibbsite nanoplatelets and either non-ionic-type polymers or polyelectrolytes can be achieved by EPD. However, there is a major difference between the natural platelets found in nacres and the synthetic gibbsite nanoplatelets – i.e., the natural aragonite platelets are rough while the single-crystalline gibbsite nanoplatelets have smooth surface (37, 54). It is found that the arrangement of nano-asperities interposing (as in Figure 4-1) between neighboring lamellae plays a crucial role in determining the inter-lamellae slip and the resulting mechanical properties of the natural composites (55, 56). This is because the stress at which the inelastic deformation proceeds is governed by these nano-sized asperities on the surface of the aragonite tablets (56).

To help understand the surface roughness effect, we intend to increase the surface roughness of synthetic nanoplatelets by coating gibbsite particles with rough silica to mimic the asperity of natural aragonite. EPD of these surface-roughened nanoplatelets is carried out to form artificial nacreous coatings. Unfortunately, the shrinkage of sol-gel silica during the drying process after electrodeposition results in severe cracking. Similar drying-induced crack formation is also a detrimental factor that affects the crystalline quality of silica colloidal crystals prepared by the convective self-assembly technology (57, 58). To resolve this cracking issue, here we report a new

EPD approach to form biomimetic monolithic multilayer by reversing the surface charge of silica-coated-gibbsite (SCG) nanoplatelets using adsorbed polyelectrolytes. Different kinds of polymer nanocomposites are prepared and their mechanical properties are evaluated by tensile tests. The resulting self-standing films are transparent and exhibit significantly improved mechanical properties over those of pure polymer.

Experimental

Coating of Gibbsite Nanoplatelets with Silica

Purified gibbsite nanoplatelets are coated with a thin layer of silica by following a procedure consisting of two steps: adsorption of polyvinylpyrrolidone (PVP) and growth of silica shell in ethanol via Stöber method (59). PVP (Mw ~40,000) is first dissolved in deionized water by ultrasonication and vigorous stirring. Subsequently, 200 ml of gibbsite nanoplatelet aqueous suspension (1 wt.%) is mixed with 300 ml of PVP solution (10 wt.%). The mixture is then stirred for 1 day to ensure the complete adsorption of PVP on the gibbsite surface. To transfer PVP-coated gibbsite nanoplatelets into ethanol, the mixture is centrifuged and the sediment is redispersed in ethanol. This process is repeated for three times for the complete replacement of water with ethanol. The final volume of the PVP-modified gibbsite nanoplatelet suspension is adjusted to 500 ml. The suspension is then mixed with 33 ml of ammonium hydroxide (14.8 N) and 1 ml of tetraethyl orthosilicate (TEOS, 99+%) for the growth of silica shell. After 4-6 h of stirring, dispersions of SCG nanoplatelets are centrifuged and the sediments are redispersed in deionized water. For TEM imaging, 1 ml of HCl (37%) and 10 ml of SCG nanoplatelets (~0.1 wt.%) are mixed and stirred for 2 days to remove the gibbsite core.

EPD of Nanoplatelets

EPD of nanoplatelets (SCG and PEI-SCG) is performed in a water-ethanol mixture in a sandwich cell placed horizontally. The bottom and the top of the cell are either an ITO or a gold electrode. PDMS spacer is used to get an active area of $1.5 \times 1.5 \text{ cm}^2$ and a cell gap of 2.2 mm.

EPD of SCG nanoplatelets

The bath solution is SCG nanoplatelets dispersed in a water-ethanol mixture. 200-proof ethanol is added into 2 wt.% of aqueous suspensions of SCG nanoplatelets to make the volumetric ratio of ethanol to the aqueous suspension to be two. A constant voltage of 3.5 V (Au vs. ITO) is applied for 20 min to deposit the negatively charged SCG nanoplatelets onto the bottom gold anode. An ITO electrode is used as the top counter cathode to enable the in situ observation of the EPD process.

EPD of PEI-SCG nanoplatelets

The electrophoretic bath solution for depositing PEI-SCG nanoplatelets is prepared by mixing 9 ml of 1.5 wt.% SCG nanoplatelet aqueous suspension with 1 ml of 1.5 wt.% PEI aqueous solution. The bath solution is ultrasonicated for 30 min to minimize the agglomeration of SCG nanoplatelets. Positively charged PEI macromolecules are adsorbed on the negatively charged surface of SCG nanoplatelets due to Coulombic attraction, forming positively charged PEI-SCG nanoplatelets. A constant voltage of -2.5 V (ITO vs. Au) is applied for 20 min to deposit the positively charged PEI-SCG nanoplatelets onto the bottom ITO cathode. A gold electrode is served as the top counter anode.

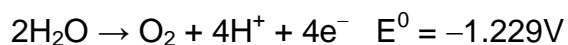
Results and Discussion

SCG Nanoplatelets

SCG nanoplatelets are synthesized by coating a thin shell of sol-gel silica on gibbsite nanoplatelet cores (59). The synthetic process consists of two steps: adsorption of PVP and the subsequent growth of silica shell via Stöber method. The amphiphilic PVP macromolecule acts as a coupling agent. It can be adsorbed onto a broad range of colloids and stabilizes them in water and various nonaqueous solvents (e.g., ethanol). The PVP-modified gibbsite nanoplatelets can be directly dispersed in ethanol for the subsequent growth of silica shell. The thickness of the silica shell can be easily controlled by adjusting the sol-gel reaction conditions (e.g., precursor concentration and reaction time) (59). To confirm the formation of silica shell, the gibbsite core of SCG nanoplatelets can be selectively removed by a hydrochloric acid wash (41). Figure 4-2A shows a typical TEM image of hollow silica nanoplatelets after selectively leaching out gibbsite cores. Dark edges in the TEM image reveal that these nanoplatelets are hollow. The arrows indicate a silica shell with a thickness of ca. 10 nm. The regular hexagonal shape and the thickness uniformity of silica shells are clearly evident from the TEM image. Additionally, by comparing the TEM image with that of gibbsite nanoplatelets in Figure 2-5, it is evident that the sol-gel-derived silica shells are much rougher than the single-crystalline gibbsite nanoplatelets. Moreover, the silica coating reverses the surface charge of gibbsite colloids and the zeta-potential of SCG nanoplatelets in ethanol is measured to be -38.1 ± 1.6 mV by using Smoluchowski's model. This further confirms that the surface of gibbsite nanoplatelets has been coated with silica which is negatively charged at neutral pH (60).

EPD of SCG Nanoplatelets

EPD of negatively charged SCG nanoplatelets is carried out in a water-ethanol mixture using a parallel-plate sandwich cell, which consists of a gold working anode on the bottom, an ITO cathode on the top, and a PDMS spacer (~2.2 mm thick). Ethanol is used to reduce the dielectric constant of the solvent and therefore decrease the electrical double-layer thickness of the SCG nanoplatelets to promote colloidal coagulation on the gold electrode. Deionized water is added to the suspension for bringing about the following anodic reaction:



which leads to a local pH decrease at the electrode surface. Since the zeta-potential of silica reduces when the solution pH decreases (60), the above anodic reaction can thus lower the surface charge of negatively charged SCG nanoplatelets to further assist colloidal coagulation. A photograph of an electrodeposited SCG film on a gold electrode is shown in Figure 4-2B. In sharp contrast to the electrodeposited gibbsite films which are monolithic and crack free, cracks can be easily formed on the SCG film during the drying process after electrodeposition. We attribute the formation of cracks to the excess stress induced by the shrinkage of sol-gel silica shell of SCG nanoplatelets. It is well-known that the drying of Stöber silica spheres during the convective self-assembly process leads to cracks in the resulting colloidal crystal films (57, 58). To eliminate shrinkage-induced cracks, one common approach is to sinter sol-gel silica at high temperature (>500°C) (58). However, this approach cannot be used for SCG nanoplatelets as gibbsite cores will be thermally decomposed at ~300°C as addressed in Chapter 2.

PEI-SCG Colloidal Stability

To resolve the cracking issue, we pursue a new approach by adding PEI to the electrophoretic bath in order to increase the adherence and strength of the electrodeposited films. PEI, which is a weak polyelectrolyte with the molecular structure shown in the inset of Figure 4-3 ($pK_a \sim 10.5$), is positively charged under the electrophoretic conditions ($pH \sim 6$) due to the possessing of multiple amine functional groups. It also acts as a particle binder because it adsorbs strongly onto silica at a wide range of pH values (48). Therefore, positively charged PEI macromolecules are adsorbed on the negatively charged surface of SCG nanoplatelets via Coulombic attraction, forming positively charged PEI-SCG nanoplatelets. However, adding a large amount of PEI leads to the flocculation of SCG nanoplatelets.

To investigate the colloidal stability of PEI-SCG nanoplatelets in suspensions as well as the reversal of surface charge, the influence of the PEI concentration is studied by measuring zeta-potential of colloidal suspensions with different amount of PEI. The testing solution is prepared by mixing 4.5 g of 0.075 wt.% SCG dispersion in ethanol with 0.5 g of PEI aqueous solution at different concentration, C_{PEI} (wt.%). The mixture is ultrasonicated for 30 min to minimize the agglomeration of SCG nanoplatelets. The specific surface area of SCG nanoplatelets is calculated to be $\sim 57 \text{ m}^2/\text{g}$ by using the geometry determined from experiments and the density of gibbsite, $2.2 \text{ g}/\text{cm}^3$. The amount of PEI addition is calculated as $[(0.5 \times C_{PEI}) / (4.5 \times 0.075 \times 57)] \times 10^3 \text{ mg}/\text{m}^2$. The zeta-potential of PEI-SCG nanoplatelets as a function of the amount of PEI addition is shown in Figure 4-3. At zero PEI addition, the zeta-potential of SCG nanoplatelets is measured to be $-38.1 \pm 1.6 \text{ mV}$, showing the surface of colloids are negatively charged

and silica is coated on gibbsite cores. With the increasing of the amount of PEI, zeta-potential of SCG nanoplatelets initially reduces and becomes less negative. Further addition of PEI triggers the reversal of zeta-potential when the PEI addition is larger than 0.5 mg/m^2 . A zeta-potential plateau is reached at around $+28 \text{ mV}$ when 2 mg/m^2 of PEI is added. The formation of the plateau is caused by the saturation of adsorbed PEI macromolecules on SCG nanoplatelets. When a larger amount of PEI is added, PEI-SCG nanoplatelets tend to flocculate and zeta-potential decreases. The agglomeration of nanoplatelets at high PEI addition can be explained by depletion flocculation. At a high polymer concentration, the concentration gradient between the inter-particle gap and the remainder of the solution generates an osmotic pressure difference, forcing solvent flows out of the gap until particles flocculate (48). Flocculation of gibbsite nanoplatelets and the decreasing of zeta-potential are observed when a high concentration of PEI (26 mg/m^2) is added to SCG dispersion. To get stable SCG nanoplatelets for EPD, the amount of PEI addition is thus controlled in the range of the zeta-potential plateau at 1.54 mg/m^2 .

EPD of PEI-SCG Nanoplatelets

The cathodic electrodeposition of PEI-SCG nanoplatelets is performed using a parallel-plate cell with electric field strength of 1100 V/m . The positively charged PEI-SCG nanoplatelets are attracted toward the bottom ITO cathode by the electrical force. Gravity only plays a minor role as the sedimentation speed of PEI-SCG particles is much slower than the electrophoretic mobility. Top-view SEM images in Figure 4-4A and B show that most of the electrodeposited PEI-SCG nanoplatelets are aligned parallel to the ITO electrode surface, though a few nanoplatelets are found to orient perpendicularly as shown by the arrows in Figure 4-4B. Compared to electrodeposited

films consisting of pure gibbsite nanoplatelets, the preferential alignment of PEI-SCG nanoplatelets is slightly deteriorated. The layered structure and the slight worsening of the oriented deposition of PEI-SCG nanoplatelets are further confirmed by the cross-sectional SEM images in Figure 4-4C and D and the XRD patterns in Figure 4-5. The diffraction peaks showing (222), (400), (441), and (622) planes are from the ITO electrode. Other than ITO diffraction peaks, we observe mainly (002) and (004) peaks from gibbsite single crystals. As the crystallographic c-axis of single-crystalline gibbsite is normal to the platelet surface, the (002) and (004) diffraction peaks are from PEI-SCG nanoplatelets oriented parallel to the electrode surface (46). Low-intensity diffraction peaks, such as those from the (023) and (024) lattice planes at 45.478° and 52.219° , respectively, can also be seen from the XRD spectrum. This indicates that small amount of nanoplatelets are not aligned parallel to the electrode surface, agreeing with our SEM observation.

Unlike gibbsite nanoplatelets that have positive charges on their surfaces (IEP ~ 10) and almost neutral edges (IEP ~ 7) under the electrophoretic conditions (pH ~ 7), PEI-SCG nanoplatelets have positive charges on both surfaces and edges because of the uniform coverage of silica shell and adsorbed PEI macromolecules. The difference in the spatial distribution of surface charges distinguishes the resulting arrangement of electrodeposited PEI-SCG nanoplatelets from that of gibbsite nanoplatelets. For the latter, the electrical force tends to re-orient the nanoplatelets in the electrophoretic bath to face the cathode. The deposited gibbsite nanoplatelets are thus densely packed with their crystallographic c-axis normal to the electrode surface. By contrast, no electric-field-induced re-orientation is occurred for PEI-SCG nanoplatelets because of the

uniform distribution of surface charge. Nevertheless, most of the PEI-SCG nanoplatelets are still preferentially aligned to the electrode surface because this orientation is more energetically favorable than the perpendicular one. Another reason for the imperfect alignment of PEI-SCG nanoplatelets may come from the bridging flocculation mechanism, which allows the formation of polymer bridges between neighboring particles (48). Since the PEI macromolecules used are highly branched with high molecular weight ($M_w \sim 750,000$) and large numbers of amine groups, they are easily attached to several SCG nanoplatelets. However, this attachment could be random and the nanoplatelets in the resulting aggregates might not be aligned.

ETPTA-PEI-SCG Nanocomposites

After electrodeposition, polymer nanocomposites can be made by filling the interstitials between the PEI-SCG nanoplatelets with photocurable monomers, followed by photopolymerization. A non-volatile monomer, ETPTA, is chosen to form the ETPTA-PEI-SCG nanocomposite. The monomer with 1 wt.% of photoinitiator is first added on a PEI-SCG film on an ITO electrode and the sample is then kept under vacuum for a few hours to promote the monomer penetration. After the sample becomes transparent, it is spin-coated at 4000 rpm for 1 min to remove the excess monomer. Exposure to ultraviolet radiation is then carried out to polymerize ETPTA monomer.

The resulting ETPTA-PEI-SCG nanocomposite film is highly transparent (as in Figure 4-6) due to the matching of the refractive index between the PEI-SCG nanoplatelets and the polymer matrix. The normal-incidence transmission spectra in Figure 4-7 indicate that the ETPTA-PEI-SCG nanocomposite on an ITO electrode (ETPTA-PEI-SCG/ITO) exhibits high transmittance (>80%) for most of the visible wavelengths. This suggests that most interstitial spaces between the PEI-SCG

nanoplatelets have been infiltrated by the polymer. Free-standing ETPTA-PEI-SCG nanocomposites can be obtained by soaking ETPTA-PEI-SCG/ITO in 1 M of sodium hydroxide solution for several hours. Higher transmittance is achieved for the ETPTA-PEI-SCG nanocomposite due to the removal of the ITO electrode. Compared to the high transmittance of the ETPTA-PEI-SCG nanocomposite, the PEI-SCG film on an ITO electrode (PEI-SCG/ITO) (Figure 4-6B) shows a transmittance less than 10% for most of the visible spectrum.

The cross-sectional SEM images in Figure 4-8 show that the layered structure of the original PEI-SCG film is retained and a thin wetting layer of ETPTA (~2.5 μm thick) is observed on the surface of the nanocomposite. The red and black arrows in Figure 4-8A indicate the ETPTA wetting layer and the ITO electrode, respectively. The mechanical properties of the biomimetic polymer nanocomposites are evaluated by tensile tests. The tensile strength for plain ETPTA, ETPTA-gibbsite nanocomposite, and ETPTA-PEI-SCG nanocomposite are tested and the results are shown in Figure 4-9. Compared with pure ETPTA polymer, the ETPTA-gibbsite nanocomposite shows ~2-time higher strength and ~3-time higher modulus. For the ETPTA-PEI-SCG nanocomposite, even higher tensile strength than that of the ETPTA-Gibbsite film can be achieved. This is due to the presence of the PEI macromolecule, which acts as a binder by strongly adsorbing on the negatively charged surface of SCG nanoplatelets via Coulombic attraction. Its highly branched molecular structure also enables the interlock with cross-linked ETPTA backbone. Early studies reveal that the interfacial bonding between the ceramic fillers and the organic matrix is crucial in determining the mechanical properties of the artificial nacreous composites (8, 9). The strong ionic

bonding between the PEI macromolecules and the SCG nanoplatelets along with the natural elasticity of PEI macromolecules make the ETPTA-PEI-SCG nanocomposites have 3 to 5-time higher strain than those of pure ETPTA and ETPTA-Gibbsite nanocomposites. The higher strain could also come from the surface roughness of PEI-SCG nanoplatelets due to the silica coating and the rotation of misaligned SCG nanoplatelets under an applied tensile load. A rough estimation based on the area under the tensile stress-strain curve indicates that the energy needed to rupture the ETPTA-PEI-SCG nanocomposite is nearly one-order-of-magnitude and 6-time higher than those required to break pure ETPTA polymer and ETPTA-Gibbsite nanocomposite, respectively.

A simple calculation based on the shear lag model as in Chapter 2 is carried out to validate the measured mechanical properties. Since the volume of the adsorbed PEI on the SCG nanoplatelets is quite small, we can simply use the volume fraction of ETPTA to calculate tensile strength of the nanocomposite. From our previous TGA of ETPTA-gibbsite nanocomposites prepared by the same spin-coating technique as reported here, the volume fraction of ETPTA in the polymer nanocomposite is ~ 0.50 . Therefore the tensile strength of the nanocomposite can be estimate to be about $2.75\sigma_m$, agreeing with our experimental results.

Summary

In summary, we have developed a simple and scalable EPD technology for assembling surface-roughened inorganic nanoplatelets into organized multilayer. The adsorption of polyelectrolyte macromolecules on the surface of nanoplatelets can reverse the surface charge and simultaneously eliminate the cracks induced by the shrinkage of the sol-gel silica shell of the surface-roughened nanoplatelets during

drying. We expect this approach could be applicable to the convective self-assembly of spherical colloidal silica particles to facilitate the formation of crack-free colloidal photonic crystals.

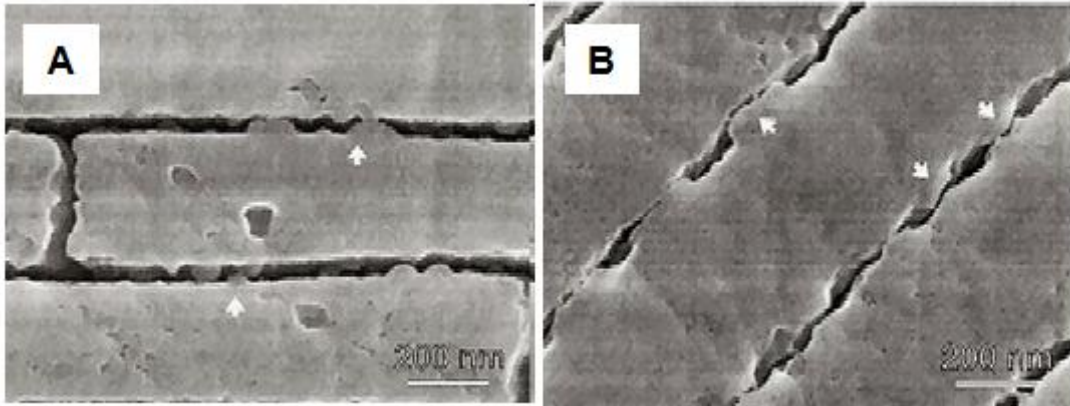


Figure 4-1. Cross section of abalone nacre showing the detailed structure at the lamellae boundaries. Arrows highlight locations where the nano-asperities interpose (56).

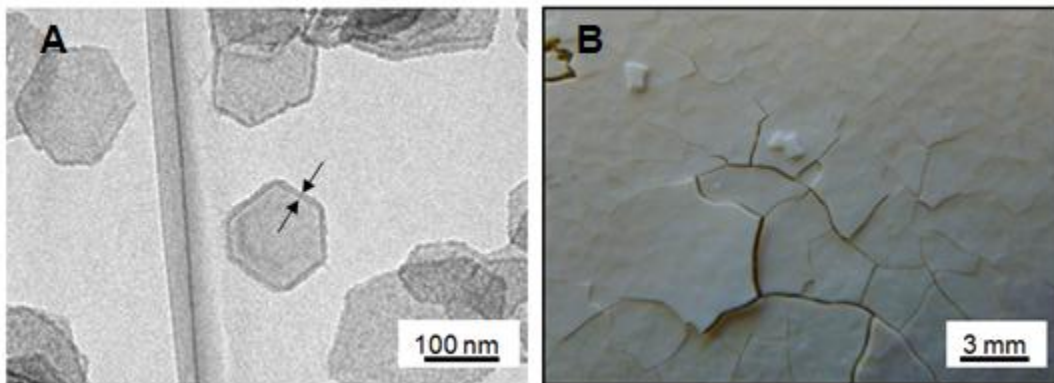


Figure 4-2. (A) TEM image of acid-leached SCG nanoplatelets. The arrows point to a silica shell with a thickness of ca. 10nm. (B) Photograph of an electrodeposited SCG film on a gold electrode.

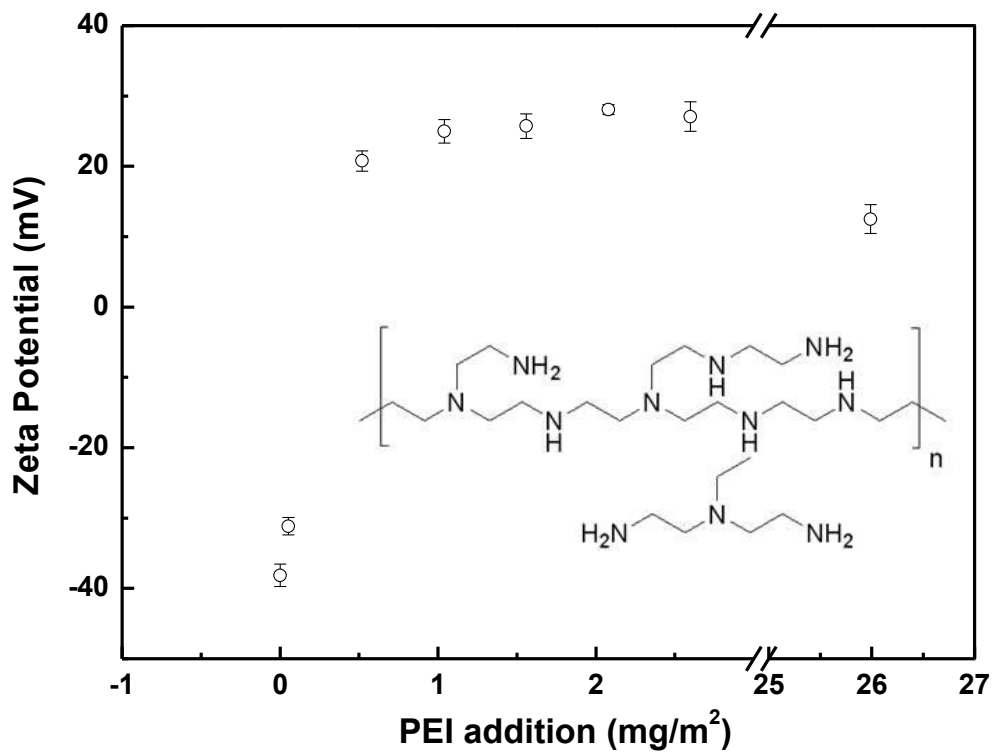


Figure 4-3. Zeta-potential of PEI-SCG nanoplatelets with different amount of PEI addition. The inset shows the molecular structure of PEI.

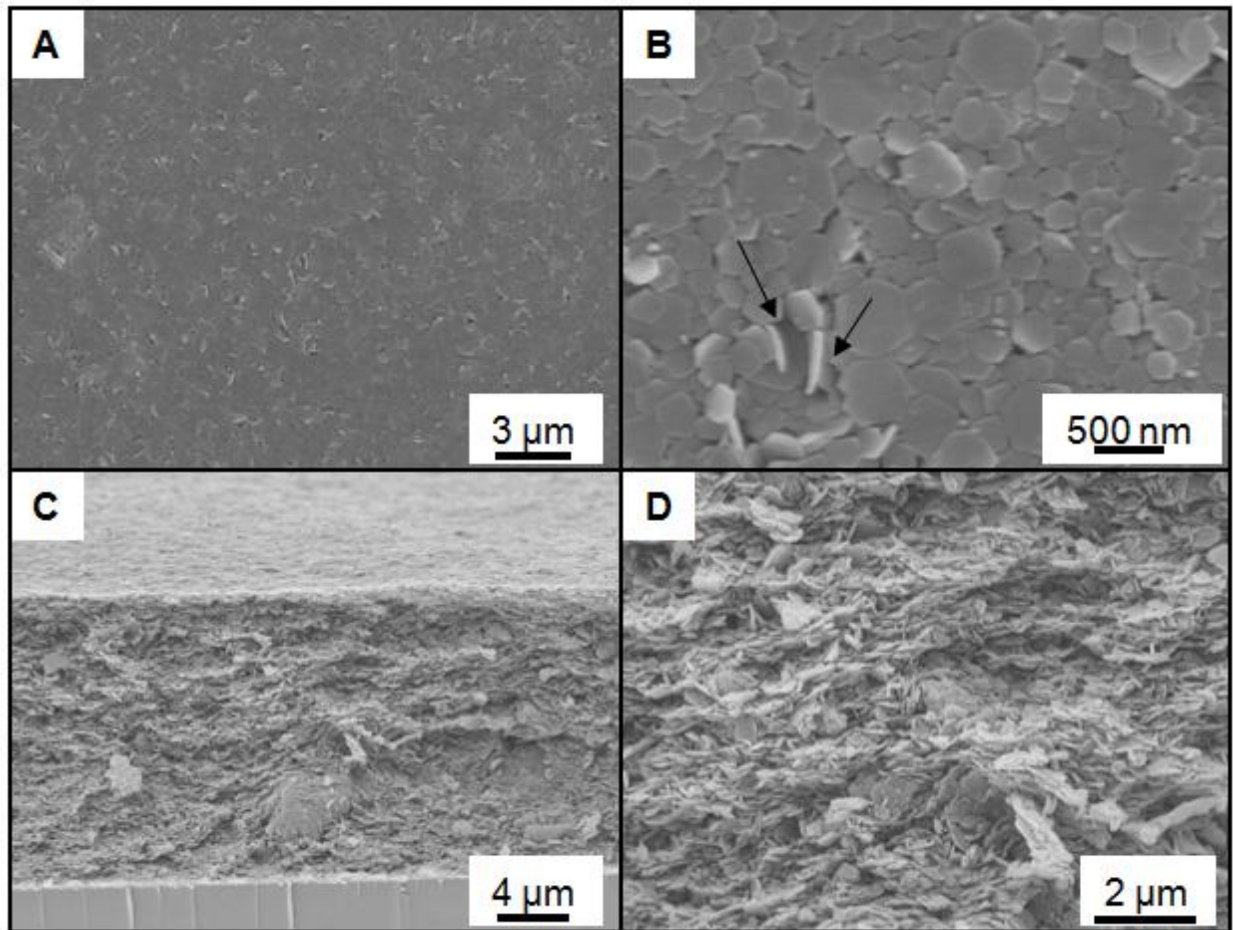


Figure 4-4. SEM images of electrodeposited PEI-SCG nanocomposite. (A) Top-view image. (B) Magnified top-view image. (C) Cross-sectional image. (D) Magnified cross-sectional image.

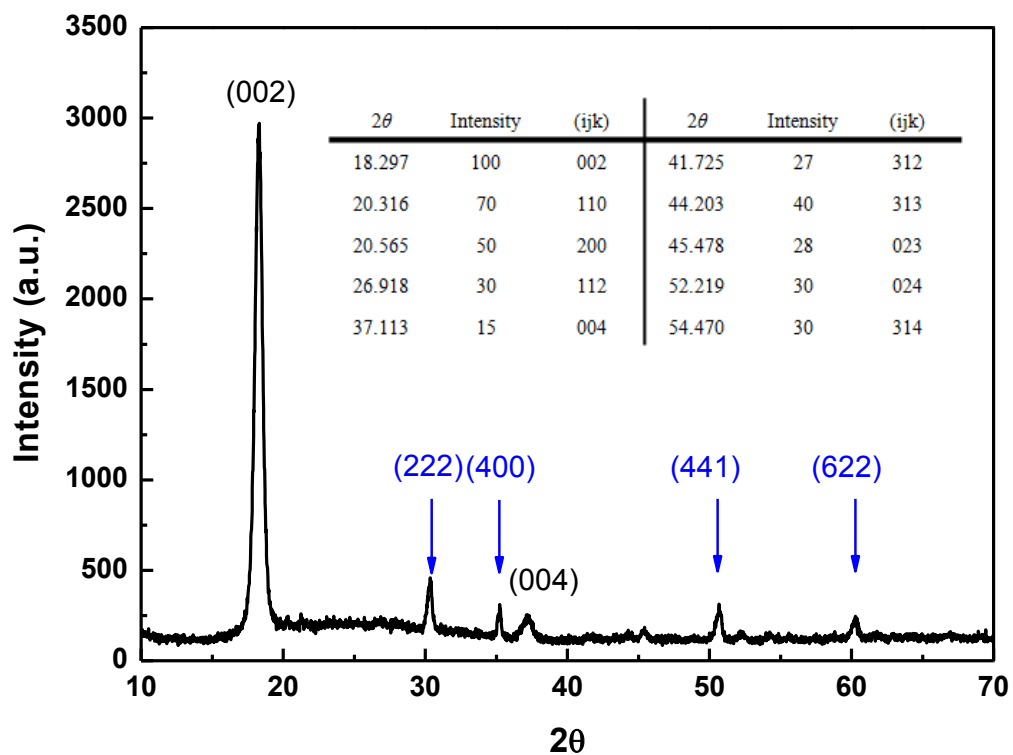


Figure 4-5. XRD patterns of a PEI-SCG nanocomposite on an ITO electrode. Blue arrows point to the characteristic peaks of ITO. The inset shows a table with major lattice planes of gibbsite.

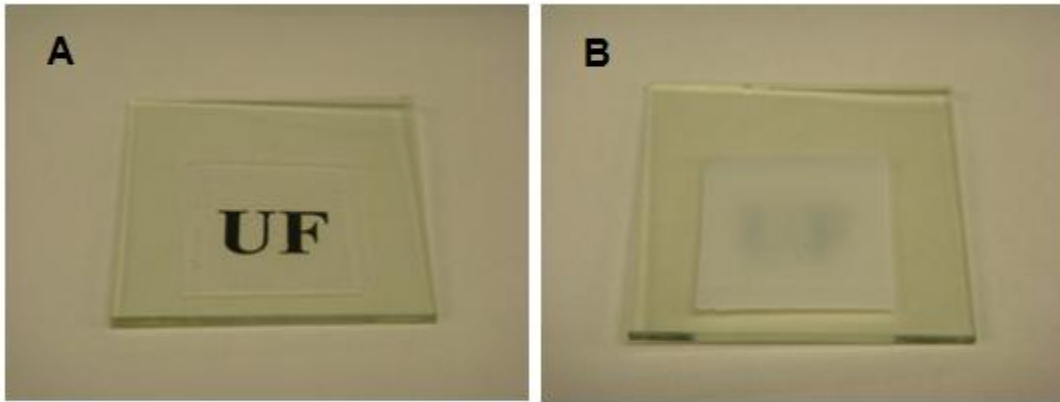


Figure 4-6. Photographs of (A) ETPTA-PEI-SCG and (B) PEI-SCG deposits on ITO electrodes.

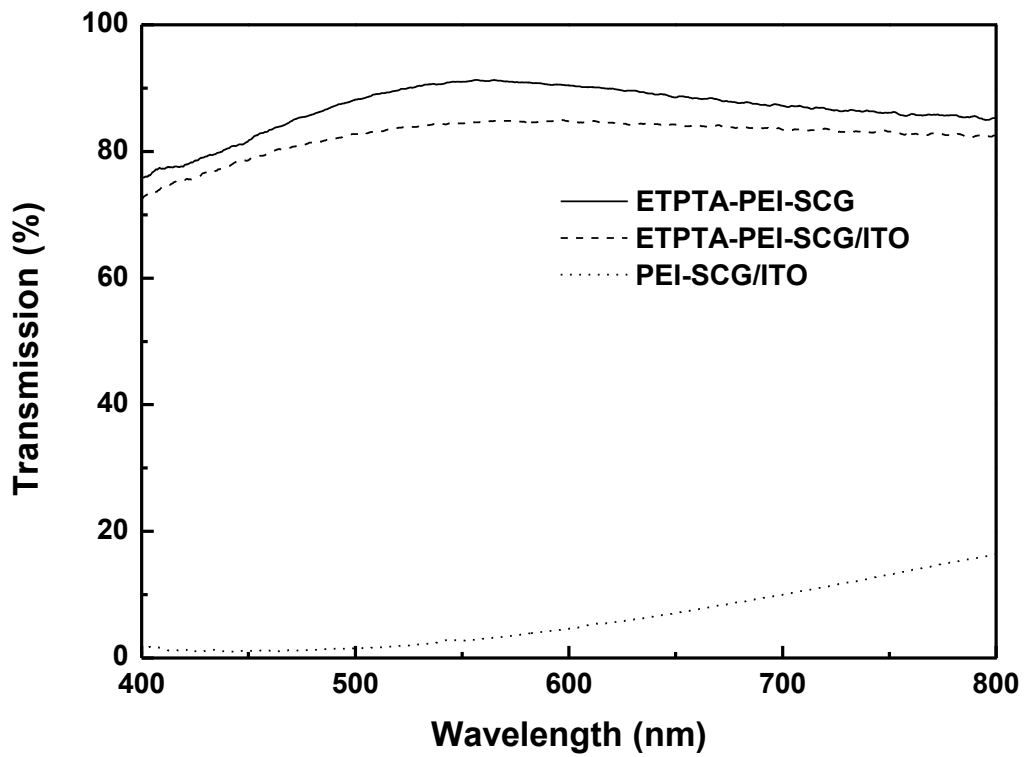


Figure 4-7. Normal-incidence transmission spectra of ETPTA-PEI-SCG nanocomposite, ETPTA-PEI-SCG nanocomposite on an ITO electrode, and PEI-SCG deposit on an ITO electrode.

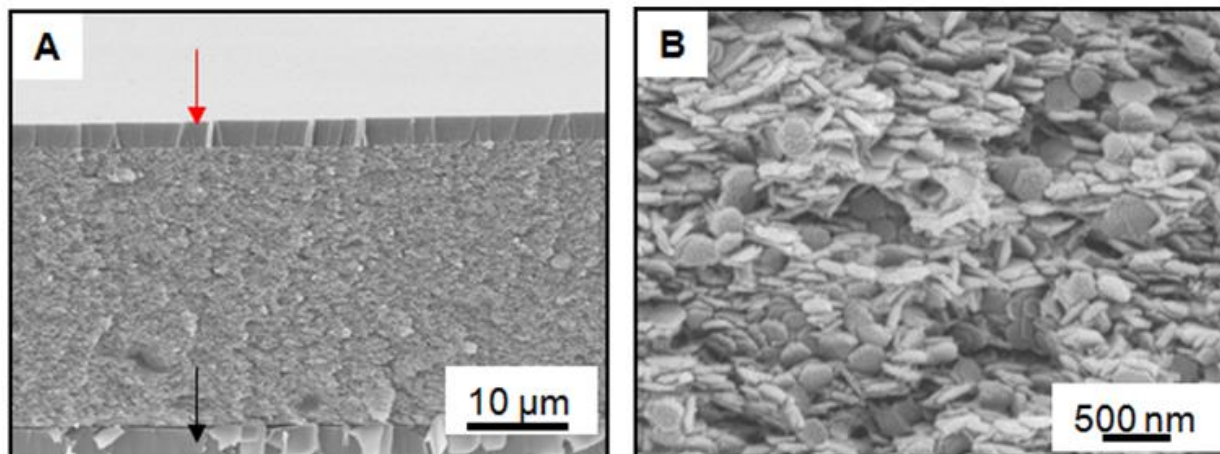


Figure 4-8. SEM images of an ETPTA-PEI-SCG nanocomposite on an ITO electrode. (A) Cross-sectional image. (B) Magnified cross-sectional image. Red and black arrows in (A) point to a thin wetting layer of ETPTA and the ITO electrode, respectively.

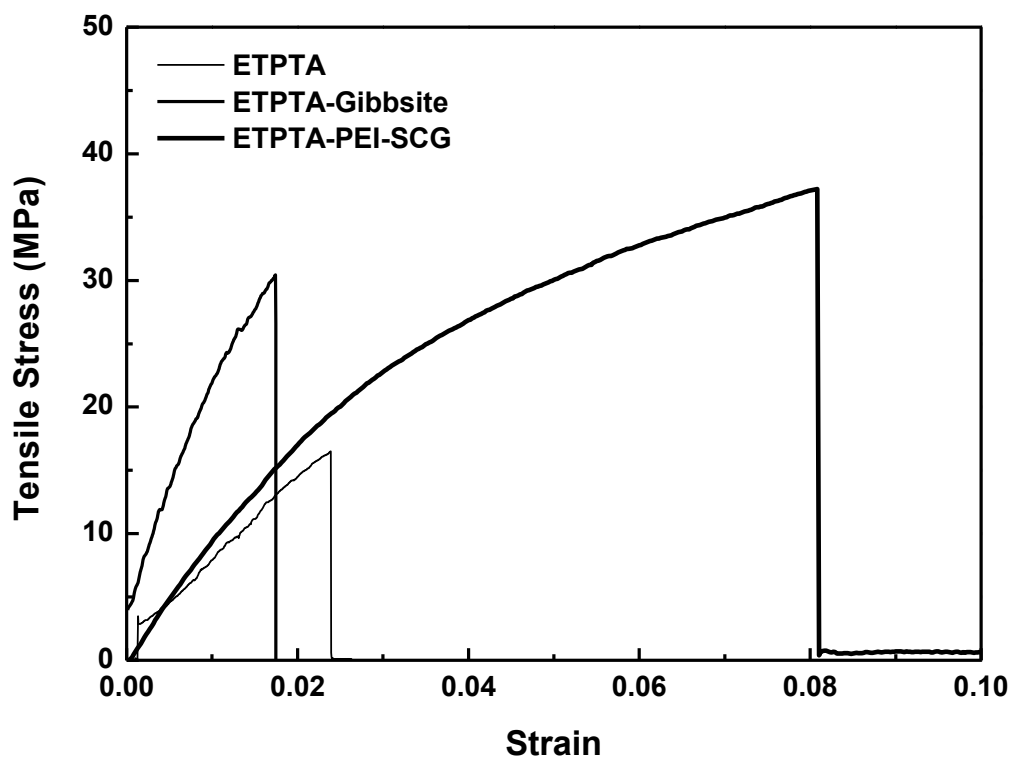


Figure 4-9. Tensile stress vs. strain curves for plain ETPTA film, ETPTA-Gibbsite nanocomposite, and ETPTA-PEI-SCG nanocomposite.

CHAPTER 5
ELECTROCHEMICAL SERS AT PERIODIC METALLIC NANOPYRAMID ARRAYS

Background

Surface Plasmon

Surface plasmons (SPs) are electromagnetic waves that propagate along a metal/dielectric interface (61). These are incident light waves that are trapped on the interface because of their interaction with free electrons in metal, leading to a strong concentration of electromagnetic energy at the interface. In this interaction, the free electrons oscillate in response to the incident light waves, as shown in Figure 5-1. The resonant interaction between the surface charge oscillation and the electromagnetic field of the light forms the SP and gives rise to its unique properties. Typical metals used to support surface plasmons are gold and silver (62, 63), but metals such as copper (64), titanium (65), or chromium (66, 67) can also sustain surface plasmon generation.

There are two consequences of the coupling to surface plasmons. One is that in contrast to the propagation of SPs along the interface, the field normal to the metal surface decays exponentially from the interface, resulting in non-radiative nature of SPs and preventing power from losing. The other is that the interaction between the free electron and the electromagnetic field results in the momentum of SP, $\hbar k_{sp}$, being greater than that of incident photons, $\hbar k_0$. This can be obtained by solving Maxwell's equations under appropriate boundary conditions and gives

$$k_{sp} = k_0 \sqrt{\frac{\epsilon_d \epsilon_m}{\epsilon_d + \epsilon_m}}$$

where ϵ_d and ϵ_m are the permittivity of the metal and the dielectric material, respectively. The difference in momentums of incident light and SPs must be compensated in order to generate SPs. Typically there are three ways to bridge the momentums. The first one requires the use of prism to enhance the momentum of the incident light. The second one exploits surface defects to scatter incident light. The third one is to generate periodically patterned nanostructures, such as sub-wavelength nanohole arrays.

Extraordinary Optical Transmission

One of the important applications of SP is the extraordinary optical transmission through sub-wavelength hole arrays (68-71), as shown in Figure 5-2. The desire to control photons in a manner analogous to the control of electrons has made SP significant. According to the standard aperture theory, the transmission of a sub-wavelength aperture is extremely low and proportional to the fourth power of the ratio of its diameter and light wavelength while apertures are smaller than the wavelength of the incident photon, resulting in a main constraint in manipulation of light (72). However, it has been found that arrays of films perforated with periodic sub-wavelength holes allow unusually high transmission of light at wavelengths larger than the array period due to surface plasmon resonance (SPR), showing extraordinary optical transmission. The transmission of light through sub-wavelength hole arrays made in a metal film can be orders of magnitude larger than expected from standard aperture theory. Experiments have provided evidence that these unusual optical properties are as a result of the coupling of light with SPs on the surface of the periodically patterned metal film.

Considerable interest in the optical properties of the periodic arrays of sub-wavelength apertures in metallic thin films has raised due to their potential numerous applications in photonic circuits, light manipulation, sub-wavelength photolithography

and optical modulators. In the past, absorption of SPs by metal was a significant problem that SPs were not considered for photonic elements because the SP propagation length was smaller than the size of components. It has been demonstrated that coherent spatial SP propagation lengths are a few μm and ultrafast decay of the SP polarization occurs on a 10 fs time scale (73). However, this view has been changed due to advances in nanotechnology. Recent SP-based components are significantly smaller than the propagation length. This opens up the way to integrate several SP-based devices into circuits before propagation losses. Typically focused ion beam (FIB) milling is used to fabricate sub-wavelength holes (74-76) but it is a time consuming, expensive and low throughput process and the size of substrate is limited.

Surface-enhanced Raman Scattering

Since SP waves travel on the boundary of the metal and the external medium, the adsorption of molecules to the metal surface greatly changes the oscillation and therefore can be also used as sensors. SPR technique is of great importance for monitoring binding events in biological systems. Typically, reflection geometry (Kretschmann configuration) is required to excite SP through prism coupling. SPR techniques provide good sensitivity at the submonolayer level. However, because the principle of operation establishes on the oscillation change of SP resonances, specificity at the molecular level is poor. SP-enhanced spectroscopic methods therefore become a powerful tool for chemical and biochemical analysis, providing better molecular specificity.

SERS is the most commonly used SP-mediated molecular spectroscopic method, as shown in Figure 5-3 (77). The enhanced Raman signal provides a molecular fingerprint due to its narrower bandwidth. SERS is a noninvasive technique that enables

the detection and characterization of both small organic and big biological molecules at very low concentrations, or even at the single-molecule level (78-81). This opens up exciting new opportunities for the sensitive and selective detection of analytes that are commonly encountered in the analysis of chemical warfare agents, biological products, food regulation, water quality control, and environmental monitoring. Electrochemical SERS is an important branch of SERS studies and has attracted great scientific and technological interest as it enables in situ investigation of adsorption and reaction at electrochemical interfaces, promising for developing fundamental understanding and control of fuel cells, metal corrosion, semiconductor processing, electrocatalysis processes, and electroanalysis (82-85). Electrochemically roughened metal surfaces have been extensively exploited as electrodes for electrochemical SERS (82, 86-89). However, the relatively low SERS enhancement (on the order of 10^4), the poor reproducibility of SERS enhancement (intensity variation by a factor of ~ 10 across a sample surface), and the electrochemical instability at high cathodic potentials are major drawbacks for these roughened electrodes. Therefore, how to generate reproducible SERS substrates that provide high enhancement factor is of great importance.

Substrates for Surface-enhanced Raman Scattering

Bottom-up colloidal self-assembly and templating nanofabrication provide an inexpensive and simple-to-implement alternative to the electrochemical roughening process in creating nanostructured SERS electrodes (90-97). Metal film over nanosphere (MFON) electrodes prepared by vapor deposition of a SERS-active metal (Au or Ag) over a self-assembled nanosphere monolayer have been demonstrated to exhibit improved stability and reproducibility for electrochemical SERS experiments

(98). Rapid detection of an Anthrax biomarker was achieved using SERS on silver film over nanosphere (AgFON) substrates (99). Atomic layer deposition (ALD) is used to deposit a sub-1-nm alumina layer on AgFON substrates to improve Anthrax biomarker detection (100). In comparison to the bare AgFON substrates, the ALD-modified AgFON substrates show higher sensitive and better stability. Sculpted electrochemical SERS-active electrodes with regular hexagonal arrays of sphere segment nanovoids, which show reproducible and high (1.5×10^5) surface enhancement, have been replicated from colloidal crystal templates via electrodeposition of coinage metals in particle interstitials (101). Unfortunately, most of the current bottom-up approaches suffer from low throughput and incompatibility with standard microfabrication, thereby impeding the cost efficiency and scale-up of these unconventional methodologies in generating SERS active electrodes.

Inspired by tip-enhanced Raman scattering (TERS) (92, 102-104), we have recently developed a simple yet scalable colloidal templating technique for producing wafer-scale gold nanopyramid arrays with nanoscale tips and high tip density (6×10^8 tips cm^{-2}) (105). These periodic arrays of nanopyramids can enhance the local electromagnetic field in the vicinity of the sharp nanotips, resulting in strong surface enhancement for Raman scattering from benzenethiol molecules absorbed on the gold surfaces. Here we demonstrate that these templated nanopyramid arrays can be utilized as electrodes for achieving high SERS enhancement. The resulting SERS intensity can be adjusted by tuning the applied electrode potential and the electrochemical reactions on the electrode.

Experimental

Preparation of Electrochemical SERS-active Gold Nanopyramid Arrays

The synthesis and purification of monodispersed silica microspheres with 320 nm diameter in 200-proof ethanol were performed according to a reference (106). Detailed procedures are as below:

1. Clean all glassware as the procedures in Chapter 2.
2. Put a stirring bar in a 1000 ml flask.
3. Enclose the flask with a septum and weight the flask
4. Enclose a bottle of EtOH with a septum.
5. Draw EtOH from the bottle with a 60 ml syringe.
6. Put a 0.2 μm PTFE hydrophobic filter on the syringe and inject EtOH into the flask.
7. Repeat 4~5 until EtOH reaches 665 ml (525g, density = 0.789).
8. Take off the filter and draw sufficient amount of DIW.
9. Put a 0.2 μm hydrophilic filter on the syringe and inject 55.7g of DIW into the flask.
10. Take off the hydrophilic filter and draw sufficient amount of ammonia hydroxide.
11. Put the hydrophilic filter on and inject 25.7ml (23.1g, density = 0.8988) of ammonia hydroxide.
12. Strongly stir on hot plate and then inject 50 ml of DISTILLATED TEOS as quickly as possible and vigorously shake the flask.
13. Aging for 8 hours on a stirring plate at a stirring rate around 7~8.

The purified silica colloids were concentrated by centrifugation and redispersed in ETPTA using a vortex mixer (Fisher). To this 1 wt.% Darocur 1173 was added as photoinitiator. The final particle volume fraction was adjusted to ~20%. The colloidal suspension was dispensed on a silicon wafer (testgrade, n type, (100), Wafernet) which had been primed by 3-acryloxypropyl trichlorosilane (Gelest). The established spin-

coating process was then utilized to generate monolayer colloidal crystal embedded in ETPTA monomer using a standard spin coater (WS-400B-6NPP-Lite Spin Processor, Laurell). The ETPTA monomer was photopolymerized for 4 s using a pulsed UV curing system (RC 742, Xenon). The polymerized ETPTA matrix was then removed by oxygen plasma etching operated at 40 mTorr pressure, 40 sccm flow rate, and 100 W for 2 min on a Unaxis Shuttlelock RIE/ICP reactive-ion etcher. The released silica particles were utilized as shadow masks during electron-beam deposition of 30 nm thick chromium using a Denton DV-502A EB evaporator with a typical deposition rate of 2 Å/s. The templating silica particles could then be removed by rubbing the wafer with a cleanroom Q-tip under flowing deionized water, resulting in the formation of chromium nanohole arrays on the (100) silicon wafer. The wafer was wet etched at 60°C for 4 min in a freshly prepared solution containing 62.5 g of KOH, 50 ml of anhydrous 2-propanol, and 200 ml of ultrapure water to create inverted pyramids in silicon. After dissolving the chromium layer in CR-7 etchant (Transene), 500 nm thick of gold was deposited on the silicon template at a deposition rate of ~5 Å/s with a Kurt J. Lesker CMS-18 Multitarget Sputter. The gold layer could finally be peeled off from the wafer surface with a conductive double-sided carbon disk (SPI Supplies), yielding an electrochemical SERS-active nanopyramid array in gold. The templated gold nanopyramid arrays were examined using a SEM prior to and after the electrochemical SERS experiments.

Electrochemical Surface-enhanced Raman Scattering

The electrochemical setup used to conduct the electrochemical SERS experiments was constructed as shown in Figure 5-4. A glass slide (Corning, 2.5 × 4.0 cm) was used as the substrate. On top of the slide were a conducting copper tape (3M, 1.2 × 4.0 cm) and then the conductive carbon disk (diameter of 1.2 cm) with the

templated gold nanopyramid array on its top side. Insulating tape obtained from Furan Co. was used to cover the rest of the copper tape. Platinum wire purchased from Sigma-Aldrich was used as the counter electrode. An aqueous solution consisting of 0.1 M NaCl and 0.05 M pyridine was used as the electrolyte. A flat gold film deposited by the same sputtering process as described above was used as the control sample for SERS measurements. The voltage (Au vs. Pt electrodes) was controlled by an EG&G Model 273A potentiostat (Princeton Applied Research). All Raman spectra were recorded on a Renishaw Raman microscope using a 785 nm diode laser at 48 μ W with an integration time of 10 s.

Cyclic Voltammetry Measurements

Two-electrode cyclic voltammetry was used to characterize electrodes in 0.1 M NaCl solution with or without 0.05 M pyridine, including electrodes that had only conductive carbon or copper tape on the glass slide and electrodes that had a gold nanopyramid array on carbon tape with or without copper tape between the carbon tape and the glass slide substrate. The active area of each electrode was controlled at 1 cm². Platinum wire was used as both counter and reference electrodes. The voltage was scanned between -1.0 and 1.0 V with a scan rate of 50 mV/s by using the EG&G potentiostat.

Electromagnetic Modeling of Raman Enhancement

In the finite-element-method (FEM) model, the gold nanopyramid array was supposed to be placed horizontally so that the interface between the substrate and the medium (water) was parallel to the xz-plane while the nanopyramids were along the y-axis. FEM was employed under a COMSOL Multiphysics environment to obtain numerical solutions of Maxwell's equations for each substrate (water and gold). In order

to obtain high-resolution numerical solutions, the computational domain needs to be bounded and the boundary conditions should be well-defined. To this end, the “perfect matched layers” (PML) boundary approach was utilized for the simulation (47).

Artificially constructed 10 boundary layers were around the medium (water) and the scatter (gold) domains. The electric and magnetic conductivities of each boundary layer could be set artificially so that little or no electromagnetic radiation would be reflected back into the domain of scatter. TO simulate electromagnetic fields in the newly augmented domain, Maxwell’s equations in all subdomains were solved. For the outer boundaries of the PML layers, a low-reflection boundary condition (47) was provided to minimize residual reflection and attenuate the wave quickly within the layers. After solving Maxwell’s equations together with the above boundary conditions, the two-dimensional electric field could be used to calculate the Raman enhancement factor as

$$G(x, y) = \log\left(\left|\frac{E(x, y)}{E_0}\right|^4\right)$$

where $E(x, y)$ was the electric field amplitude at location (x, y) and E_0 was the incident electric field amplitude (107). The maximum value of the Raman enhancement could be obtained over the medium (water) domain.

Results and Discussion

Colloidal Templating Process for Nanopyramid Array Fabrication

The schematic illustration of the colloidal templating process for fabricating gold nanopyramid array electrodes is shown in Figure 5-5. The established spin-coating technique is first applied to shear-align submicrometer-sized silica particles into ordered colloidal monolayers. In contrast with previous colloidal self-assembly approaches, spin-coating enables rapid production of colloidal crystal templates with wafer-scale area (up

to 8 in. diameter). Though the particles are not touching each other, they do exhibit long-range hexagonal ordering. After removing the polymer matrix surrounding silica particles by brief oxygen plasma etch process, the nontouching silica particles can be used as shadow masks during physical vapor deposition of chromium to create periodic nanohole arrays, which are then utilized as etching masks to make inverted silicon pyramidal pits by anisotropic KOH wet etch. Wafer-scale gold nanopyramid arrays with sharp tips can finally be replicated by sputtering a thin layer of gold on the silicon templates, followed by a simple adhesive peeling process. By simply controlling the size of the templating silica spheres and the anisotropic wet etch conditions (e.g., temperature, duration, and etchant concentration), the dimensions of the templated nanopyramids, such as base length, depth, and separation, can be adjusted. Figure 5-6A shows a tilted SEM image of an array of gold nanopyramids templated from 320 nm silica spheres. The long-range hexagonal ordering of nanopyramids is clearly evident from the image. Magnified SEM images show that most of the pyramidal tips have a radius of curvature of $r < 10$ nm.

Electrochemical SERS Spectra of Pyridine on Gold Nanopyramid Arrays

The electrochemical SERS measurements are carried out using a 0.05 M pyridine aqueous solution with 0.1 M NaCl as a background electrolyte. Figure 5-7 shows a comparison of SER spectra obtained at -1.0 V on the gold nanopyramid array electrode and a flat gold control electrode prepared by the same sputtering process. The nanopyramid electrode exhibits a strong Raman scattering signal, while the featureless gold control sample does not show distinctive SERS peaks at the same experimental conditions. The control sample has been prepared in the same sputtering batch as the

nanopyramid electrode and therefore has a similar surface roughness. The peak positions and the relative amplitude of the peaks obtained at the nanopyramid electrodes agree well with those in the literature for pyridine adsorbed on roughened gold disk electrodes (108, 109), but are significantly different from those obtained at sculpted gold nanovoid array electrodes (101). The assignment of the spectral peaks is shown in Table 5-1 (110). From Table 5-1, it is clear that almost all the enhanced vibrational modes are associated with the in-plane perturbations, indicating that the adsorbed pyridine molecules are bonded perpendicular to the metal surface via their nitrogen lone pairs (97, 98, 108). Another evidence of the end-on configuration of the adsorbed molecules comes from the two peaks at 1013 and 1037 cm^{-1} , which correspond to the ring breathing mode and the ring mode (ν_{12}) and occur at frequencies close to those obtained for pyridine in solution (87, 108). By contrast, for flat-adsorbed pyridine molecules, the frequencies of the ring modes are expected to decrease when compared to those of the “free” molecules in the liquid state, due to the interaction of the π -electrons of the ring with the electrode surface (111).

Figure 5-8 shows the SER spectra recorded for adsorbed pyridine as a function of electrode potential applied on the gold nanopyramid array electrode (vs. a platinum counter electrode). It is clearly evident that stronger SERS enhancement occurs at higher negative potentials when the potential is swept from +1.0 to -1.0 V. Similar SERS intensity dependence on the applied electrode potential has previously been reported on Au(210) single-crystal electrodes (108) and AgFON electrodes (98). The maximum surface enhancement factor at -1.0 V is estimated to be $\sim 2.7 \times 10^6$ using the method described in the literature by comparing the Raman intensity for the peak at

1013 cm^{-1} obtained for a solution and at the nanopyramid electrode and assuming a surface coverage of 0.40 nmol cm^{-2} for pyridine on gold and a surface roughness of 3.0 (84). This enhancement is more than 1 order of magnitude higher than that obtained at other nanostructured electrodes (98, 101). Figure 5-9 shows the SER spectra of pyridine adsorbed on a gold nanopyramid electrode when the potential is swept from -1.0 V (top spectrum) to $+1.0$ V (middle spectrum) and then back to -1.0 V (bottom spectrum). The peak amplitude is greatly reduced when the potential is swept from -1.0 to $+1.0$ V and the 1013 cm^{-1} peak is shifted to 1018 cm^{-1} . When the potential is cycled from $+1.0$ V back to -1.0 V, the SERS signal is even stronger than the original spectrum obtained at -1.0 V and the peak at 1013 cm^{-1} reaches the detection limit of the Raman spectrometer. Further potential cycling experiments show that the high SERS enhancement at -1.0 V can be consistently achieved for at least five cycles and then starts to decrease for more sweeps.

Electrode Effects

The experimental results shown in Figures 5-8 and 5-9 are contradictory to those obtained at sculpted nanovoid arrays, where higher SERS intensity is observed at more positive potentials (101). To help understand this contradiction, we conducted two-electrode cyclic voltammetry measurements to evaluate potential redox reactions on nanopyramid electrodes in 0.1 M NaCl solution with or without 0.05 M pyridine. As shown by the dashed curve in Figure 5-10, the nanopyramid electrode that consists of a gold nanopyramid array on an adhesive carbon disk and a conductive copper tape exhibits apparent redox activities when the electrode potential is cycled between -1.0 and $+1.0$ V. This is caused by the electrochemical reactions on the conductive copper

tape which is used as a conducting wire to connect the gold nanopyramid array to the potentiostat and is partially exposed to the electrolyte solution. A similar cyclic voltammogram is obtained when pure copper tape is used as the electrode as shown by the thin solid curve in Figure 5-10. Since the applied cyclic electrode potentials are below the electrolytic potential of water (≥ 1.23 V) (112), we believe that the anodic reaction on the conductive copper tape is $\text{Cu} \rightarrow \text{Cu}^{2+} + 2\text{e}^-$. By contrast, when pure conducting carbon tape (thick solid curve) and gold pyramid array on carbon tape (dotted curve) are used as electrodes, no apparent redox reactions are observed. Similar cyclic voltammetry results are obtained when the electrolyte solution contains 0.1 M NaCl and 0.05 M pyridine.

We speculate that the electrochemical reactions on the conductive copper tape are responsible for the observed SERS intensity-electrode potential contradiction between the templated nanopyramid array and sculpted nanovoid array electrodes. It is well-known that pyridine can easily conjugate with Cu^{2+} ions to form a positively charged complex, $[\text{Cu}(\text{py})_4]^{2+}$ (107), which can be electrophoretically attracted by the cathode, while being repelled from the anode. This could lead to a higher concentration of pyridine on the cathode surface and therefore results in higher SERS intensity at more negative potentials. To verify this speculation, we conducted the same electrochemical SERS experiments with a gold nanopyramid array supported only by an electrochemically inert conductive carbon tape (see the cyclic voltammetry results in Figure 5-10). The experimental results as shown in Figure 5-11 exhibit the same SERS intensity–electrode potential relationship as observed on sculpted nanovoid array electrodes (i.e., higher SERS intensity occurs at more positive potentials). The relatively

low SERS enhancement could be due to the reduced sharpness of the nanotips of the nanopyramid array which was templated from an inverted silicon mold that had been used multiple times.

Electromagnetic Modeling

We believe the electromagnetic enhancement caused by the significant concentration of the electromagnetic field in the vicinity of the sharp nanotips is the dominating mechanism for the observed SERS enhancement at nanopyramid electrodes. To verify this hypothesis, we conduct finite element electromagnetic modeling using COMSOL Multiphysics software to calculate the electric field amplitude distribution and the corresponding Raman enhancement factors surrounding arrays of nanopyramids (113). Since the periodic nanostructure is symmetric, it is reasonable to construct a simplified two-dimensional (2-D) model which can be considered as sections through a three-dimensional nanopyramid array at the point of maximum enhancement (Figure 5-12). To numerically solve the 2-D Maxwell's equations, the "perfect matched layers" (PML) boundaries method is utilized for the simulation (114). The widely used optical constants for gold (115) are employed to conduct the electromagnetic modeling, and the surrounding medium is water.

Figure 5-12A shows the simulated distribution of the SERS enhancement factor around two adjacent nanopyramids with base length of 320 nm, interpyramid distance of 1.414×320 nm (106), and nanotip radius of curvature of 5 nm. The height of nanopyramids is determined by the base length as wet-etched silicon pyramids have characteristic 54.7° side walls (116). The simulation results show that the significant enhancement of the electromagnetic field and the maximum SERS enhancement ($10^{4.7}$) happen at the vertices of the nanotips, and are favorably comparable to other numerical

simulations for nanotips and nanorings (92, 117, 118). The spatial distribution of the electromagnetic “hot spots” of the two triangles is asymmetric. This is caused by the electromagnetic interaction between neighboring nanotips. Figure 5-12B shows that larger arrays with more nanotips but the same structural parameters result in higher enhancement and the maximal enhancement factor reaches a plateau ($G_{\max} \sim 10^{7.5}$) when the array has more than 12 tips. This indicates that the electromagnetic coupling between adjacent scatters played a critical role in determining the electric field amplitude distribution and the corresponding Raman enhancement factors surrounding arrays of nanopyramids. Indeed, the calculated G_{\max} at the nanotip apex could be even higher if the sharp edges and facets of the nanopyramids are considered in a more realistic three-dimensional (3-D) model instead of the current 2-D model. The very small effective area occupied by the sharp nanotips (electromagnetic hot spots) could be the reason for the significant difference between the simulated G_{\max} and the experimental enhancement factor. A recent experimental study shows that a very small percentage of molecules (0.0063%) in the hottest spots contribute 24% to the overall SERS intensity (119). We believe that the surface roughness of the templated nanopyramid electrodes plays only a minor role in the observed SERS enhancement. Indeed, the SEM image in Figure 5-6B shows that the surface roughness of the nanopyramid electrode does not change much after the electrochemical SERS experiment.

Summary

In summary, we have developed a bottom-up approach for fabricating periodic arrays of gold nanopyramids with nanoscale sharp tips. These nanotips can significantly enhance the local electromagnetic field at the tip apex, resulting in more than 1 order of magnitude higher SERS enhancement than other nanostructured electrodes. We have

also found that the redox reactions occurring near the nanopyramid electrode play a crucial role in determining the dependence of SERS enhancement on the applied electrode potential. The current templating technology is scalable and compatible with standard microfabrication, enabling large-scale production of SERS-active electrodes for in situ electrochemical studies and sensitive electroanalysis.

Table 5-1. Assignment of SERS peaks for pyridine adsorbed on gold nanopyramid electrode

Label	SERS peak (cm ⁻¹)	Vibration mode	Vibration type
a	634	V_{6a}	Symmetric
b	650	V_{6b}	Asymmetric
c	699		
d	1013	V_1	Ring breathing
e	1037	V_{12}	C-H in-plane deformation
f	1068	V_{18a}	C-H in-plane deformation
g	1216	V_{9a}	C-H in-plane deformation
h	1600	V_8	Ring stretching

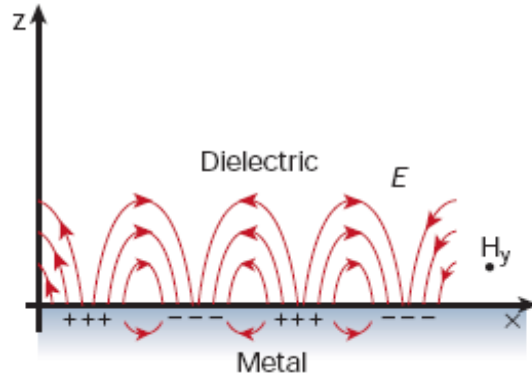


Figure 5-1. Surface plasmons propagate along a metal/dielectric interface (61).

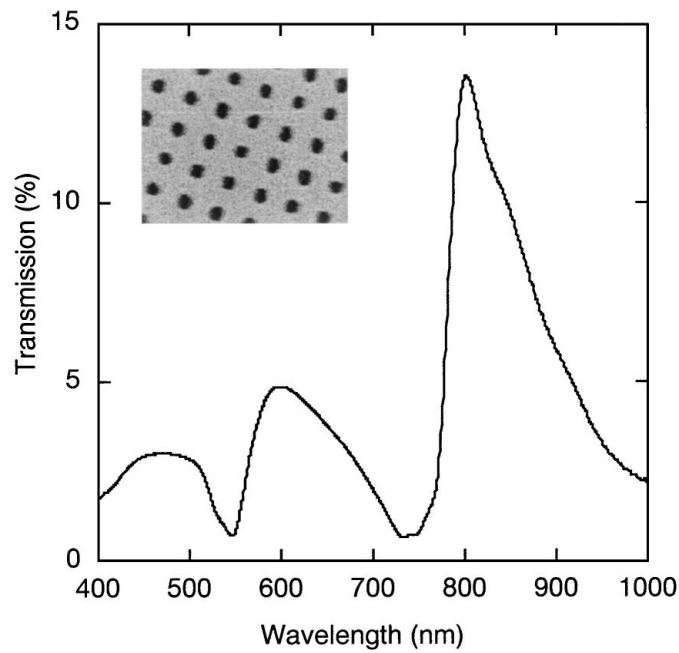


Figure 5-2. Extraordinary transmittance at normal incidence for a square array of holes. The area covered by holes is only 11% while the normalized-to-area transmittance of lights is 130% (69).

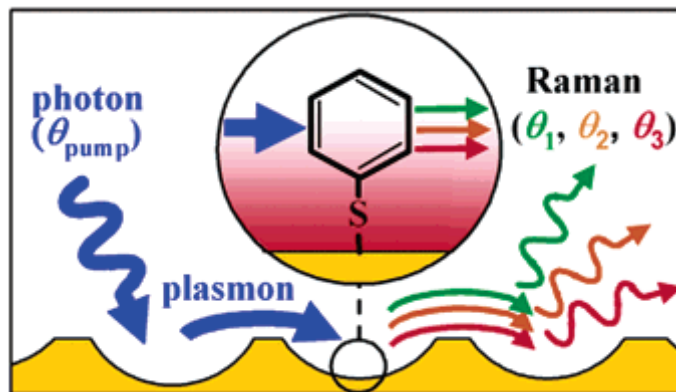


Figure 5-3. Schematic SERS process in which light is Raman scattered by a molecule on the surface (77).

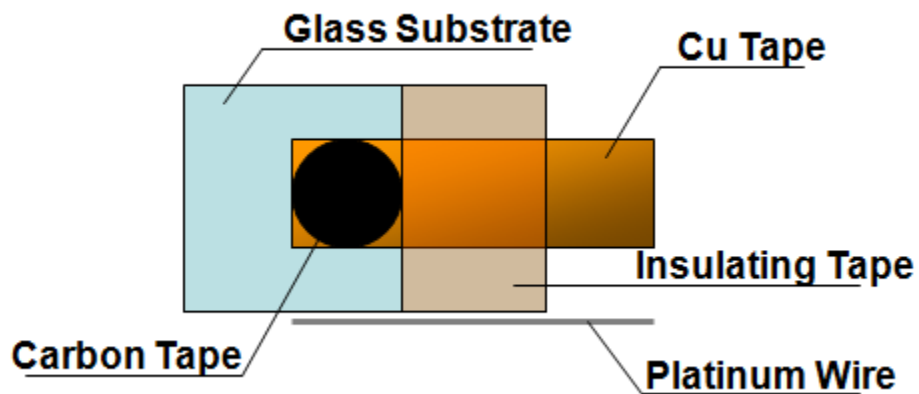


Figure 5-4. Schematic illustration of electrochemical SERS set up.

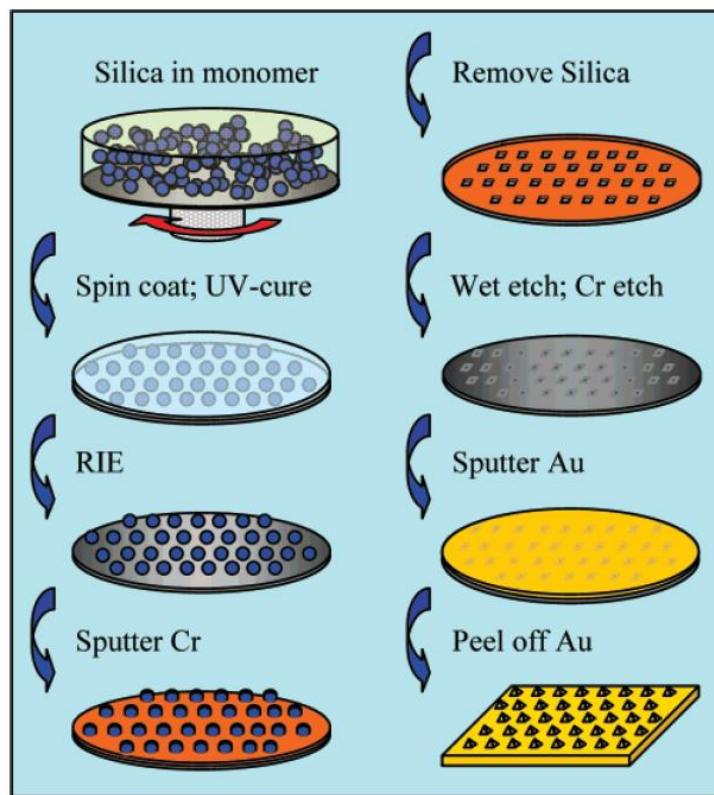


Figure 5-5. Schematic illustration of the templating procedures for fabricating gold nanopyramid array by using spin-coated monolayer colloidal crystal as template (105).

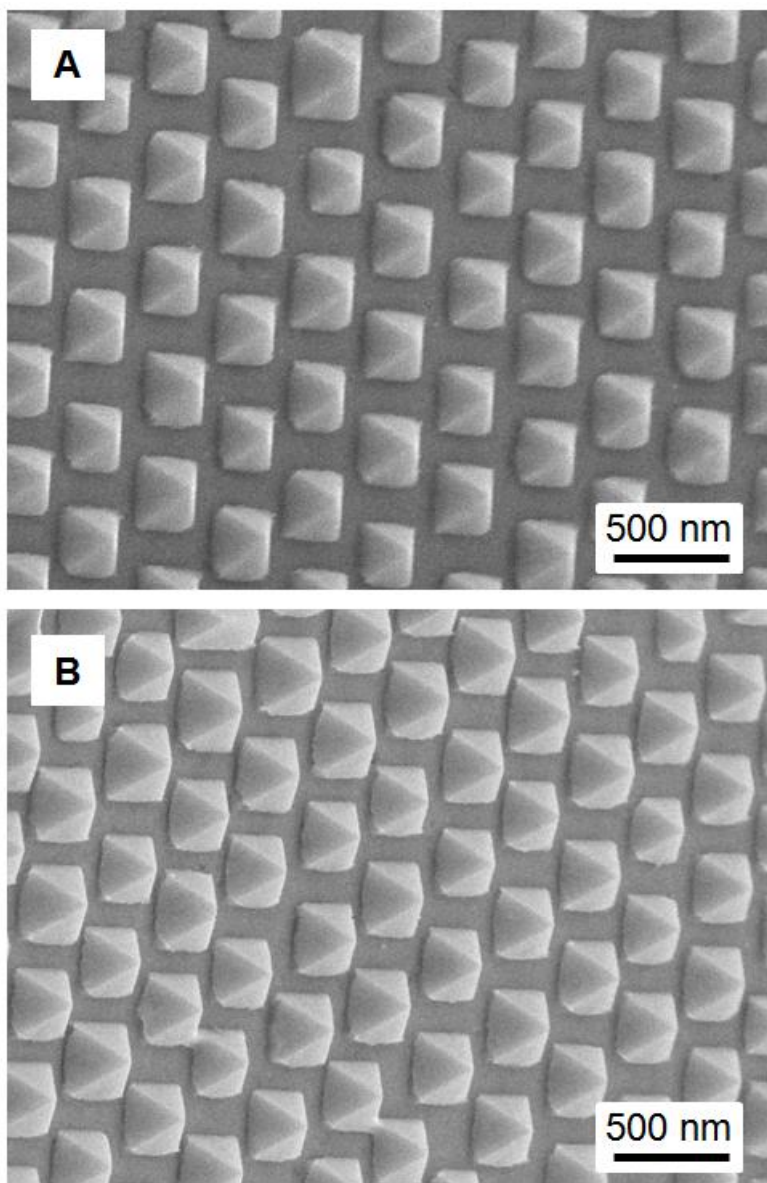


Figure 5-6. Tilted (35°) SEM images of a gold nanopillar array electrode prior to (A) and after (B) electrochemical SERS experiments. As templates, 320 nm silica spheres were used.

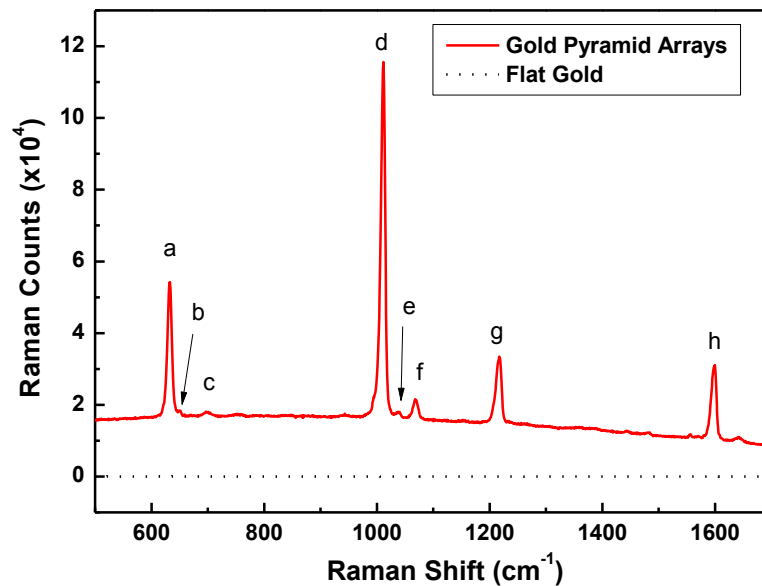


Figure 5-7. Electrochemical SER spectra recorded on a gold nanopyramid array supported by a conductive carbon disk and a copper tape (red) and a flat gold control sample on silicon (black) in 0.1 M NaCl solution containing 0.05 M pyridine.

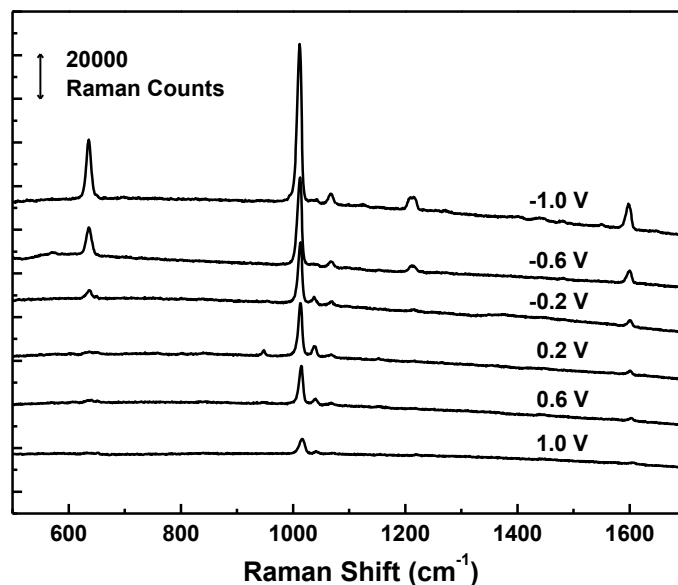


Figure 5-8. Electrochemical SER spectra recorded on a gold nanopyramid array supported by a conductive carbon disk and a copper tape in 0.1 M NaCl solution containing 0.05 M pyridine.

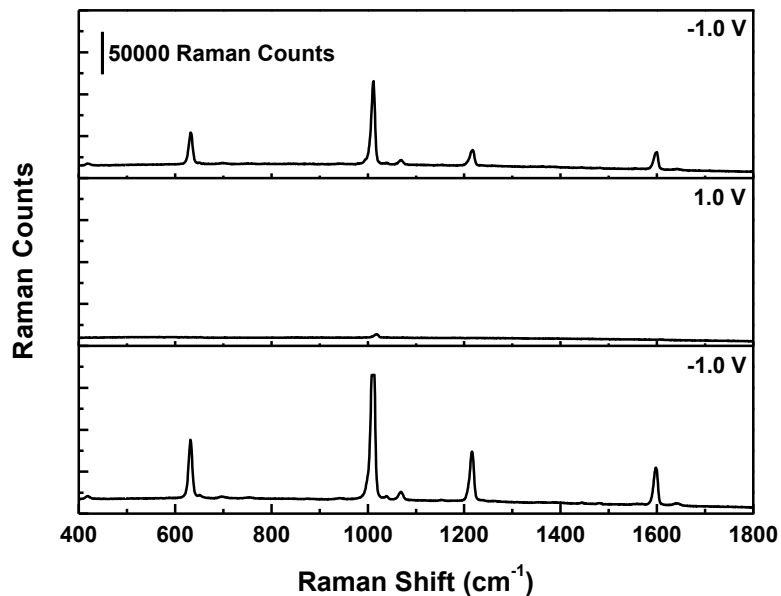


Figure 5-9. The gold electrode potential was swept from -1.0 V (top) to $+1.0$ V (middle) and then back to -1.0 V (bottom).

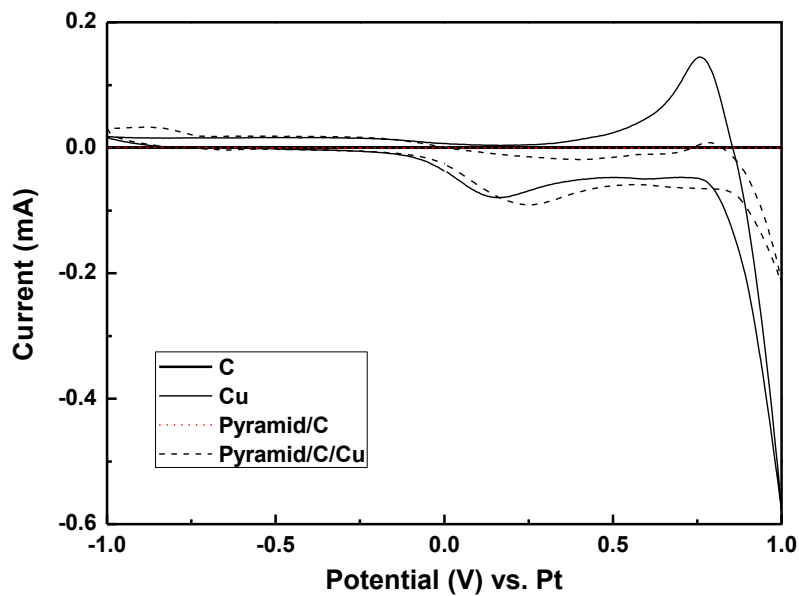


Figure 5-10. Cyclic voltammograms of a conductive carbon tape, a conductive copper tape, a gold nanopillar array supported by a carbon tape, and a gold nanopillar array supported by a carbon disk and a copper tape in 0.1 M NaCl.

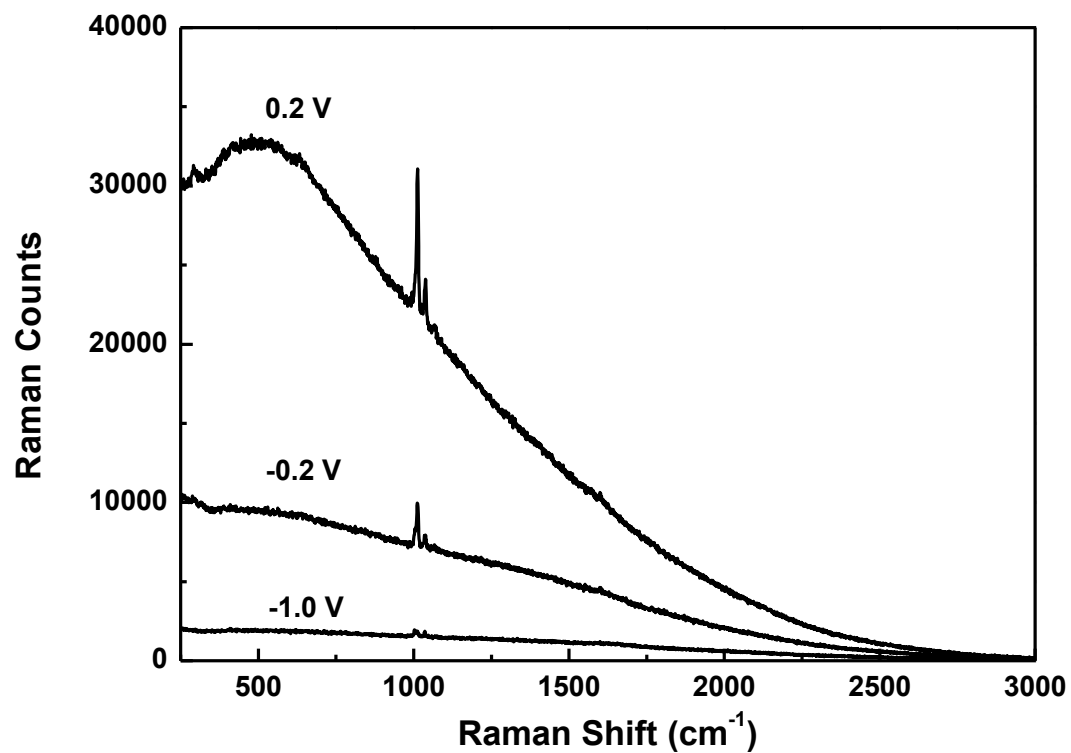


Figure 5-11. Electrochemical SER spectra obtained on a gold nanopyramid array supported by a conductive carbon tape in 0.1 M NaCl solution containing 0.05 M pyridine. The gold electrode potential was swept from -1.0 to 0.2 V. The spectra were taken using a 785 nm diode laser at $48 \mu\text{W}$ with an integration time of 10 s.

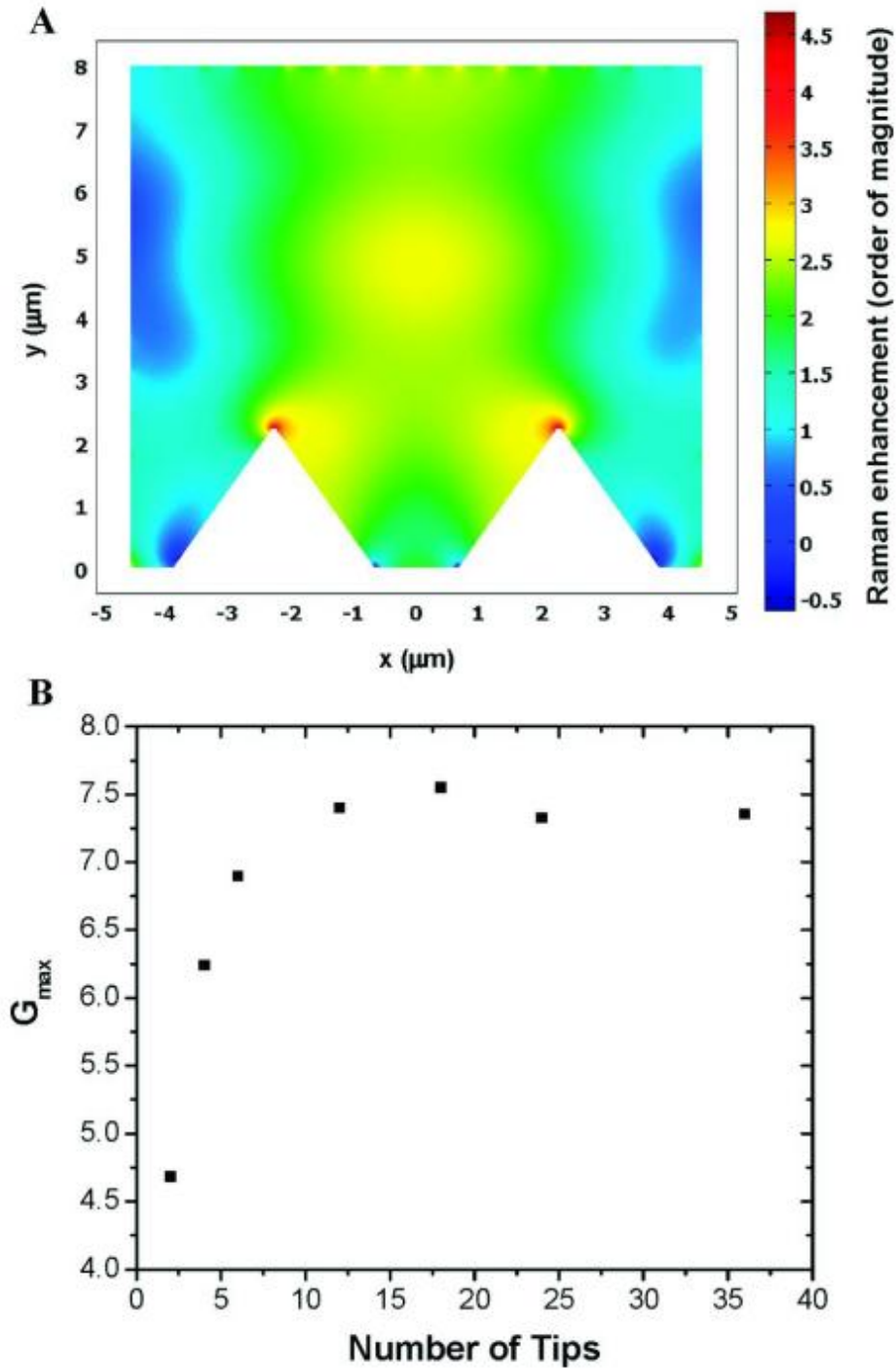


Figure 5-12. (A) Modeled Raman enhancement factor around two gold nanopillars with base length of 320 nm and nanotips radius of curvature of 5 nm at $\lambda = 785$ nm. (B) Simulated maximum SERS enhancement factor (G_{max}) vs. number of tips of the templated nanopillar array with the same structural parameters as (A).

CHAPTER 6 GRAPHENE PAPER ACTUATORS

Background

Graphene, a two-dimensional honeycomb building block for graphitic materials of other dimensionalities (120, 121), has been extensively studied due to its extraordinary qualities in electrical, thermal, and mechanical aspects that provide itself opportunities in fields such as electronics (122, 123), composites (124-126), sensors (127, 128) and capacitors (129). It can be wrapped up into 0D fullerenes, rolled into 1D nanotubes or stacked into 3D graphite, as shown in Figure 6-1 (121). Besides these fields, graphene is also a strong candidate in making actuators that can convert electrical energy into mechanical energy because of its high surface area for double-layer charging and the above excellent properties. The direct conversion of energy through materials is of great importance for applications in robotics, prosthetic devices, optical displays as well as micro pumps (130). As an actuator material, graphene has the following advantages: it is electrically conductive with high electron mobility of $15,000 \text{ cm}^2\text{V}^{-1}\text{s}^{-1}$; it has high intrinsic stress of 130 GPa and it is light-weight (121, 131). All the extraordinary properties mentioned above make graphene attractive for use in making actuators.

Electromechanical actuators based on sheets of single-walled carbon nanotubes were reported (132), showing stresses higher than natural muscle and strains higher than ferroelectric materials. The quantum chemical-based expansion without ion intercalation is believed as the mechanism that causes actuation. Actuation of graphite oxide (GO)/graphene bilayer papers were also reported (133). Instead of driving by an applied voltage as the carbon nanotube actuator, the bilayer actuator was driven by variation of humidity and temperature and therefore has poor controllability. Here we

report electromechanical actuators based on two strips of graphene papers with an intermediate dielectric layer. Graphene papers were produced by flow-directed assembly (134) of one-atom-thick graphene sheets, which were obtained from chemically reduced GO sheets. GO sheets were generated by exfoliation of highly oxygenated graphite in water. The actuators were operated under repeated potential steps and cyclic voltammetry. Cycling stability of the graphene-based actuators was also explored.

Experimental

Materials and Methods

Graphene papers

Graphene papers were basically made by following a procedure presented by Li and colleagues (135, 136). Schematic illustrations of graphene paper preparation are shown in Figure 6-2, 6-3, and 6-4. Simply put, graphite oxide was first synthesized from natural graphite by a modified Hummers method that consists of an additional oxidation prior to the typical Hummers method (137, 138). As-synthesized graphite oxide was subjected to multiple cycles of centrifugation and re-dispersion until no supernatant formed after centrifugation and then suspended in ultrapure water (18.2 M Ω cm⁻¹, Barnstead water system) to give a viscous, inhomogeneous, brown suspension with a concentration of 0.6 wt.% and then stored. To prepare colloidal dispersion of GO, the stored graphite oxide suspension was diluted with ultrapure water to 0.05 wt.%, followed by exfoliation carried out with ultrasonication for 60 min. The dispersion was then subjected to centrifugation at 3,000 r.p.m. for 30 min to remove unexfoliated graphite oxide and subsequent dialysis for several hours to remove residual salts and acids, resulting in a clear, homogeneous and brownish dispersion as shown in Figure 6-5A.

Chemical reduction (136) of GO to graphene was conducted by mixing 3 ml of GO dispersion with 3 ml of ultrapure water, 21 μl of ammonia solution (14.8 N, Fisher Chemical) and 3 μl of hydrazine (35 wt.% solution in water, Sigma Aldrich) in a glass vial with a hot water bath for 1 h to give a homogeneous and black dispersion as shown in Figure 6-5B. The graphene paper was then made by vacuum filtration of the graphene dispersion through an Anodisc membrane (25 mm in diameter, 0.02 μm pore size, Whatman) (134). The resulting deposit was then air dried and peeled from the membrane to give a free-standing graphene paper. The graphene paper was cut into 2 mm by 15 mm strips by a razor blade for mechanical testing and making actuators.

Detailed procedures for making graphene dispersions are listed as below:

Prior to Hummers' method (additional oxidation, as in Figure 6-2)

1. Grind graphite flakes into powder.
2. Put graphite powder (1g) into an 80°C solution of concentrated H_2SO_4 (1.5 ml), $\text{K}_2\text{S}_2\text{O}_8$ (0.5 g) and P_2O_5 (0.5 g). Use a 250 ml flask. No stirring bar required.
3. Thermally isolate and allow the dark blue mixture to cool to room temperature over a period of 6 h.
4. Carefully dilute the mixture with DIW.
5. Filter and wash the mixture with vacuum filtration until the rinse water pH becomes neutral.
6. Dry the product in air at ambient temperature overnight.

Hummers' method (as in Figure 6-3)

7. Put this pre-oxidized graphite into concentrated H_2SO_4 (23 ml) that have been cooled to 0°C in an ice-bath with vigorous stirring.
8. Gradually add KMnO_4 (3 g) so that the temperature of the mixture is not allowed to reach 20°C.
9. Remove the ice-bath, bring the temperature to 35°C and stir for 2 h. (As the reaction progressed, the mixture gradually thickened with a diminishing in effervescence. The mixture was brownish grey in color at the end of the reaction.)

10. Slowly stir DIW (46 ml) into the paste. (Violent effervescence occurs and temperature increases to 98°C.)
11. Keep the diluted brown suspension at this temperature for 15 minutes.
12. Further dilute the suspension with WARM DIW (140 ml).
13. Slowly treat the suspension with 30% H₂O₂ (2.5 ml) to reduce the residual permanganate and manganese dioxide to colorless soluble manganese sulfate. Upon treatment with the peroxide, the suspension turned bright yellow.
14. Filter and wash the suspension with WARM 1:10 HCl solution (250 ml) to remove metal ions, resulting in a yellowish-brown filter cake. (The filtering has to be conducted while the suspension was still warm to avoid precipitation of slightly soluble salt of mellitic acid formed as a side reaction.)
15. Wash the filter cake with DIW by multiple centrifugation/re-dispersion steps until no supernatant forms after centrifugation.
16. Suspend the GO product in DIW to give a viscous, brown dispersion, which is stable for a period of years.

Exfoliation and reduction of GO (as in Figure 6-4)

17. Exfoliation can be achieved by dilution of the GO dispersion with DIW, followed by sonication and dialysis.
18. Prepare GO dispersion (0.05 wt. %) by sonication and use dialysis to completely remove metal ions and acids. (For 30 ml 0.05 wt. % dispersion, take 2.5 ml of 6 mg/ml solution and then dilute to 30 ml.)
19. Mix the above dispersion (3 ml), DIW (3 ml) and 28 wt. % NH₄OH (21 μl) into a 20 ml glass vial.
20. Add 35 wt.% hydrazine (3 μl) into the vial and shake vigorously.
21. Put the vial in a 95°C water bath for 1h.

Graphene actuators

Graphene actuators were made in a relatively simple way as presented by Baughman and colleagues (132). Schematic illustrations of an actuator and apparatus used are shown in Figure 6-11. The actuator was made by laminating two strips of graphene papers with an intermediate larger of strip of Scotch Double Stick Tape (1 mm

wider and longer than graphene strips), resulting in a sandwich structure as shown in Figure 6-11A and B. Two pieces of Au/Cr/glass electrodes, made by sputter deposition of 20 nm of Cr and 200 nm of Au, were then attached on opposite sides of the upper end of the actuator with a clamp, facing to the graphene strips with the Au surface but not touching each other. A voltage could therefore be applied across the two Au electrodes without breaking the graphene strips. Actuation was carried out by immersing 10 mm of the actuator in 1 M NaCl solution held in a homemade rectangular glass tank as shown in Figure 6-11C. A graph paper was attached to one side of the glass tank as background for displacement measurement, which was done with the aid of videotaping the motion of the actuator under applied voltages. Displacements of the actuator tip were then calculated via the graph paper.

Results and Discussion

GO and Graphene Dispersions

Colloidal dispersions of GO were prepared by exfoliation of graphite oxide synthesized by a modified Hummers method, resulting in a homogeneous and brownish dispersion as shown in Figure 6-5A. Zeta-potential of the GO sheets in deionized water was measured to be -42.27 ± 1.33 mV by fitting experimental data using Smoluchowski's model. The sign and magnitude reveal that the GO sheets are highly negatively charged and electrostatically stabilized, resulting from phenolic hydroxyl and carboxylic acid groups formed during oxidation of graphite powders. Chemical reduction of GO to graphene was carried out by following a procedure presented by Li and co-workers. In this procedure, GO dispersions are adjusted to a low concentration of 0.025 wt.%. Ammonia is then added to GO dispersions in order to maximize the surface charge of GO sheets and therefore further stabilize the dispersions. After that, chemical reduction

is carried out by adding a small amount of hydrazine, resulting in a homogeneous and black dispersion. A graphene dispersion made by this method is shown in Figure 6-5B. Zeta-potential of this dispersion was measured to be around -2 mV. The low magnitude shows that graphene sheets in the dispersion are weakly charged as a result of unreduced carboxylic acid groups.

A TEM image of graphene sheets made by the above method is shown in Figure 6-6 in which graphene sheets are observed to be rested on TEM grids, folded and wrinkled. An AFM image of graphene sheets and height profiles are shown in Figure 6-7A and B, respectively. The height profile in Figure 6-7B1 shows that size of graphene sheets can be as large as 600 nm with a thickness of 0.6 nm, resulting in an aspect ratio of 1000. This high aspect ratio is beneficial in making organic-inorganic biomimetic nanocomposites. The height profile in Figure 6-7B2 consists of one and two layers of graphene sheets.

Graphene Papers

Because of the low zeta-potential, dispersions of graphene prepared by this procedure showed visible agglomeration after 2 days. Therefore, vacuum filtration through an Anodisc membrane of graphene dispersions was conducted immediately after chemical reduction to avoid severe aggregation which hinders mechanical properties of graphene papers. Top and bottom side images of a free-standing graphene paper made by vacuum filtration are shown in Figure 6-8A and B, respectively. The graphene paper was air dried and peeled directly from the membrane. As discovered by Li and co-workers, the graphene paper exhibits a metallic texture that demonstrates its smoothness.

The top-view and bottom-view SEM images in Figure 6-9A and B demonstrate that both surfaces are relatively smooth and graphene sheets are aligned parallel to the Anodisc membrane. The cross-sectional SEM image in Figure 6-9C provide further evidence that the graphene sheets are aligned and stacked parallel to each other to form a layered structure. It has been proposed that the layered structure is formed because rising in sheets concentration during filtration causes increasing in sheet-to-sheet interactions that make the sheets tend to align parallel to each other to reduce total energy of the system. Unlike graphene papers, GO papers made by the vacuum filtration method keeps a layered structure but do not exhibit smooth surfaces, as shown in Figure 6-10 and 6-11. Instead, SEM images of GO papers in Figure 6-11A and B show many humps one after another on both top and bottom surfaces. We believe this is caused by high surface charge of GO sheets (-42.27 ± 1.33 mV) that make GO sheets repel each other rather than adhere together during the increasing in sheet-to-sheet interactions and result in rumpled surfaces. Tensile strengths of graphene papers and GO papers tested are about 140 MPa and 110 MPa, respectively, as shown in Figure 6-12, and are close to the strength reported.

Graphene Actuators

Graphene actuators were made in a relatively simple way by laminating two strips of graphene papers with an intermediate layer of larger strip of double-sided tape, resulting in a sandwich structure. Schematic illustrations of an actuator and apparatus used are shown in Figure 6-13. Detailed information is in materials and methods session. In order to estimate capacitance of graphene papers, cyclic voltammetry measurements under different scan rates were carried out on a single strip of graphene

paper immersed in 1 M NaCl solution. Dimensions of the strip were 2 mm in width and 15 mm in length. The length of the strip immersed was 10 mm. One side of the strip was covered with an insulating tape, resulting in a superficial active area of 0.2 cm^2 . Since 2.5 cm^2 of graphene paper can be made by filtration of 6 ml of graphene dispersion containing 1.5 mg of graphene, the weight of graphene immersed in solution therefore becomes 0.12 mg. After several cycles to reach maximum degree of wetting, cyclic voltammograms of the graphene strip under various scan rates are shown in Figure 6-14A where a saturated calomel electrode is used as the reference electrode and a platinum wire is used as the counter electrode. The capacitance of graphene papers can therefore be estimated by calculating the ratio of steady state current to scan rate or by plotting steady state currents versus scan rates as shown in Figure 6-14B that gives a capacitance of 0.006 F or 50F/g, which is three-time higher than a nanotube paper, demonstrating high surface area of graphene sheets (132).

Actuations of a graphene actuator operated by potential step method between -2 and 2 volts in 1 M NaCl solution are shown in Figure 6-15. Voltages reported here are with respect to the graphene strip on the right hand side. Few cycles of operations were also performed before hand to ensure maximum wetting of the actuator. Positions and displacements of the actuator tip were then recorded and calculated via the graph paper with the initial position of the actuator tip as the origin. Figure 6-15A shows cross-sectional images of a graphene actuator under eight successive potential steps with a total of four cycles ($-2/2 \text{ V}$ repeatedly) in which the actuator moves to the right when a positive voltage is applied and to the left when a negative voltage is applied. The moving direction of the graphene actuator is actually opposite to that of the carbon

nanotube actuators proposed by Baughman and colleagues with respect to the direction of an applied voltage. The actuation mechanism of carbon nanotube actuators is based on quantum chemical-based expansion that causes dimensional changes in covalently bonded directions and injection of electrons results in bond expansion (132). As a result, carbon nanotube actuators bend to the anode. Meanwhile, anions and cations in electrolyte are moved into the anode and cathode, respectively, to compensate the injected charges. These dopant intercalations can actually result in swelling electrodes and extent of swelling depends on the size of dopants (130, 139, 140). Since chloride ions are larger than sodium ions, actuation due to dopant intercalations more likely bend to the cathode and is opposite to that due to quantum chemical-based expansion. For our graphene actuators, we found that dopant intercalations are required and important. From Figure 6-15A, since the graphene actuator bend to the cathode, we conclude that actuation due to dopant intercalation suppresses that due to quantum chemical-based expansion, resulting in a movement opposite to carbon nanotube actuators.

Displacements of the actuator tip in Figure 6-15A under repeated potential steps between -2 and 2 volts in 1 M NaCl solution are calculated and shown in Figure 6-15B. From this simple measurement, the displacement is found to be around 1.2 mm with 10 mm of graphene actuators immersed in 1 M NaCl electrolyte.

Actuations of a graphene actuator operated by cyclic voltammetry method between -2 and 2 volts in 1 M NaCl solution with a scan rate of 50 mV/s are shown in Figure 6-16. The left side of the graphene actuator was set as the working electrode while the right side was set at both counter and reference electrodes. No pre-cycling was conducted before recording. The very beginning cycles of the cyclic

voltammograms of the graphene actuator are shown in Figure 6-16A. The increasing in the current at this stage demonstrates that wetting of the actuator occurs at beginning along with dopant intercalations. After few cycles of operations, the current becomes steady, corresponding to the finish of the wetting process. The displacement measured is shown in Figure 6-16B. At the beginning, almost no displacement is observed. The extent of displacement increases along with the increasing in cyclic numbers and then reaches a steady value of around 1.2 mm, which is almost the same as actuators operated by potential steps. Figure 15B also demonstrates that the graphene actuator can be cycled up to 140 cycles.

Summary

We demonstrate that electromechanical graphene actuators can be made by laminating two strips of graphene papers with an intermediate dielectric layer. Graphene papers were produced by flow-directed assembly of graphene sheets, which were obtained from chemically reduced GO sheets. GO sheets were generated by exfoliation of highly oxygenated graphite in water. Capacitance of graphene papers was estimated to be 0.006F or 50F/g by cyclic voltammetry and is almost three-time higher than carbon nanotube papers. We also found that the actuation mechanism of graphene actuators is most likely due to swelling of electrodes originating from dopant intercalations. The displacements of actuators under repeated potential steps between -2 and 2 volts in 1 M NaCl solution was determined to be around 1.2 mm with 10 mm of graphene actuators immersed in electrolyte. Actuations of a graphene actuator operated by cyclic voltammetry method between -2 and 2 volts in 1 M NaCl solution with a scan rate of 50 mV/s were also carried out. Wetting of the graphene actuator was found during the first

few cycles. The extent of displacement increases along with the increasing in cyclic numbers and then reaches a steady value of around 1.2 mm, which is almost the same as actuators operated by potential steps. Actuation of graphene actuators was able to last up to 140 cycles without significant degradation.

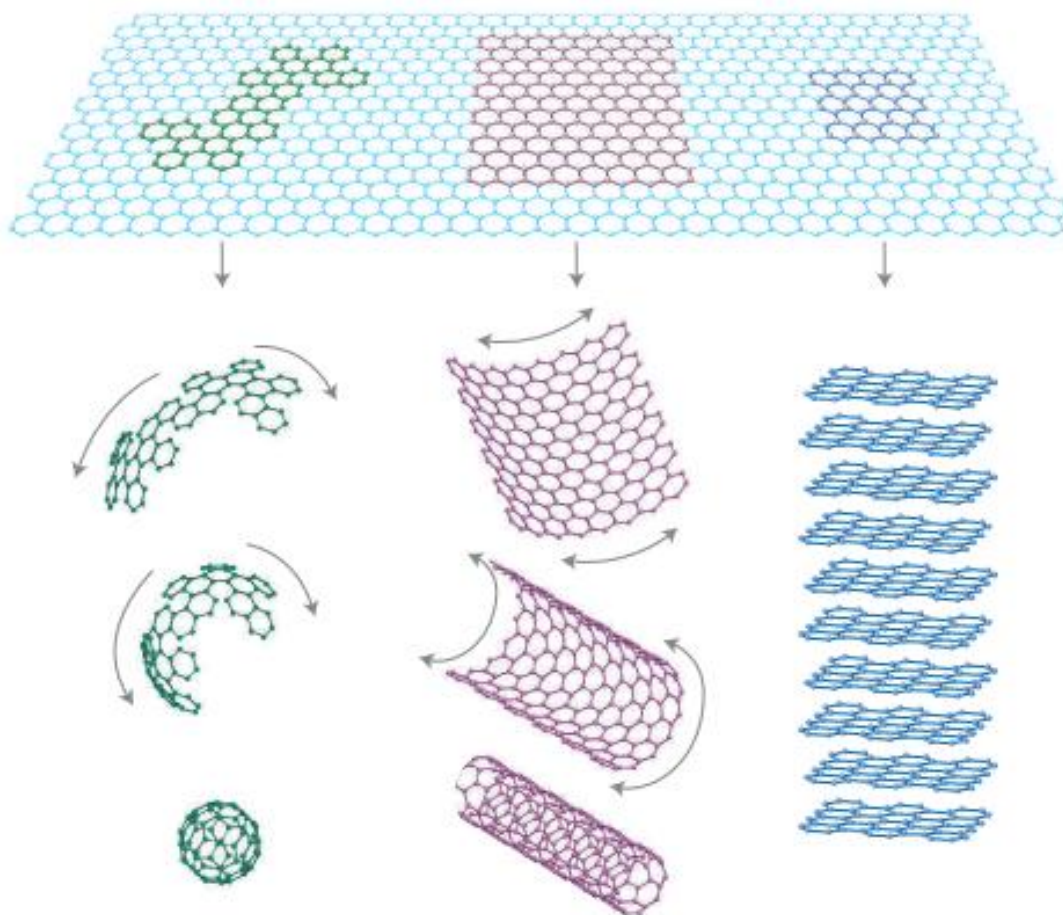


Figure 6-1. Mother of all graphitic forms (121).

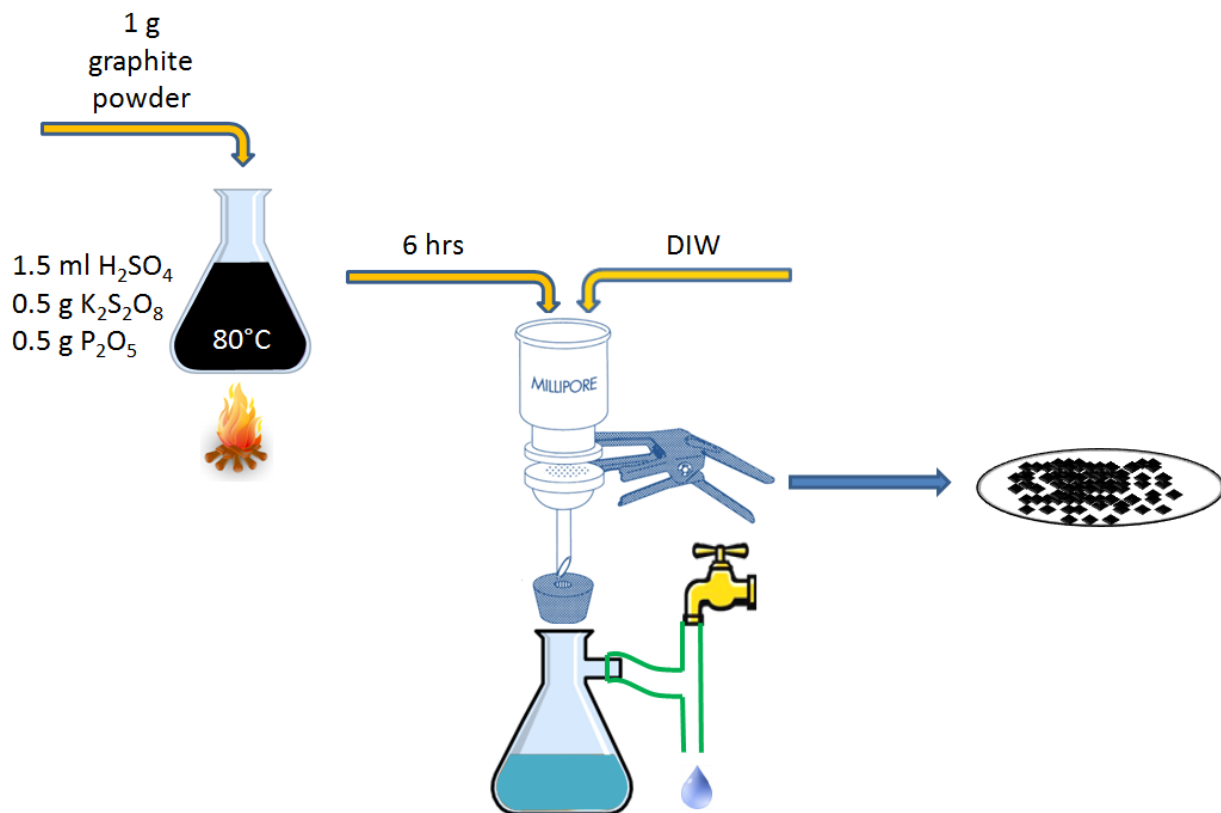


Figure 6-2. Schematic illustration of an additional oxidation prior to Hummer's method.

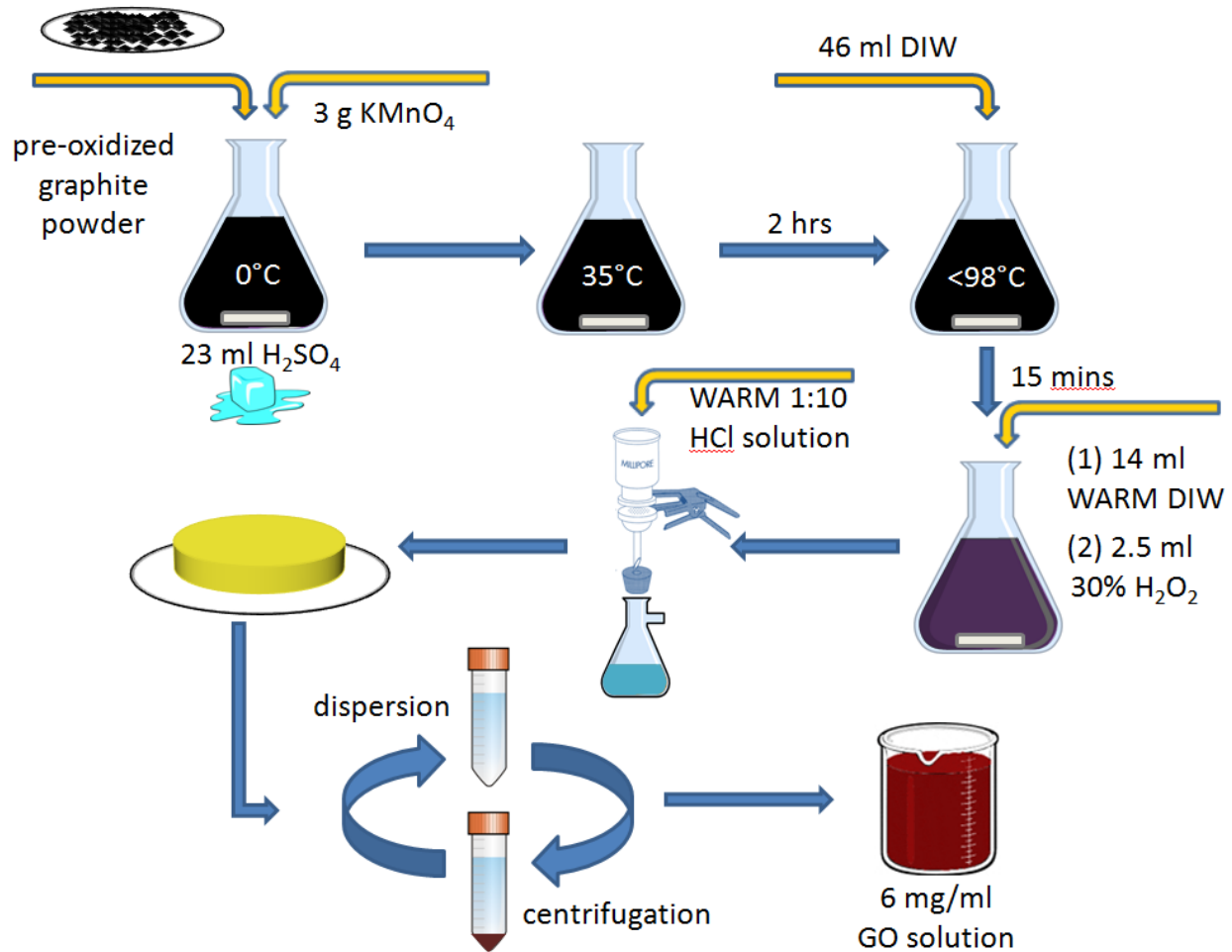


Figure 6-3. Schematic illustration of Hummers' method for GO preparation.

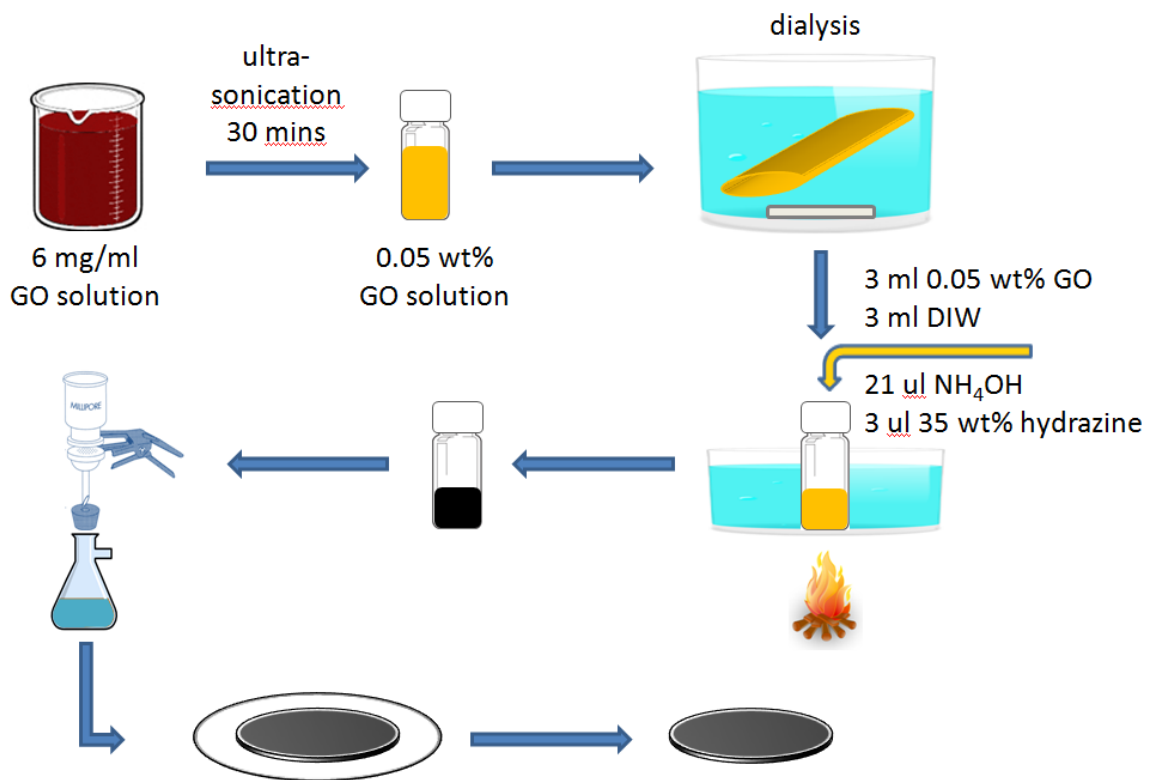




Figure 6-5. Images of colloidal dispersions of (A) GO and (B) graphene.

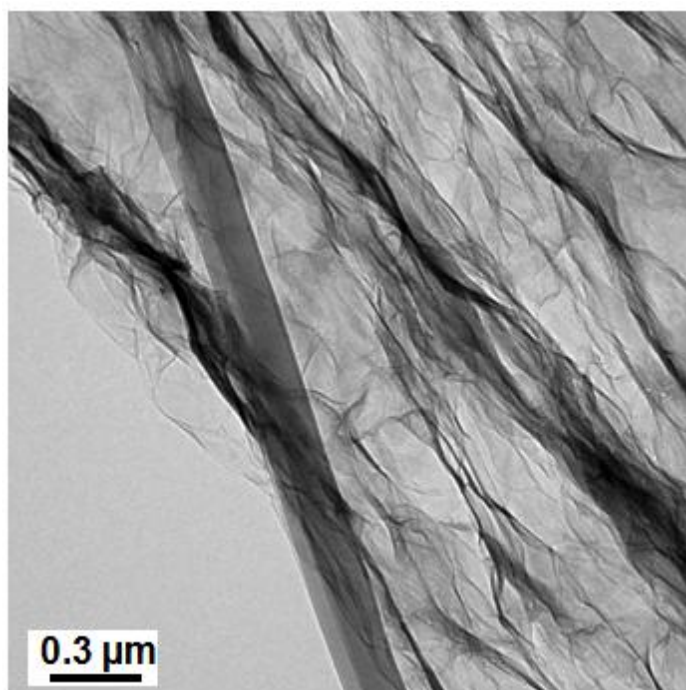


Figure 6-6. TEM image of graphene sheets.

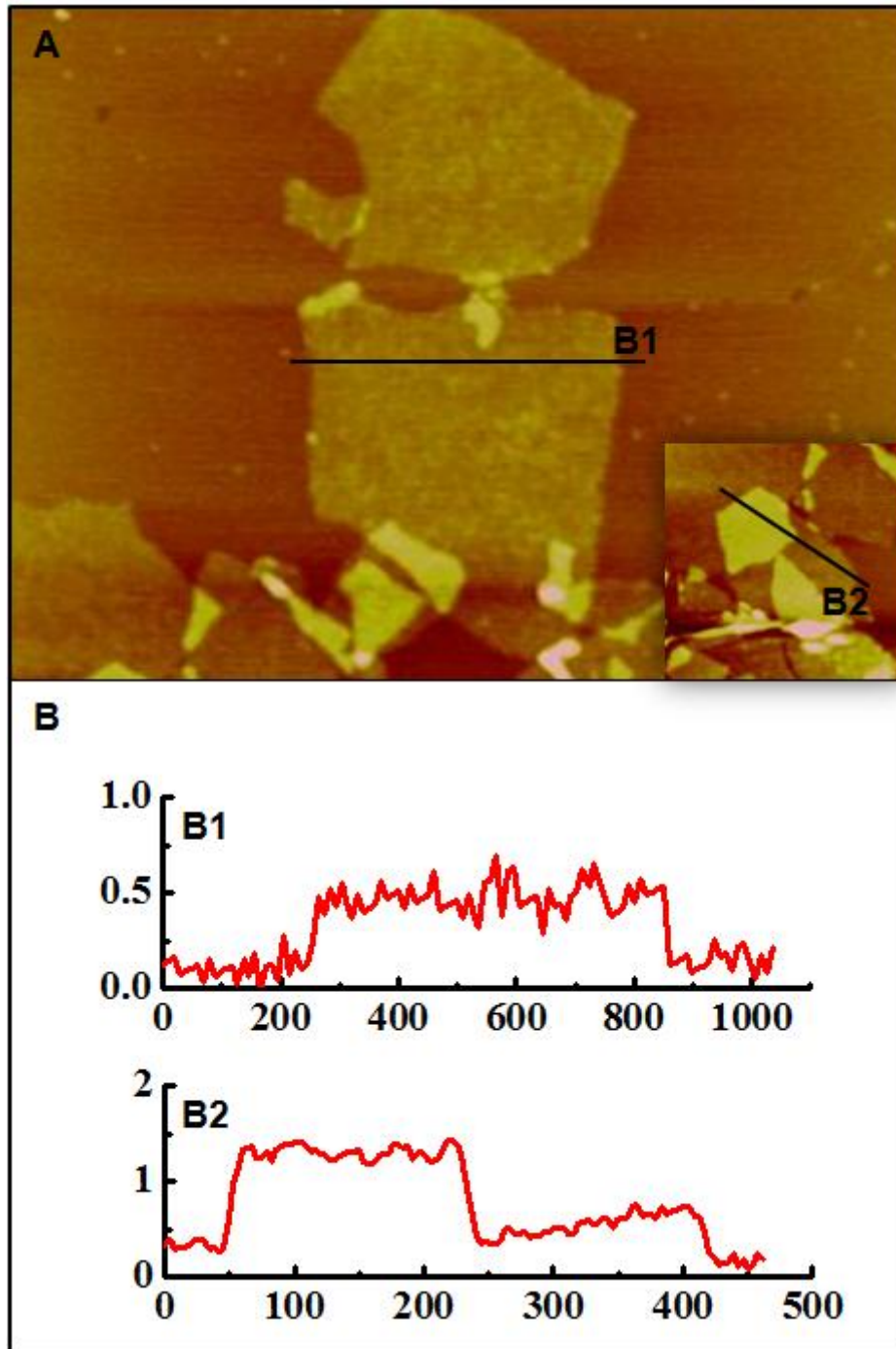


Figure 6-7. (A) Tapping-mode AFM image of graphene sheets with (B) height profiles B1 and B2 taken along the lines in (A). The sample was prepared by drop-casting diluted graphene dispersion onto a mica substrate.

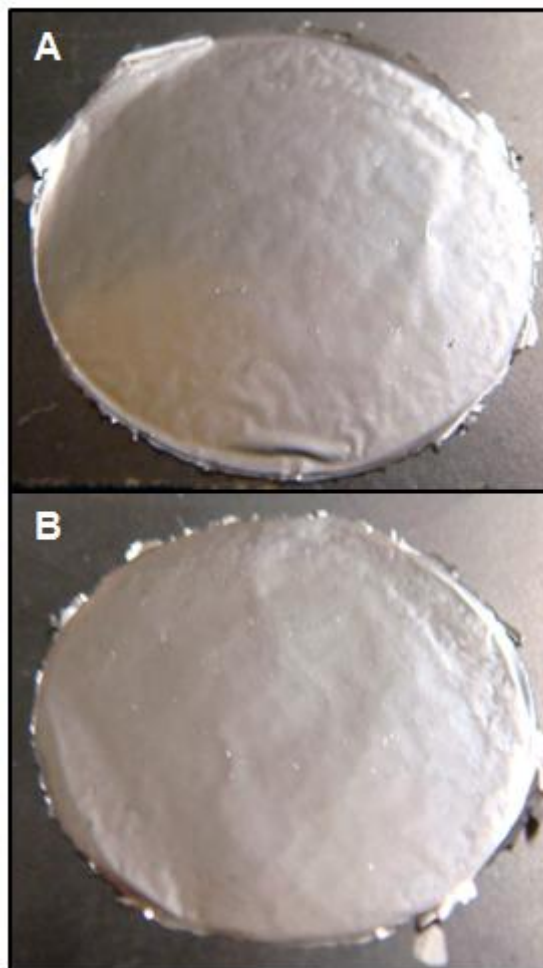


Figure 6-8. (A) Top and (B) bottom side images of a free-standing graphene paper made by vacuum filtration of graphene dispersion through an Anodisc membrane.

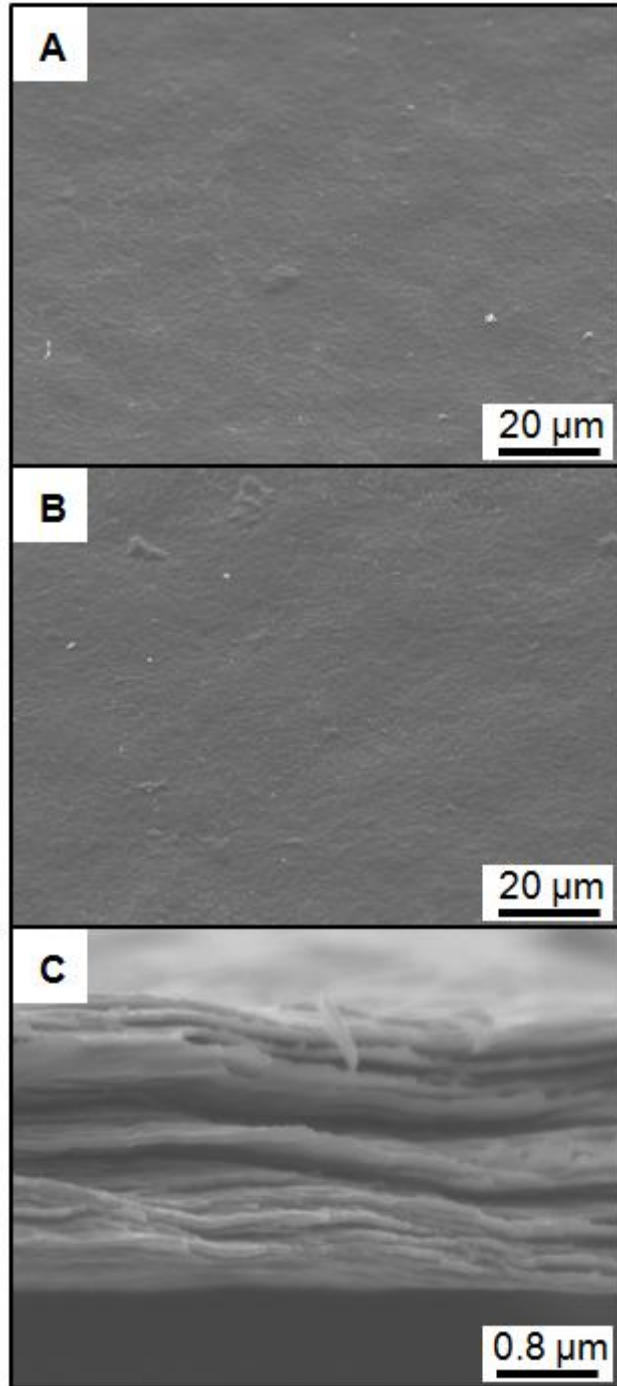


Figure 6-9. SEM images of a graphene paper. (A) Top-view SEM image, (B) bottom-view SEM image and (C) cross-sectional SEM image.

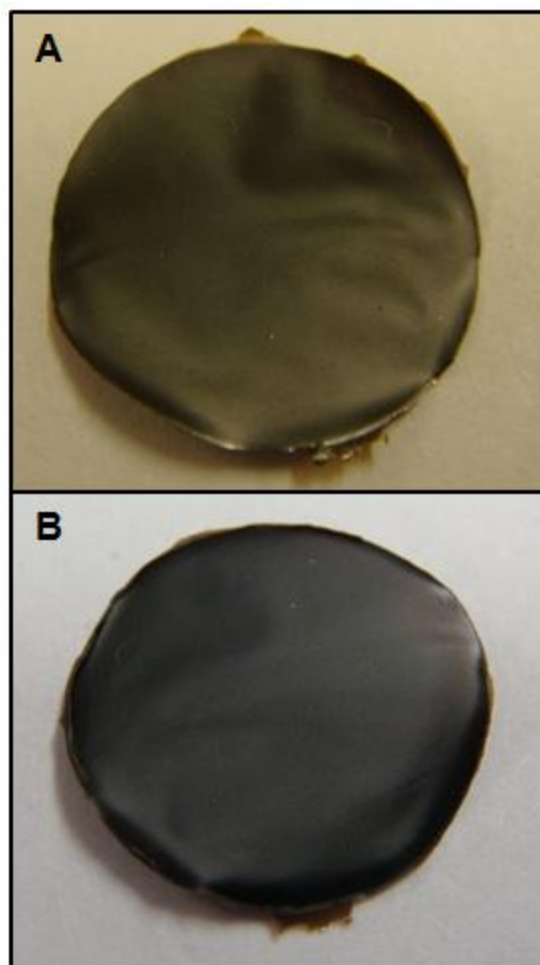


Figure 6-10. (A) Top and (B) bottom side images of a free-standing graphene paper made by vacuum filtration of GO dispersion through an Anodisc membrane.

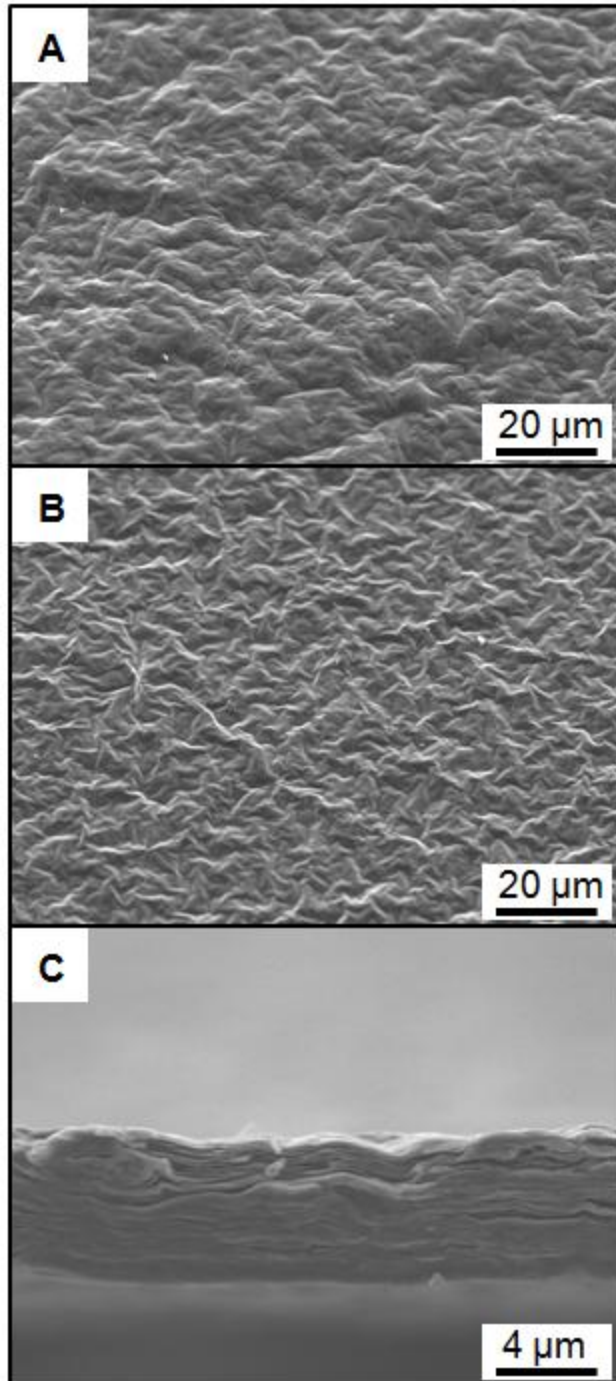


Figure 6-11. SEM images of a GO paper. (A) Top-view SEM image, (B) bottom-view SEM image and (C) cross-sectional SEM image.

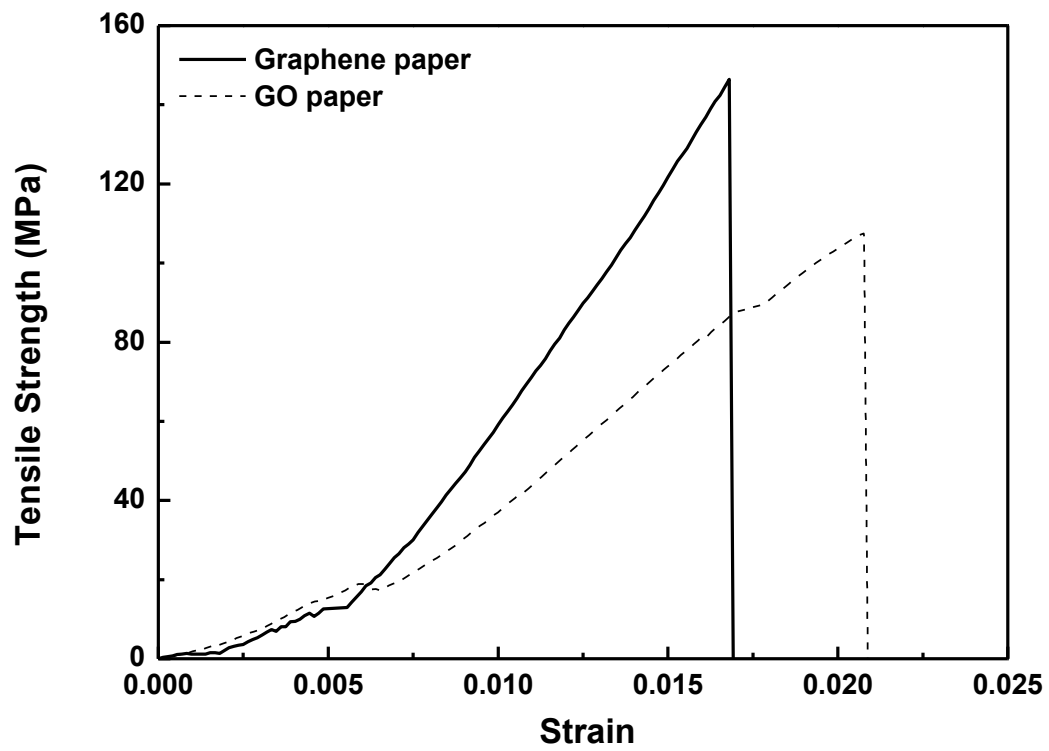


Figure 6-12. Tensile stress versus strain curve for a free-standing graphene and GO paper.

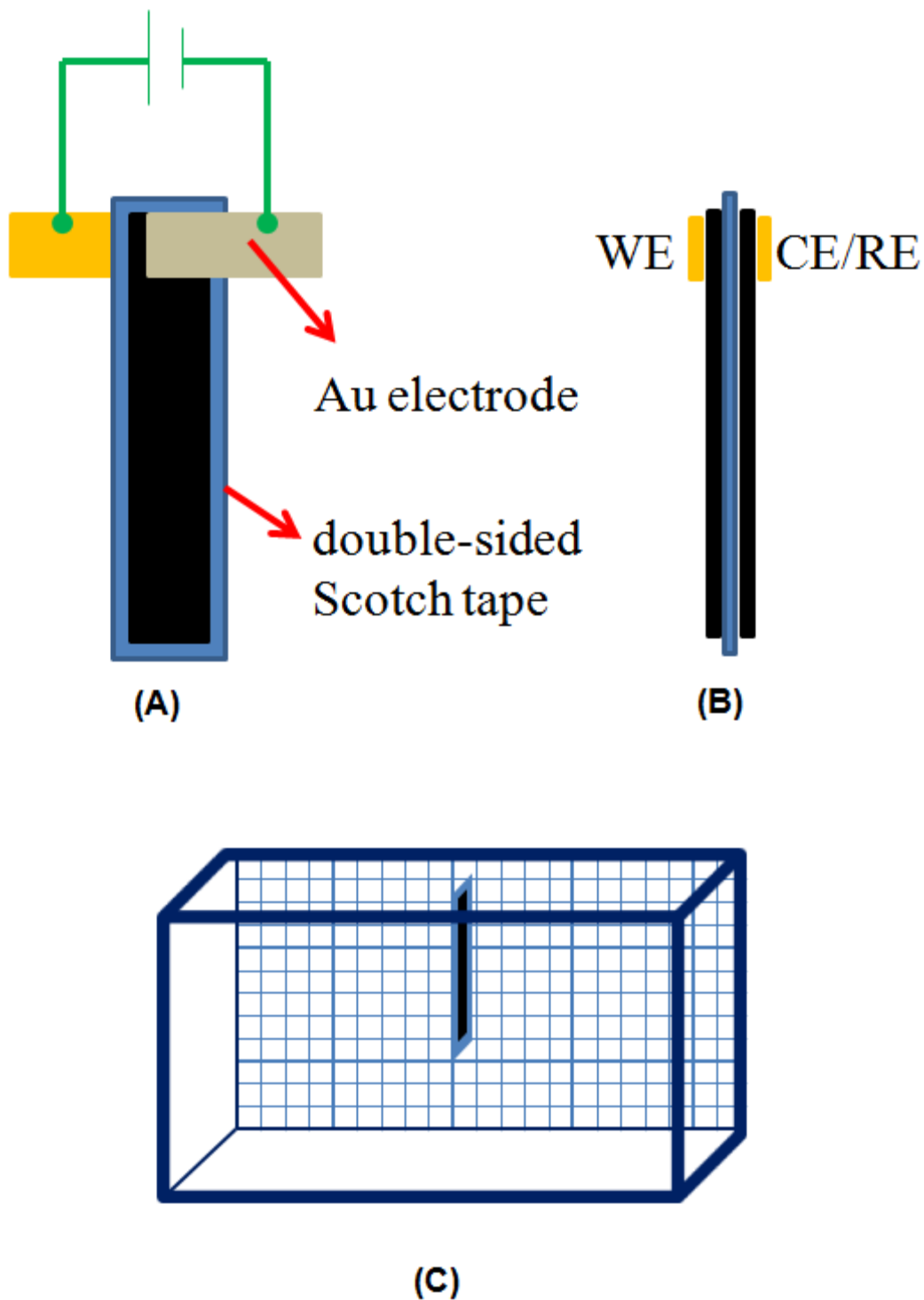
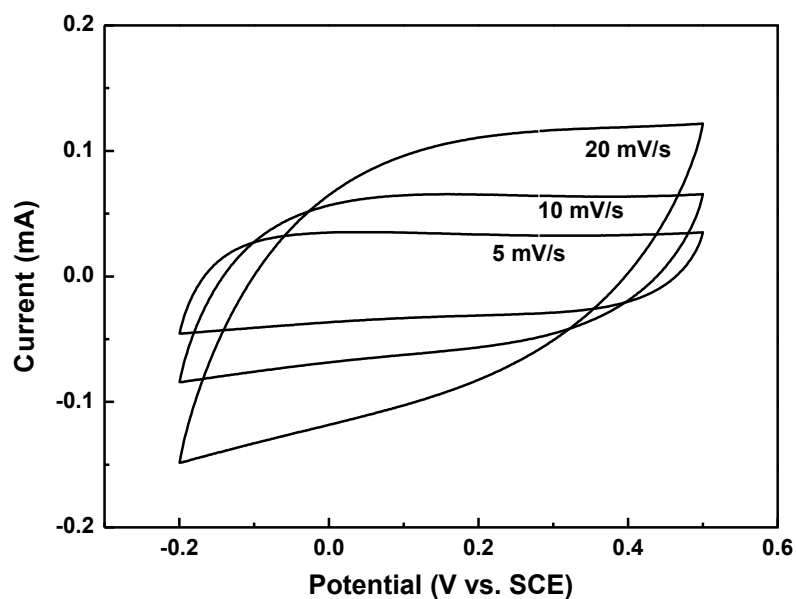
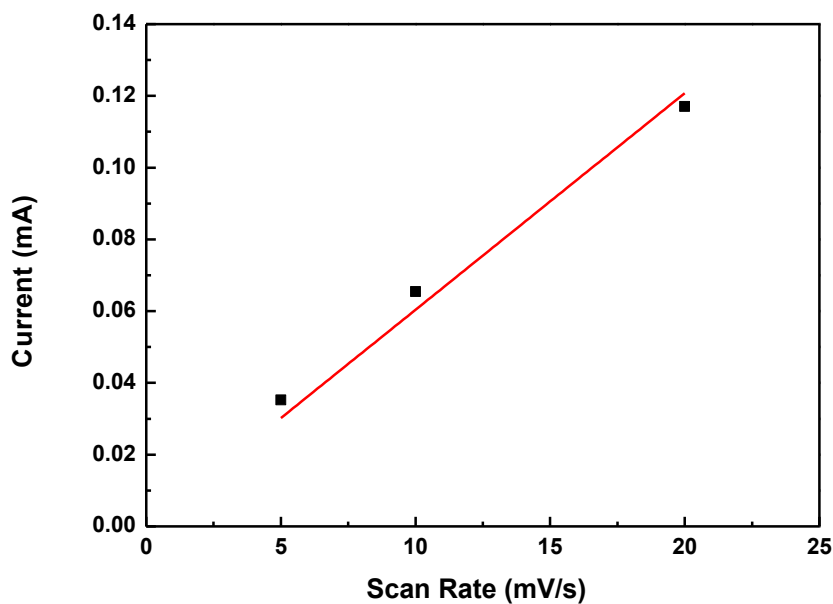


Figure 6-13. Schematic illustrations of a graphene actuator. (A) Front-view of the actuator, (B) side-view of the actuator and (C) apparatus used for displacement measurement.

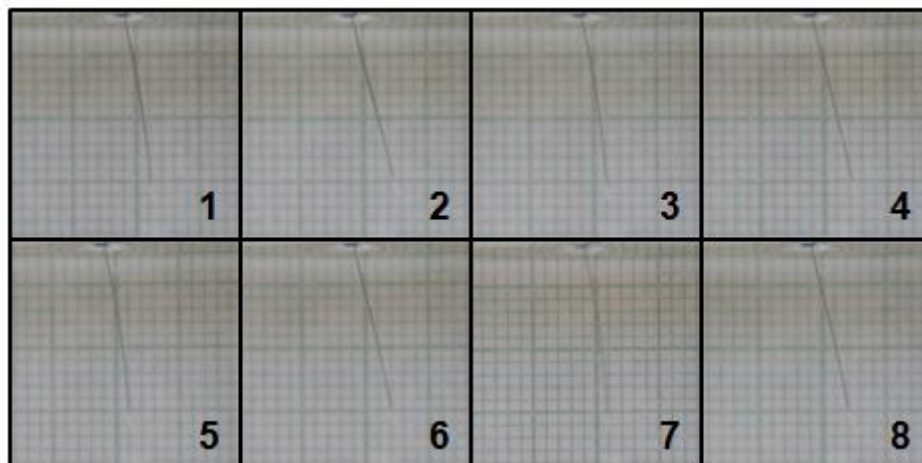


(A)

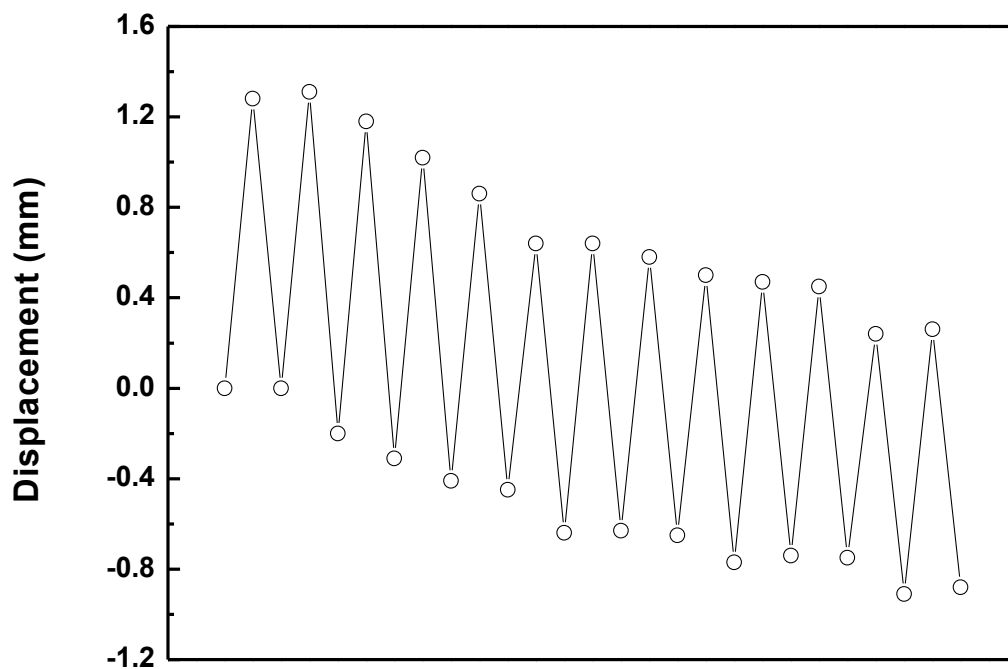


(B)

Figure 6-14. (A) Cyclic voltammograms of a graphene strip at various scan rates in 1 M NaCl solution. A saturated calomel electrode was used as the reference electrode and a platinum wire was used as the counter electrode. The superficial active area was 0.2 cm^2 and the weight of graphene paper immersed was 0.12 mg. (B) A plot of steady state currents in (A) versus corresponding scan rates. The slope in (B) is 0.006 F.

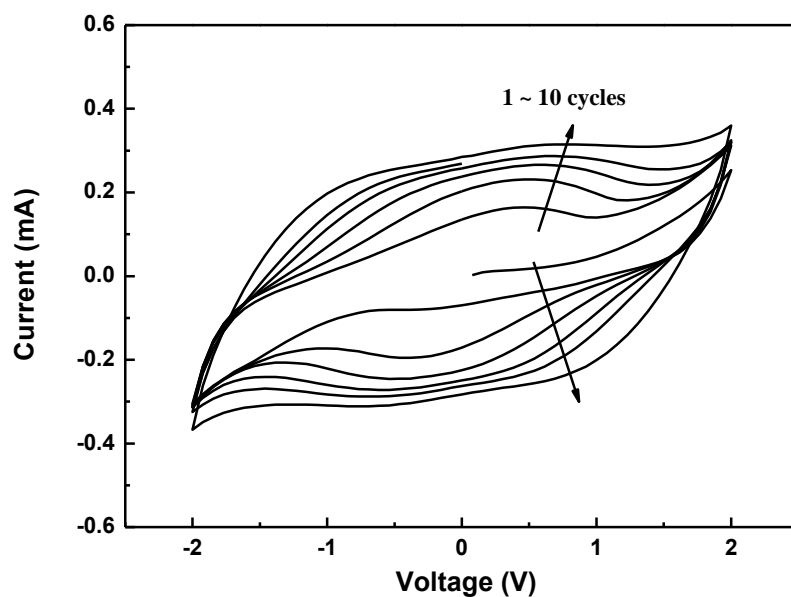


(A)

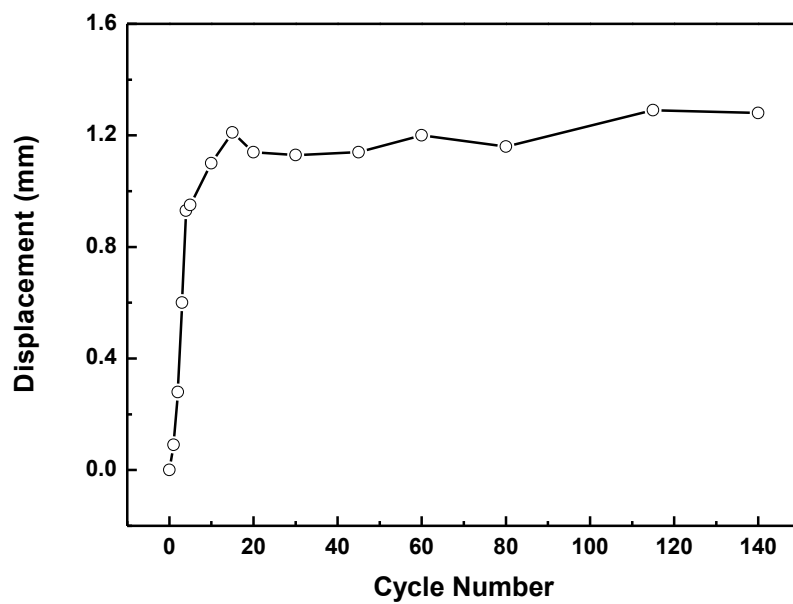


(B)

Figure 6-15. (A) Cross-sectional images of a graphene actuator under eight successive potential steps with a total of four cycles ($-2/2$ V repeatedly). (B) Displacements of the actuator tip in (A) under repeated potential steps.



(A)



(B)

Figure 6-16. (A) Two-electrode cyclic voltammograms of a graphene actuator operated between -2 and 2 volts in 1 M NaCl solution with a scan rate of 50 mV/s. (B) Corresponding displacements of the actuator in (A) as a function of cycle number.

CHAPTER 7 CONCLUSIONS

A simple electrodeposition technology that enables rapid production of large-area polymer nanocomposites with layered structures that mimic the nacreous layer of mollusk shells was studied. Uniform, electrostatically stabilized gibbsite nanoplatelets with high aspect ratio were preferentially oriented parallel to the electrode surface when an external direct current electric field was applied. The electroplated ceramic films had uniform thickness, and the thickness could be controlled by adjusting the nanoplatelet concentration of the electroplating baths. Homogeneous, optically transparent nanocomposites were obtained when the interstitials between the aligned nanosheets were infiltrated with polymer. The resulting ceramic-polymer nanocomposites exhibited four-time higher tensile strength and nearly 1 order of magnitude higher modulus than pure polymer films. The covalent linkage between the nanoplatelets and the polymer matrix plays an important role in determining the mechanical properties of these biomimetic nanocomposites.

Electrophoretic co-deposition of polymer-gibbsite nanocomposites was also demonstrated. The electrodeposited PVA-Gibbsite nanocomposite films were optically transparent and flexible, even though the weight fraction of the brittle inorganic phase was higher than 80%. The electrophoretic co-deposition assembly of positively charged gibbsite nanoplatelets and cationic PEI polyelectrolytes into ordered multilayer in a single step was performed. The resulting nanocomposite had similar organic/inorganic weight ratio and ordered brick-and-mortar nanostructure as natural nacles. Nanoindentation tests showed that this nanocomposites exhibited similar hardness and reduced modulus as those of pure gibbsite coatings.

Assembling of surface-roughened inorganic nanoplatelets into ordered multilayer that mimic the asperities interposing nanostructure found in the nacreous layer of mollusk shells was investigated. A thin layer of sol-gel silica was coated on smooth gibbsite nanoplatelets in order to increase the surface roughness to mimic the asperity of aragonite platelets found in nacs. To avoid the severe cracking caused by the shrinkage of sol-gel silica during drying, polyelectrolyte PEI was used to reverse the surface charge of silica-coated-gibbsite nanoplatelets and increased the adherence and strength of the electrodeposited films. Polymer nanocomposites could then be made by infiltrating the interstitials of the aligned nanoplatelet multilayer with photocurable monomer followed by photopolymerization. The resulting self-standing films were highly transparent and exhibited nearly three-time higher tensile strength and one-order-of-magnitude higher toughness than those of pure polymer. The measured tensile strength agrees with that predicted by a simple shear lag model.

A simple and scalable colloidal templating nanofabrication technology for generating periodic metallic nanopyramid arrays as electrodes for electrochemical surface-enhanced Raman spectroscopy (SERS) was conducted. These periodic arrays of nanopyramids with nanoscale sharp tips and high tip density could enhance the local electromagnetic field in the vicinity of the nanotips, resulting in high SERS enhancement (on the order of 10^6). The effects of the applied electrode potential and the electrode redox reactions on the SERS enhancement were investigated. Finite element electromagnetic modeling was also developed to simulate the electric field amplitude distribution and the corresponding Raman enhancement factors surrounding arrays of nanopyramids.

Actuators that can convert electrical energy into mechanical energy are of great importance for applications in many fields. Development of novel actuators requires materials that have excellent electrical, thermal, and mechanical properties. Graphene has been studied over years and is known to have extraordinary qualities. We studied electromechanical actuators based on two strips of graphene papers with an intermediate dielectric layer. The actuation mechanism of graphene actuators was most likely due to swelling of electrodes originating from dopant intercalations. The swelling-induced bending actually suppressed that due to quantum chemical-based expansion, resulting in a bending direction opposite to that of carbon nanotube actuators. Capacitance of graphene papers was estimated to be 0.006F or 50F/g by cyclic voltammetry and was almost three times higher than carbon nanotube papers. The displacements of actuators under repeated potential steps between -2 and 2 volts in 1 M NaCl solution was determined to be around 1.2 mm with 10 mm of graphene actuators immersed in electrolyte. Actuations of a graphene actuator operated by cyclic voltammetry at a scan rate of 50 mV/s were able to last up to 140 cycles without significant degradation.

LIST OF REFERENCES

1. S. C. Glotzer, M. J. Solomon, *Nature Materials* **6**, 557 (2007).
2. I. D. Hosein, C. M. Liddell, *Langmuir* **23**, 10479 (2007).
3. S. H. Lee *et al.*, *Journal of Materials Chemistry* **18**, 4912 (2008).
4. A. B. Pawar, I. Kretzschmar, *Langmuir* **24**, 355 (2008).
5. K. J. Stebe, E. Lewandowski, M. Ghosh, *Science* **325**, 159 (2009).
6. J. M. McLellan, Z. Y. Li, A. R. Siekkinen, Y. N. Xia, *Nano Letters* **7**, 1013 (2007).
7. Z. Y. Tang, N. A. Kotov, S. Magonov, B. Ozturk, *Nature Materials* **2**, 413 (2003).
8. P. Podsiadlo *et al.*, *Science* **318**, 80 (2007).
9. L. J. Bonderer, A. R. Studart, L. J. Gauckler, *Science* **319**, 1069 (2008).
10. F. M. van der Kooij, K. Kassapidou, H. N. W. Lekkerkerker, *Nature* **406**, 868 (2000).
11. D. van der Beek, H. N. W. Lekkerkerker, *Langmuir* **20**, 8582 (2004).
12. M. C. D. Mourad, J. Wijnhoven, D. D. Van 'T Zand, D. Van der Beek, H. N. W. Lekkerkerker, *Phil. Trans. R. Soc. A* **364**, 2807 (2006).
13. D. van der Beek, P. B. Radstake, A. V. Petukhov, H. N. W. Lekkerkerker, *Langmuir* **23**, 11343 (2007).
14. A. Donev *et al.*, *Science* **303**, 990 (2004).
15. J. A. Lee, L. L. Meng, D. J. Norris, L. E. Scriven, M. Tsapatsis, *Langmuir* **22**, 5217 (2006).
16. A. F. Mejia, P. He, D. W. Luo, M. Marquez, Z. D. Cheng, *Journal of Colloid and Interface Science* **334**, 22 (2009).
17. S. Kamat, X. Su, R. Ballarini, A. H. Heuer, *Nature* **405**, 1036 (2000).
18. H. J. Gao, B. H. Ji, I. L. Jager, E. Arzt, P. Fratzl, *Proceedings of the National Academy of Sciences* **100**, 5597 (2003).
19. F. Barthelat, *Phil. Trans. R. Soc. A* **365**, 2907 (2007).
20. A. P. Jackson, J. F. V. Vincent, R. M. Turner, *Proc. R. Soc. Lond. B* **234**, 415 (1988).

21. I. A. Aksay *et al.*, *Science* **273**, 892 (1996).
22. B. L. Smith *et al.*, *Nature* **399**, 761 (1999).
23. G. Mayer, *Science* **310**, 1144 (2005).
24. J. S. Lee, Y. J. Lee, E. L. Tae, Y. S. Park, K. B. Yoon, *Science* **301**, 818 (2003).
25. J. C. Love, A. R. Urbach, M. G. Prentiss, G. M. Whitesides, *Journal of the American Chemical Society* **125**, 12696 (2003).
26. C. E. Snyder, A. M. Yake, J. D. Feick, D. Velegol, *Langmuir* **21**, 4813 (2005).
27. J. W. Kim, R. J. Larsen, D. A. Weitz, *Journal of the American Chemical Society* **128**, 14374 (2006).
28. T. Ebina, F. Mizukami, *Advanced Materials* **19**, 2450 (2007).
29. N. Almqvist *et al.*, *Materials Science and Engineering: C* **7**, 37 (1999).
30. S. Deville, E. Saiz, R. K. Nalla, A. P. Tomsia, *Science* **311**, 515 (2006).
31. R. F. Chen, C. A. Wang, Y. Huang, H. R. Le, *Materials Science and Engineering: C* **28**, 218 (2008).
32. I. Zhitomirsky, *Advances in Colloid and Interface Science* **97**, 279 (2002).
33. O. D. Velev, K. H. Bhatt, *Soft Matter* **2**, 738 (2006).
34. M. Holgado *et al.*, *Langmuir* **15**, 4701 (1999).
35. P. V. Braun, P. Wiltzius, *Nature* **402**, 603 (1999).
36. T. Liu, B. Q. Chen, J. R. G. Evans, *Bioinspiration & Biomimetics* **3**, 016005 (2008).
37. A. M. Wierenga, T. A. J. Lenstra, A. P. Philipse, *Colloids and Surfaces A: Physicochemical and Engineering Aspects* **134**, 359 (1998).
38. H. Kim *et al.*, *Applied Physics Letters* **91**, 133106 (2007).
39. L. Y. Sun, W. J. Boo, H. J. Sue, A. Clearfield, *New Journal of Chemistry* **31**, 39 (2007).
40. H. Deng, S. H. Yang, S. Xiao, H. M. Gong, Q. Q. Wang, *Journal of the American Chemical Society* **130**, 2032 (2008).

41. J. Wijnhoven, *Chemistry of Materials* **16**, 3821 (2004).
42. J. Wijnhoven, *Journal of Colloid and Interface Science* **292**, 403 (2005).
43. F. M. van der Kooij, H. N. W. Lekkerkerker, *The Journal of Physical Chemistry B* **102**, 7829 (1998).
44. A. B. D. Brown, S. M. Clarke, A. R. Rennie, *Langmuir* **14**, 3129 (1998).
45. A. P. Philipse, C. Smits, A. Vrij, *Journal of Colloid and Interface Science* **129**, 335 (1989).
46. B. D. Cullity, *Elements of x-ray diffraction*. (Addison-Wesley Publishing Company, Reading, MA, ed. 2nd, 1978).
47. W. B. Russel, D. A. Saville, W. R. Schowalter, *Colloidal dispersions*. (Cambridge University Press, Cambridge, 1989).
48. A. Dietrich, A. Neubrand, *Journal of the American Ceramic Society* **84**, 806 (Apr, 2001).
49. W. C. Oliver, G. M. Pharr, *Journal of Materials Research* **7**, 1564 (1992).
50. V. Vertlib *et al.*, *Journal of Materials Research* **23**, 1026 (Apr, 2008).
51. T. F. Page, W. C. Oliver, C. J. McHargue, *Journal of Materials Research* **7**, 450 (1992).
52. G. M. Pharr, *Materials Science and Engineering a-Structural Materials Properties Microstructure and Processing* **253**, 151 (1998).
53. K. S. Katti, B. Mohanty, D. R. Katti, *Journal of Materials Research* **21**, 1237 (2006).
54. Y. Oaki, H. Imai, *Angewandte Chemie International Edition* **44**, 6571 (2005).
55. A. G. Evans *et al.*, *Journal of Materials Research* **16**, 2475 (2001).
56. R. Z. Wang, Z. Suo, A. G. Evans, N. Yao, I. A. Aksay, *Journal of Materials Research* **16**, 2485 (2001).
57. P. Jiang, J. F. Bertone, K. S. Hwang, V. L. Colvin, *Chemistry of Materials* **11**, 2132 (1999).
58. A. A. Chabanov, Y. Jun, D. J. Norris, *Applied Physics Letters* **84**, 3573 (2004).

59. C. Graf, D. L. J. Vossen, A. Imhof, A. van Blaaderen, *Langmuir* **19**, 6693 (Aug, 2003).
60. R. K. Iler, *The Chemistry of Silica*. (John Wiley & Sons, New York, 1979).
61. W. L. Barnes, A. Dereux, T. W. Ebbesen, *Nature* **424**, 824 (2003).
62. G. Chumanov, K. Sokolov, B. W. Gregory, T. M. Cotton, *Journal of Physical Chemistry* **99**, 9466 (1995).
63. P. Mulvaney, *Langmuir* **12**, 788 (1996).
64. I. Lisiecki, F. Billoudet, M. P. Pileni, *Journal of Physical Chemistry* **100**, 4160 (1996).
65. A. P. Hibbins, J. R. Sambles, C. R. Lawrence, *Journal of Modern Optics* **45**, 2051 (1998).
66. M. N. Zervas, *Ieee Photonics Technology Letters* **2**, 597 (1990).
67. F. Caruso, T. Serizawa, D. N. Furlong, Y. Okahata, *Langmuir* **11**, 1546 (1995).
68. T. W. Ebbesen, H. J. Lezec, H. F. Ghaemi, T. Thio, P. A. Wolff, *Nature* **391**, 667 (1998).
69. L. Martin-Moreno *et al.*, *Physical Review Letters* **86**, 1114 (2001).
70. L. Salomon, F. Grillot, A. V. Zayats, F. de Fornel, *Physical Review Letters* **86**, 1110 (2001).
71. R. Gordon *et al.*, *Physical Review Letters* **92**, 037401 (2004).
72. H. A. Bethe, *Physical Review* **66**, 163 (1944).
73. D. S. Kim *et al.*, *Physical Review Letters* **91**, (2003).
74. A. G. Brolo, E. Arctander, R. Gordon, B. Leathem, K. L. Kavanagh, *Nano Letters* **4**, 2015 (2004).
75. A. G. Brolo, R. Gordon, B. Leathem, K. L. Kavanagh, *Langmuir* **20**, 4813 (2004).
76. K. J. K. Koerkamp, S. Enoch, F. B. Segerink, N. F. van Hulst, L. Kuipers, *Physical Review Letters* **92**, 183901 (2004).
77. J. J. Baumberg *et al.*, *Nano Letters* **5**, 2262 (2005).

78. S. M. Nie, S. R. Emery, *Science* **275**, 1102 (1997).
79. G. A. Baker, D. S. Moore, *Analytical and Bioanalytical Chemistry* **382**, 1751 (2005).
80. J. A. Dieringer *et al.*, *Faraday Discussion* **132**, 9 (2006).
81. K. Kneipp, H. Kneipp, J. Kneipp, *Accounts of Chemical Research* **39**, 443 (2006).
82. M. Fleischm, P. J. Hendra, A. McQuilla, *Chemical Physics Letters* **26**, 163 (1974).
83. S. Zou, M. J. Weaver, X. Q. Li, B. Ren, Z. Q. Tian, *Journal of Physical Chemistry B* **103**, 4218 (1999).
84. Z. Q. Tian, B. Ren, D. Y. Wu, *Journal of Physical Chemistry B* **106**, 9463 (2002).
85. Z. Q. Tian, B. Ren, *Annual Review of Physical Chemistry* **55**, 197 (2004).
86. D. L. Jeanmaire, R. P. van Duyne, *Journal of Electroanalytical Chemistry* **84**, 1 (1977).
87. H. Chang, K. C. Hwang, *Journal of the American Chemical Society* **106**, 6586 (1984).
88. L. Stolberg, J. Lipkowski, D. E. Irish, *Journal of Electroanalytical Chemistry* **300**, 563 (1991).
89. A. Kudelski, B. J., *Vibrational Spectroscopy* **10**, 335 (1996).
90. R. G. Freeman *et al.*, *Science* **267**, 1629 (1995).
91. P. M. Tessier *et al.*, *Journal of the American Chemical Society* **122**, 9554 (2000).
92. Y. Lu, G. L. Liu, J. Kim, Y. X. Mejia, L. P. Lee, *Nano Letters* **5**, 119 (2005).
93. H. Wang, C. S. Levin, N. J. Halas, *Journal of the American Chemical Society* **127**, 14992 (2005).
94. S. Cintra *et al.*, *Faraday Discussion* **132**, 191 (2006).
95. M. E. Abdelsalam, S. Mahajan, P. N. Bartlett, J. J. Baumberg, A. E. Russell, *Journal of the American Chemical Society* **129**, 7399 (2007).
96. G. Braun *et al.*, *Journal of the American Chemical Society* **129**, 7760 (2007).

97. B. G. McMillan, L. E. A. Berlouis, F. R. Cruickshank, P. F. Brevet, *Electrochimica Acta* **53**, 1157 (2007).
98. L. A. Dick, A. D. McFarland, C. L. Haynes, R. P. Van Duyne, *The Journal of Physical Chemistry B* **106**, 853 (2002).
99. X. Y. Zhang, M. A. Young, O. Lyandres, R. P. Van Duyne, *Journal of the American Chemical Society* **127**, 4484 (2005).
100. X. Zhang, J. Zhao, A. V. Whitney, J. W. Elam, R. P. Van Duyne, *Journal of the American Chemical Society* **128**, 10304 (2006).
101. M. E. Abdelsalam *et al.*, *Electrochemistry Communications* **7**, 740 (2005).
102. B. Pettinger, B. Ren, G. Picardi, R. Schuster, G. Ertl, *Physical Review Letters* **92**, 096101 (2004).
103. H. Watanabe, Y. Ishida, N. Hayazawa, Y. Inouye, S. Kawata, *Physical Review B* **69**, 155418 (2004).
104. S. Chattopadhyay, L. C. Chen, K. H. Chen, *Critical Reviews in Solid State and Materials Sciences* **31**, 15 (2006).
105. C. H. Sun, N. C. Linn, P. Jiang, *Chemistry of Materials* **19**, 4551 (2007).
106. P. Jiang, M. J. McFarland, *Journal of the American Chemical Society* **126**, 13778 (2004).
107. F. A. Cotton, G. Wilkinson, *Advanced Inorganic Chemistry*. (John Wiley & Sons, New York, ed. 5, 1988).
108. A. G. Brolo, D. E. Irish, J. Lipkowski, *Journal of Physical Chemistry B* **101**, 3906 (1997).
109. W. H. Li, X. Y. Li, N. T. Yu, *Chemical Physics Letters* **305**, 303 (1999).
110. K. B. Wiberg, V. A. Walters, K. N. Wong, S. D. Colson, *Journal of Physical Chemistry* **88**, 6067 (1984).
111. M. Moskovits, D. P. Dilella, *Journal of Chemical Physics* **73**, 6068 (1980).
112. A. J. Bard, L. R. Faulkner, *Electrochemical Methods: Fundamentals and Applications*. (John Wiley & Sons, New York, ed. 2, 2001).
113. R. J. C. Brown, J. Wang, R. Tantra, R. E. Yardley, M. J. T. Milton, *Faraday Discussions* **132**, 201 (2006).

114. J. Jin, *The Finite Element Method in Electromagnetics*. (John Wiley and Sons, New York, ed. 2nd, 2002).
115. P. B. Johnson, R. W. Christy, *Physical Review B* **6**, (1972).
116. M. J. Madou, *Fundamentals of Microfabrication: The Science of Miniaturization*. (CRC Press, Boca Raton, FL, ed. 2nd, 2002).
117. J. Aizpurua *et al.*, *Physical Review Letters* **90**, (2003).
118. A. Hartschuh, E. J. Sanchez, X. S. Xie, L. Novotny, *Physical Review Letters* **90**, (2003).
119. Y. Fang, N. H. Seong, D. D. Dlott, *Science* **321**, 388 (2008).
120. K. S. Novoselov *et al.*, *Proceedings of the National Academy of Sciences of the United States of America* **102**, 10451 (2005).
121. A. K. Geim, K. S. Novoselov, *Nature Materials* **6**, 183 (2007).
122. X. Wang, L. J. Zhi, K. Mullen, *Nano Letters* **8**, 323 (2008).
123. G. Eda, M. Chhowalla, *Nano Letters* **9**, 814 (2009).
124. S. Stankovich *et al.*, *Nature* **442**, 282 (2006).
125. P. K. Hansma, P. J. Turner, R. S. Ruoff, *Nanotechnology* **18**, (2007).
126. D. Y. Cai, K. Yusoh, M. Song, *Nanotechnology* **20**, (2009).
127. P. K. Ang, W. Chen, A. T. S. Wee, K. P. Loh, *Journal of the American Chemical Society* **130**, 14392 (2008).
128. B. Huang *et al.*, *Journal of Physical Chemistry C* **112**, 13442 (2008).
129. D. W. Wang *et al.*, *Acs Nano* **3**, 1745 (2009).
130. R. H. Baughman, *Synthetic Metals* **78**, 339 (1996).
131. C. Lee, X. D. Wei, J. W. Kysar, J. Hone, *Science* **321**, 385 (2008).
132. R. H. Baughman *et al.*, *Science* **284**, 1340 (1999).
133. S. Park, J. An, J. W. Suk, R. S. Ruoff, *Small* **6**, 210 (2010).
134. D. A. Dikin *et al.*, *Nature* **448**, 457 (2007).

135. H. Chen, M. B. Muller, K. J. Gilmore, G. G. Wallace, D. Li, *Advanced Materials* **20**, 3557 (2008).
136. D. Li, M. B. Muller, S. Gilje, R. B. Kaner, G. G. Wallace, *Nature Nanotechnology* **3**, 101 (2008).
137. W. S. Hummers, R. E. Offeman, *Journal of the American Chemical Society* **80**, 1339 (1958).
138. N. I. Kovtyukhova *et al.*, *Chemistry of Materials* **11**, 771 (1999).
139. E. Smela, *Advanced Materials* **15**, 481 (Mar, 2003).
140. N. Terasawa, I. Takeuchi, H. Matsumoto, *Sensors and Actuators B-Chemical* **139**, 624 (2009).

BIOGRAPHICAL SKETCH

Tzung-Hua Lin received his Bachelor of Science in chemical engineering from the National Taiwan University in 2003. He continued his studies at the National Taiwan University and received a Master of Science in 2005. He joined the Department of Chemical Engineering at the University of Florida in August 2007.